

Background-Induced Forces from Quadratically Coupled Ultralight Dark Matter

Thomas Bouley^{1,*}, Xucheng Gan^{2,†}, Hailin Xu^{3,4,‡} and Tien-Tien Yu^{5,§}

¹*Humanities & Sciences Division, Cincinnati State Technical and Community College, Cincinnati OH 45223 USA*

²*Deutsches Elektronen-Synchrotron DESY, Notkestr. 85, 22607 Hamburg, Germany*

³*State Key Laboratory of Dark Matter Physics, Tsung-Dao Lee Institute & School of Physics and Astronomy, Shanghai Jiao Tong University, Shanghai 200240, China*

⁴*Key Laboratory for Particle Astrophysics and Cosmology (MOE)
& Shanghai Key Laboratory for Particle Physics and Cosmology,
Shanghai Jiao Tong University, Shanghai 200240, China*

⁵*Department of Physics and Institute for Fundamental Science, University of Oregon, Eugene OR 97403 USA*

Quadratically coupled ultralight scalar dark matter behaves as a coherent classical field whose interactions with matter can induce a composition-dependent force through the dark matter background. We present a complete calculation of this background-induced force beyond the spherically symmetric approximation. Using a partial-wave treatment of dark-matter scattering, we determine its angular dependence and derive an analytic description valid even when the dark-matter wavelength is much smaller than the Earth's radius. We show for the first time that Earth screening generates a characteristic frequency-band structure, splitting the signal into multiple sidebands that provide a distinctive experimental signature. We further show that the relative amplitudes of these sidebands vary annually due to the Earth's motion through the dark-matter halo, enabling the construction of a complete signal template. As an application of these results, we re-evaluate constraints from the MICROSCOPE mission, which currently provides the strongest laboratory limits on equivalence-principle violations from ultralight dark matter. We further show that proposed space-based equivalence-principle experiments, such as Galileo Galilei and STE-QUEST, can significantly enhance their sensitivity to ultralight scalar dark matter by incorporating the full frequency-band information.

arXiv:2606.28481v1 [hep-ph] 26 Jun 2026

* tbouley@uoregon.edu

† xucheng.gan@desy.de

‡ hailin.xu@sjtu.edu.cn

§ tientien@uoregon.edu

CONTENTS

I. Introduction	2
II. Models	4
A. Effective Scalar–SM Couplings	4
B. Higgs Portal	5
C. Other Couplings	6
III. Background-Induced Force	7
A. Modified Mass of Ordinary Matter	7
B. Modified Scalar Distribution	9
1. Scattering Theory Formalism	10
2. Spherically Symmetric Limit	13
C. Ensemble Averages and Multipole Expansion	14
1. Phase-Space Ensemble Average	15
2. Multipole Expansion	18
D. Final Expressions	20
IV. Equivalence Principle Tests	22
A. Kinematics	23
B. Force Projection and Frequency Band Structure	26
C. Revised MICROSCOPE Constraints	30
D. Future Experimental Probes and Analyses	34
V. Discussion and Conclusion	38
Acknowledgement	38
A. Dilaton Charges	38
1. Scalar–SM Coupling	39
2. Atomic Mass	40
3. Dilaton Charge: Analytical Expressions	41
4. Nuclear Physics Inputs	43
B. Spherically Symmetric Ansatz	45
C. Partial Wave Analysis	47
1. Monochromatic Wave Function	48
2. Phase Space Integration	49
D. Optical Limit	54
References	58

I. INTRODUCTION

The particle nature of dark matter (DM) is one of the leading puzzles of particle physics. There is a vast zoo of potential candidates, but one particularly compelling category of candidates is ultralight dark matter (ULDM) [1]. For the masses of interest, the Galactic halo DM density corresponds to occupation numbers far above unity. As a result, the DM must be bosonic and behaves as a coherent classical wave on astrophysical scales. This wave-like nature gives rise to a variety of distinctive signatures in precision measurements. Through its interactions with Standard

Model (SM) fields, ULDM can induce variations in fundamental constants [2–5]. Such variations can be probed using precision measurements with, for example, atomic clocks [6–12], searches for anomalous accelerations and fifth forces [13–16], atom interferometers [17–20], and pulsar timing arrays [21–24]. These diverse effects have motivated a broad experimental program, making laboratory, cosmological, and astrophysical observations increasingly sensitive probes of ULDM over a wide range of masses and couplings. A review of such efforts can be found in Ref. [25].

Of particular interest are scalar ULDM models that give rise to composition-dependent forces and can therefore be probed through equivalence principle (EP) tests. Models with linear couplings are already strongly constrained by weak-EP and fifth-force searches [2, 26–28]. If a symmetry suppresses the linear interaction, however, quadratic couplings become the leading observable effect and give rise to qualitatively different phenomenology. In contrast to the linear case, quadratic couplings cause the ULDM field to be sensitive to the surrounding matter environment, and the DM background mediates an additional force that is affected by the finite density and size of massive bodies such as the Earth. This is known as the background-induced force. Since the strongest constraints for much of the scalar ULDM parameter space currently come from the MICROSCOPE EP test [14, 28], an accurate treatment of the background-induced force is essential for reliably interpreting existing bounds and assessing the sensitivity of future experiments.

Depending on whether the interaction increases or decreases the DM mass in finite-density media, matter effects give rise to either repulsive or attractive potentials, respectively. Previous studies of the repulsive case have largely relied on spherically symmetric approximations [14, 25, 29] or analyses restricted to selected scattering directions [30], while treatments including the full angular dependence have been limited to the perturbative regime [15]. The complementary attractive case has also been explored and exhibits distinct phenomenology [31, 32]. The motion of the Earth through the Galactic DM halo introduces a preferred direction, rendering the force intrinsically anisotropic. In particular, the force is no longer spherically symmetric once the ULDM de Broglie wavelength becomes comparable to the Earth’s radius, corresponding roughly to DM mass $m_\phi \gtrsim 10^{-11}$ eV. Moreover, the resulting DM wake can occur for arbitrary orientations relative to the Earth’s motion through the halo. This is particularly relevant for experiments such as MICROSCOPE, whose orbit samples a range of DM-Earth interaction geometries over time. Accurately modeling the resulting signal therefore requires accounting for the full angular dependence of the interaction, together with an appropriate averaging over the ULDM velocity distribution.

In this work we develop a scattering-theory framework that incorporates phase-space averaging, applies to both scenarios, and remains valid beyond the spherically symmetric approximation. For concreteness, we focus on the repulsive potential case. Using this framework, we compute the scalar profile and derive its optical-limit description. We further show that the resulting anisotropic force produces a characteristic frequency-band structure in EP experiments, revealing a previously unexplored signature of quadratically coupled ULDM. These results enable a consistent treatment of terrestrial and space-based probes across the relevant ULDM parameter space.

This paper is organized as follows. In Sec. II, we review several representative models of quadratically coupled scalar ULDM, including a low-energy effective theory, the Higgs portal, a universally coupled scalar, and the QCD axion. In Sec. III, we develop a quantum mechanical scattering-theory description of the background-induced force beyond the spherical approximation. We introduce a background-induced-potential form factor to quantify the deviation from spherical symmetry. Our established formalism can be used to compute the background-induced force across the full parameter space. In Sec. IV, we apply this formalism to EP experiments, using the setup of the MICROSCOPE mission as an example. We show that the angular dependence of the force produces a distinctive frequency-band structure in the experimental signal, providing a new phenomenological signature of quadratically coupled ULDM. We then derive updated MICROSCOPE constraints and demonstrate that future space-based EP tests, such as Galileo Galilei and STE-QUEST, can substantially improve their sensitivity to ULDM by leveraging the full frequency-band information. Additional technical details are presented in the appendices. Appendix A derives the dilaton charges relevant for ULDM couplings, Appendix B reviews the spherically symmetric approximation employed in previous work, Appendix C provides details of the partial-wave analysis, and Appendix D derives the optical-limit description and its connection to the full calculation in the high-mass, strongly coupled regime.

II. MODELS

We begin with a discussion of models of quadratically-coupled scalars, where we add a real scalar field ϕ to the SM. To eliminate the linear interaction term $\phi \mathcal{O}_{\text{SM}}$ and ensure that the quadratic interaction is the leading contribution, we impose a \mathbb{Z}_2 symmetry on the scalar sector under the transformation $\phi \rightarrow -\phi$. The leading interactions with the SM then take the form

$$\mathcal{L} \supset \frac{\phi^2}{2\Lambda^2} \mathcal{O}_{\text{SM}}, \quad (1)$$

where \mathcal{O}_{SM} is a CP-even operator in the SM Lagrangian, and Λ denotes the suppression scale of the effective operator.

This section introduces the benchmark models used to explore the detectability of equivalence-principle (EP) violation in the upcoming sections. We proceed in three steps. In Sec. II A, we present the effective scalar–SM couplings, which provide the widely adopted full-set parameterization of the varying fundamental constants. In Sec. II B, we discuss the Higgs portal as a concrete UV completion that induces a specific linear combination of those couplings. Finally, we briefly comment on other scenarios, including the universal coupling and the light QCD axion. Throughout the remainder of this work, we focus primarily on the effective scalar–SM couplings of Sec. II A and the Higgs portal of Sec. II B.

A. Effective Scalar–SM Couplings

Following the conventions adopted in Refs. [2, 3, 14, 25, 33], we parameterize the interactions between the scalar field and the SM by the Lagrangian

$$\mathcal{L}_{\text{int}} \supset 2\pi \frac{\phi^2}{M_{\text{pl}}^2} \left[\frac{d_e^{(2)}}{4e^2} F_{\mu\nu} F^{\mu\nu} - \frac{d_g^{(2)} \beta_s}{2g_s} G_{\mu\nu}^A G^{A\mu\nu} - d_{m_e}^{(2)} m_e \bar{\psi}_e \psi_e - \sum_{q=u,d} (d_{m_q}^{(2)} + \gamma_{m_q} d_g^{(2)}) m_q \bar{\psi}_q \psi_q \right], \quad (2)$$

where $M_{\text{pl}} = 1.22 \times 10^{19}$ GeV is the Planck mass, A is the color index, g_s is the QCD gauge coupling, $\beta_s = \partial g_s / \partial \log \mu$ is the QCD beta function, and $\gamma_{m_q} = -\partial \log m_q / \partial \log \mu$ are the anomalous dimensions of the u and d quarks. The superscript “(2)” specifies that these are the *quadratic* (as opposed to linear) couplings of the scalar. The bare mass term of the scalar is taken to be $\mathcal{L}_\phi \supset -\frac{1}{2} m_\phi^2 \phi^2$, where m_ϕ denotes the bare scalar mass in the vacuum. The mass term is not protected from quadratic corrections, but there have been model-building efforts to address this by e.g. imposing a \mathbb{Z}_N discrete symmetry [34–39] or mirror symmetry [40], exploiting field-space boundaries [41], or introducing a relaxation mechanism [25]. In Eq. (2), the effective scale $\Lambda_i \simeq M_{\text{pl}} (1/4\pi d_i^{(2)})^{1/2}$, where $i = e, g, m_e, m_u, m_d$. Note that, in the constraint plots presented in this work, we turn on only one coupling at a time while setting all other couplings to zero.

The interactions defined in Eq. (2) induce a ϕ -dependence in the fundamental constants of the SM, parameterized by the couplings $d_i^{(2)}$. Following the renormalization-scale-invariant parametrization of Ref. [3], generalized here to the case of quadratic couplings, a background value of ϕ leads to the following variations of the constants:¹

$$\frac{\Delta \alpha_{\text{em}}}{\alpha_{\text{em}}} = d_e^{(2)} \times 2\pi \frac{\phi^2}{M_{\text{pl}}^2}, \quad \frac{\Delta \Lambda_{\text{QCD}}}{\Lambda_{\text{QCD}}} = d_g^{(2)} \times 2\pi \frac{\phi^2}{M_{\text{pl}}^2}, \quad \frac{\Delta m_e}{m_e} = d_{m_e}^{(2)} \times 2\pi \frac{\phi^2}{M_{\text{pl}}^2}, \quad \frac{\Delta m_q}{m_q} = d_{m_q}^{(2)} \times 2\pi \frac{\phi^2}{M_{\text{pl}}^2}. \quad (3)$$

Here, $\alpha_{\text{em}} \simeq 1/137$ is the fine-structure constant, Λ_{QCD} denotes the QCD confinement scale, m_e denotes the electron mass, and m_q ($q = u, d$) denote the up and down quark masses. A key feature of this parameterization is that the quantities in Eq. (3) are renormalization-group (RG) invariant, and therefore constitute genuine low-energy observables. This invariance is not accidental: it is built into the structure of the interaction Lagrangian Eq. (2) through the inclusion of the anomalous dimension γ_{m_q} in the quark-mass coupling. Specifically, the operator coefficients $d_g^{(2)} \beta_s / 2g_s$

¹ The subscript “e” in $d_e^{(2)}$ denotes the electric charge, since the $\phi^2 F^2$ interaction induces a variation in the fine-structure constant α_{em} . We clarify this notation to distinguish it from $d_{m_e}^{(2)}$, the coupling multiplying $m_e \bar{\psi}_e \psi_e$, which governs the variation of the electron mass.

and $(d_{m_q}^{(2)} + \gamma_{m_q} d_g^{(2)})$ in Eq. (2) are chosen so that the physical variations $\Delta\Lambda_{\text{QCD}}/\Lambda_{\text{QCD}}$ and $\Delta m_q/m_q$ in Eq. (3) are RG-scale independent [3].

Although the couplings defined in Eqs. (3) may be used directly, it is more convenient to reorganize the up and down quark mass variation when matching onto atomic observables, since the relevant quantities are more naturally expressed in terms of the sum and difference of the up- and down-quark masses. We therefore define

$$\begin{aligned}\hat{m} &\equiv \frac{m_u + m_d}{2} && \text{(symmetric),} \\ \delta m &\equiv m_d - m_u && \text{(anti-symmetric),}\end{aligned}\tag{4}$$

which correspond to the symmetric and antisymmetric combinations of the up- and down-quark masses, respectively. Here, \hat{m} controls the pion mass through the Gell-Mann–Oakes–Renner relation given by $m_\pi^2 \propto \Lambda_{\text{QCD}} \hat{m}$ [42, 43] and thereby dominates the quark-mass dependence of nuclear binding through pion exchange, while δm characterizes isospin-symmetry breaking which thereby determines the neutron-proton mass difference. Using the definitions of \hat{m} and δm together with Eq. (3), we define the corresponding coupling strengths varying the quark masses as

$$d_{\hat{m}}^{(2)} \equiv \frac{m_d d_{m_d}^{(2)} + m_u d_{m_u}^{(2)}}{m_d + m_u} \quad \text{(symmetric),}\tag{5}$$

$$d_{\delta m}^{(2)} \equiv \frac{m_d d_{m_d}^{(2)} - m_u d_{m_u}^{(2)}}{m_d - m_u} \quad \text{(anti-symmetric).}\tag{6}$$

Although the Lagrangian in Eq. (2) is widely used in the literature (See Refs. [2, 3, 14, 33] for example) to parametrize the full set of variations of physical constants, it is important to emphasize that it is formulated at the quark level, above the QCD confinement scale. To relate this framework to observables in low-energy experiments, one must understand how the variations of fundamental constants in Eq. (3) affect both the rest masses of elementary particles and nuclear binding energies. This mapping is encoded in the dilaton charges, which were systematically studied in Refs. [2, 3]. In Appendix A, we provide a pedagogical introduction to this formalism and update the dilaton charges using modern experimental inputs.

B. Higgs Portal

The Higgs-portal model provides an ultraviolet completion of the effective theory discussed in the previous section, and was studied in Refs. [13, 44]. The interaction Lagrangian takes the renormalizable form

$$\mathcal{L}_{\text{int}} \supset 4\pi \frac{\phi^2}{M_{\text{pl}}^2} d_H^{(2)} m_h^2 H^\dagger H,\tag{7}$$

where $H = (1/\sqrt{2})(0, v+h)^T$ in unitary gauge. This modifies the Higgs mass as $m_h^2(\phi) = m_h^2(1 + 4\pi d_H^{(2)} \phi^2/M_{\text{pl}}^2)$, where $m_h \simeq 125$ GeV is the Higgs boson mass [45]. Assuming the Higgs self-coupling is unaffected, the Higgs vacuum expectation value is correspondingly shifted to $v(\phi) = v(1 + 2\pi d_H^{(2)} \phi^2/M_{\text{pl}}^2)$, where $v \simeq 246$ GeV [45].

At energies well below the Higgs mass, the ϕ -dependent shift in the Higgs VEV induces shifts in the electron, up-quark, and down-quark masses. In addition, Λ_{QCD} is indirectly modified, because the heavy quark masses (top, bottom, charm) governing the renormalization-group flow are also shifted by the scalar background [13, 44]. Matching to the effective theory in Eq. (2) gives

$$d_e^{(2)} = \frac{\alpha_{\text{em}}}{\pi} d_H^{(2)}, \quad d_g^{(2)} = \frac{2}{9} d_H^{(2)}, \quad d_{m_e}^{(2)} = d_{\hat{m}}^{(2)} = d_{\delta m}^{(2)} = d_H^{(2)}.\tag{8}$$

The coupling $d_e^{(2)}$, which governs the variation of the fine-structure constant, arises from the combination of the $\phi^2 h$ vertex and the $h\gamma\gamma$ vertex [44]. Since the $h\gamma\gamma$ vertex is generated at one loop of SM particles, $d_e^{(2)}$ is suppressed by a loop factor α_{em}/π relative to the other scalar–SM couplings, and is therefore neglected throughout this work.

Finally, we note that the scalar bare mass receives a tree-level contribution from the Higgs vacuum expectation value upon electroweak symmetry breaking. Nevertheless, the scalar can remain ultralight, provided that this contribution is either cancelled by a mass counterterm or suppressed by the imposition of an additional symmetry [25, 34, 36, 39].

C. Other Couplings

Before closing this section, we also briefly discuss two other theories that can induce the quadratic coupling considered here. The first example is the universal coupling from scalar-tensor theory [46, 47], as implemented for quadratically-coupled ULDM in Ref. [48], where the BBN constraints on this scenario were first derived. Below we briefly summarize the setup of Ref. [48]. The model assumes that the scalar field ϕ couples to the Standard Model universally through a ϕ -dependent and conformally rescaled metric, $g_{\mu\nu}(\phi) = \Omega^2(\phi) g_{\mu\nu}$, where $g_{\mu\nu}(\phi)$ denotes the Jordan-frame metric, while $g_{\mu\nu}$ denotes the Einstein-frame metric. The conformal factor $\Omega(\phi)$ is parameterized as

$$\Omega(\phi) = 1 + d_{\text{univ}}^{(2)} \times 2\pi \frac{\phi^2}{M_{\text{pl}}^2}, \quad (9)$$

where $d_{\text{univ}}^{(2)}$ is the single parameter of the model. Starting from the point-particle action in the Jordan frame and transforming to the Einstein frame as $S_{\text{SM}} = -m_{\text{SM}} \int \sqrt{g_{\mu\nu}(\phi)} dx^\mu dx^\nu = -\Omega(\phi) m_{\text{SM}} \int \sqrt{g_{\mu\nu}} dx^\mu dx^\nu$, one finds that every elementary or composite SM particle mass rescales universally as $m_{\text{SM}}(\phi) = \Omega(\phi) m_{\text{SM}}$. For hadrons, this universality is inherited from rescaling the QCD confinement scale, $\Lambda_{\text{QCD}}(\phi) = \Omega(\phi) \Lambda_{\text{QCD}}$, which in turn follows from requiring the UV cutoff M_{UV} to transform in the same way as all other mass scales, namely $M_{\text{UV}}(\phi) = \Omega(\phi) M_{\text{UV}}$ [48]. Since all masses rescale by the same universal factor $\Omega(\phi)$, the weak EP is manifestly preserved. The model is therefore described by a single dimensionless parameter $d_{\text{univ}}^{(2)}$. Matching to Eq. (2) and Eq. (3) gives

$$d_e^{(2)} = 0, \quad d_g^{(2)} = d_{m_e}^{(2)} = d_{\tilde{m}}^{(2)} = d_{\delta m}^{(2)} = d_{\text{univ}}^{(2)}. \quad (10)$$

The fact that $d_e^{(2)} = 0$ in this matching is physically significant: any nonzero $d_e^{(2)}$, however small, would cause the fine-structure constant α_{em} to vary with ϕ . This dependence would shift the nuclear Coulomb energy in a composition-dependent manner and thereby violate the equivalence principle (See Eq. (A10) and Eq. (A11) in Appendix A). This result is protected and can be seen in the Jordan-frame in which the scalar field decouples from the SM entirely [48]. As established in Refs. [48–52], this decoupling ensures that SM quantum corrections cannot generate particle-selective, EP-violating couplings at any loop order in the SM sector, and $d_e^{(2)}$ therefore strictly vanishes to all orders in SM perturbation theory. EP violation can still arise from graviton loops, but is highly suppressed by inverse powers of M_{pl} [51]. Given the matching in Eq. (10), this model is therefore effectively immune to EP tests, but can still be constrained by fifth-force searches, which probe the overall coupling strength rather than composition-dependent differences.² For this reason, we do not consider this scenario further in the remainder of this work.

The second example is the light QCD axion [37, 38, 53], which also induces EP violation, with two distinct microscopic origins: the proton–neutron mass difference arising from isospin violation [54–56], and composition-dependent differences in nuclear binding energies [57, 58]. EP searches therefore provide a complementary probe of this scenario, independent of astrophysical or cosmological assumptions. Nevertheless, we do not pursue this case further for two reasons. First, as the axion enters the strongly-coupled regime, Earth undergoes a phase transition and scalar self-interactions become non-negligible [53]. Second, as shown in Refs. [24, 59], the parameter space within reach of current EP constraints is largely covered by existing astrophysical and terrestrial searches [53, 60–62]. For completeness, we nevertheless present in Appendix A 3 the analytical expression for the QCD-axion charge, Eq. (A15), to illustrate the microscopic origin of the EP violation.

² Strictly speaking, the above EP-conserving argument for the universal coupling applies only when the two test masses are located at the same position. In practice, a finite separation $\Delta L \sim \mathcal{O}(1)$ cm can induce a tidal differential acceleration due to the spatial variation of the ULDM field sourced by Earth’s matter through the universal coupling to the SM sector. However, this effect is suppressed as $\Delta a_{\text{bg}}/a_{\text{bg}} \lesssim \Delta L/R_\oplus \ll 1$, where a_{bg} denotes the acceleration induced by the background-induced force and the Earth’s radius R_\oplus sets the characteristic scale over which the local DM field profile varies.

III. BACKGROUND-INDUCED FORCE

The interactions discussed in the previous section can affect the behavior of both SM objects and the scalar field. The interactions in Eq. (3) lead to modifications of the mass of an object proportional to $\langle \phi^2 \rangle$, where $\langle \dots \rangle$ denotes the ensemble average over the DM distribution. Because the object mass depends on $\langle \phi^2 \rangle$, moving an object from a region of low $\langle \phi^2 \rangle$ to one of higher $\langle \phi^2 \rangle$ requires extra work. Equivalently, $\langle \phi^2 \rangle$ acts as an effective potential for the object, giving rise to a force and thus an induced acceleration. On the flip-side, when the scalar field ϕ propagates through ordinary matter, it can interact coherently with many particles if its de Broglie wavelength exceeds the interatomic spacing. This coherence modifies the propagation and distribution of ϕ , known as the *matter effect*. The matter-effect phenomenon appears in diverse contexts, including the Mikheyev-Smirnov-Wolfenstein (MSW) effect [63–69], the Meissner effect in superconductors [70], and electromagnetic reflection in metals [71]. The matter effect for quadratically-coupled ULDM was discussed in detail in Ref. [30].

In the literature, this has been called the *wake force* [15], in which the disturbance in the background field, a wake, is produced by the source and sensed by the neighboring test object. Because such a force is induced by the DM background, in contrast to the background-independent quantum force [2, 3, 27, 72–78], it is also referred to as the *background-induced force* [30, 79–84]. From a phenomenological standpoint of long-range interactions, the same underlying physical effect has also been investigated as a medium-dependent fifth force or long-range force [14, 25, 29, 74]. Throughout this work, we use the terminology *background-induced force*.

The interplay between these two above-mentioned effects – the dependence of the ϕ mass on the SM background and the converse dependence of SM parameters on ϕ – gives rise to rich phenomenology, in particular a *background-induced potential* (a.k.a. *wake potential*) imposed on the test object, which is given by

$$V_{\text{bg}}(\mathbf{r}) = -\frac{\rho_\phi}{m_\phi^2} \frac{(m_{\text{M},\mathcal{T}}^2(\mathbf{r}) \mathcal{V}_{\mathcal{T}})(m_{\text{M},\mathcal{S}}^2(\mathbf{r}) \mathcal{V}_{\mathcal{S}})}{4\pi r} \times \mathcal{F}(\mathbf{r}), \quad (11)$$

which leads to a background-induced, or wake force³

$$\mathbf{F}_{\text{bg}} = -\nabla V_{\text{bg}}, \quad (12)$$

where “bg” stands for “background.” Note that $V_{\text{bg}} \propto \rho_\phi$, the density of ϕ , and thus the potential and corresponding force vanishes in the absence of the scalar field background. The subscript “S” denotes the source object that modifies the scalar background, while “T” denotes the test object that experiences the scalar-induced force. In this work, \mathcal{S} is the Earth (denoted by \oplus) while \mathcal{T} is the test mass of the experiment (see e.g. I). $\mathcal{V}_{\mathcal{S}}$ and $\mathcal{V}_{\mathcal{T}}$ denote the volumes of the source and test objects, respectively. $m_{\text{M},\mathcal{S}}$ and $m_{\text{M},\mathcal{T}}$ correspond to the induced scalar mass due to the interactions with \mathcal{S} and \mathcal{T} , respectively. $\mathcal{F}(\mathbf{r})$ is the spatially-dependent potential form factor that describes the deviation of the background-induced potential from a Newtonian-like $1/r$ potential. For the remainder of this work, we will set $\mathcal{S} = \oplus$. In what follows, we will describe the computation of the background-induced potential.

A. Modified Mass of Ordinary Matter

We begin by expanding the discussion of how a scalar background modifies the masses of macroscopic objects. As shown in Eq. (3), when the scalar field acquires a non-zero value, it shifts the fundamental constants. As a result, the atomic mass of \mathcal{A} changes because the scalar field modifies both the rest masses of its constituent particles and the

³ Here $\mathbf{F}_{\text{bg}}|_{\mathcal{T} \leftarrow \mathcal{S}} \equiv -\nabla_{\mathcal{T}}(V_{\text{bg}}|_{\mathcal{T} \leftarrow \mathcal{S}})$ denotes the background-induced force sourced by \mathcal{S} and experienced by \mathcal{T} . The corresponding reverse force, $\mathbf{F}_{\text{bg}}|_{\mathcal{S} \leftarrow \mathcal{T}} \equiv -\nabla_{\mathcal{S}}(V_{\text{bg}}|_{\mathcal{S} \leftarrow \mathcal{T}})$, does not satisfy reciprocity, i.e., $\mathbf{F}_{\text{bg}}|_{\mathcal{T} \leftarrow \mathcal{S}} + \mathbf{F}_{\text{bg}}|_{\mathcal{S} \leftarrow \mathcal{T}} \neq \mathbf{0}$. This reflects momentum exchange between the two-body system and the scalar background. Such non-reciprocity is present in the ULDM results of Refs. [15, 30], as reflected by the fact that, in general, $\mathcal{F}(\theta_{\mathbf{r}}) \neq \mathcal{F}(\theta_{\mathbf{r}} + \pi)$. Similar discussions of the non-reciprocity of the force also arise in the context of optical binding [85, 86]. Since $M_{\mathcal{S}} \gg M_{\mathcal{T}}$, the force on \mathcal{S} is negligible, and we use V_{bg} and \mathbf{F}_{bg} as shorthand for $V_{\text{bg}}|_{\mathcal{T} \leftarrow \mathcal{S}}$ and $\mathbf{F}_{\text{bg}}|_{\mathcal{T} \leftarrow \mathcal{S}}$ throughout this work.

	Object	$(Q_{\mathcal{A}})_g$	$(Q_{\mathcal{A}})_e$ [$\times 10^{-3}$]	$(Q_{\mathcal{A}})_{m_e}$ [$\times 10^{-4}$]	$(Q_{\mathcal{A}})_{\hat{m}}$ [$\times 10^{-3}$]	$(Q_{\mathcal{A}})_{\delta m}$ [$\times 10^{-4}$]	$(Q_{\mathcal{A}})_H$ [$\times 10^{-3}$]
Source Mass \mathcal{S}	\oplus	1	2.0 (1.9)	2.7	97.1 (81.0)	0.3 (0.4)	297.9 (285.4)
Test Mass \mathcal{T}	Ti	1	2.3	2.5	98.8 (82.7)	0.9 (1.3)	299.4 (286.9)
	Pt	1	4.2	2.2	101.5 (85.4)	2.2 (3.2)	301.6 (289.1)
	Ti – Pt	0	–1.9	0.3	–2.7	–1.3 (–1.9)	–2.2

TABLE I. Numerical values of the dilaton charges for the source mass (the Earth, \oplus) and the test masses (Ti and Pt) in the MICROSCOPE experiment. “Ti” denotes the Titanium alloy and “Pt” denotes the Platinum alloy. The column “Ti – Pt” represents the difference in dilaton charge between the two test masses. Analytical expressions and the numerical evaluation of these charges are given in Appendix A. For our fiducial values, we use the updated hadronic inputs listed in Table A.1. The values in parentheses are obtained using the same analytical dilaton-charge formulas, but with the hadronic inputs adopted by Damour and Donoghue (DD 2010) [2, 3]. Entries without parentheses are unchanged at the displayed precision.

nuclear binding energy, as shown in Appendix A. Consequently, the mass of the ordinary matter varies as ⁴

$$\frac{\Delta M_{\mathcal{A}}}{M_{\mathcal{A}}} = \alpha_{\mathcal{A}}^{(2)} \times \frac{2\pi\phi^2}{M_{\text{pl}}^2} \quad (\mathcal{A} = \oplus, \mathcal{T}). \quad (13)$$

Here, $\alpha_{\mathcal{A}}^{(2)}$ is the effective coupling between the scalar and the object \mathcal{A} . For the full sets of the effective scalar–SM coupling given by Sec. II A, we have

$$\alpha_{\mathcal{A}}^{(2)} = (Q_{\mathcal{A}})_g d_g^{(2)} + (Q_{\mathcal{A}})_e d_e^{(2)} + (Q_{\mathcal{A}})_{m_e} (d_{m_e}^{(2)} - d_g^{(2)}) + (Q_{\mathcal{A}})_{\hat{m}} (d_{\hat{m}}^{(2)} - d_g^{(2)}) + (Q_{\mathcal{A}})_{\delta m} (d_{\delta m}^{(2)} - d_g^{(2)}), \quad (14)$$

where the $(Q_{\mathcal{A}})_i$ are the “dilaton charges” [2, 3] that quantify the material-dependent response of $M_{\mathcal{A}}$ to the dimensionless scalar–SM coupling $d_i^{(2)}$. For example, in the renormalizable Higgs portal (Sec. II B), we have

$$\begin{aligned} \alpha_{\mathcal{A}}^{(2)} &= \{(2/9) + (\alpha_{\text{em}}/\pi)(Q_{\mathcal{A}})_e + (7/9)[(Q_{\mathcal{A}})_{m_e} + (Q_{\mathcal{A}})_{\hat{m}} + (Q_{\mathcal{A}})_{\delta m}]\} d_H^{(2)} \\ &\equiv (Q_{\mathcal{A}})_H d_H^{(2)}. \end{aligned} \quad (15)$$

In Appendix A, we present the derivation of $(Q_{\mathcal{A}})_H$ and more generally the dilaton charges, together with the updated numerical inputs from atomic and nuclear physics for the scalar models introduced in Sec. II. As a reminder, in this work the object \mathcal{A} refers to either the Earth or a test mass \mathcal{T} , since the scalar field modifies the masses of both. In Table I, we present the numerical values of the dilaton charges for the source, $\mathcal{S} = \oplus$, and the test masses, $\mathcal{T} = \{\text{Ti}, \text{Pt}\}$, in the MICROSCOPE experiment. “Ti” denotes the titanium alloy Ti/Al/V [90 : 6 : 4], while “Pt” denotes the platinum alloy Pt/Rh [90 : 10], where the numbers in square brackets denote the mass percentages of the constituent elements. To compute the Earth dilaton charge, we approximate the Earth composition by Fe/MgSiO₃ [32 : 68], where Fe represents the iron-core component and MgSiO₃ represents the mantle component [87]. This two-component toy model captures the dominant Earth elemental composition, Fe (32%), O (30%), Si (16%), and Mg (15%), up to subdominant elements at the few-percent level [88].⁵

The modification of the Earth and test masses has two physical consequences. First, it changes the free energy of the system, which is dominated by the Earth in our setup since $M_{\oplus} \gg M_{\mathcal{T}}$. This modifies the scalar distribution inside the Earth through an induced scalar mass term $m_{M,\oplus}$, as discussed next in Sec. III B. Second, it affects the motion of the test object \mathcal{T} through the scalar gradient. After ensemble averaging over the DM phase space, this effect is described by the background-induced potential V_{bg} , which is determined by $\langle\phi^2\rangle$. The resulting force on the

⁴ To avoid notational confusion, throughout the text we use capital M to denote the masses of macroscopic objects, such as the Earth and test masses. By contrast, lowercase m always denotes a scalar mass, either the bare scalar mass m_{ϕ} or the matter-induced scalar mass m_M .

⁵ Compared with the Fe/SiO₂ [32 : 68] approximation used in earlier EP-test literature [3, 14, 25], this choice does not qualitatively change the resulting dilaton charges, but provides a more realistic representation of the Earth’s magnesium (Mg) component.

test mass is obtained by taking the gradient of this potential, as shown in Eq. (12). We discuss this second effect in Sec. III C.

B. Modified Scalar Distribution

The interactions between the SM and scalar in a finite-density environment also modify the scalar-field dynamics. Previous studies examined the scalar’s early-Universe cosmology, where interactions with the relativistic plasma generate matter, or thermal, effects. These effects significantly alter the scalar’s cosmological evolution and can shift the resulting constraints by orders of magnitude [33, 48, 89–92] compared to the treatment with only the scalar bare mass [4]. Here, we study how the nonrelativistic (NR) matter density affects the scalar’s spatial distribution, rather than its cosmological time evolution.

We saw in the previous section that the mass of a macroscopic object is modified by the scalar field (Eq. (13)). For the object \mathcal{A} , this object acquires an additional scalar-induced density, given by $\Delta\rho_{\mathcal{A}}/\rho_{\mathcal{A}} = \alpha_{\mathcal{A}}^{(2)}(2\pi\phi^2/M_{\text{pl}}^2)$, where $\Delta\rho_{\mathcal{A}}$ can be treated as the increase of the scalar-induced free energy of the system. Since ϕ couples *quadratically* to matter, ϕ gets an effective mass in the presence of matter. The matter-induced scalar mass inside the object \mathcal{A} is thus given by

$$m_{\text{M},\mathcal{A}}^2(\mathbf{r}) = \alpha_{\mathcal{A}}^{(2)} \frac{4\pi\rho_{\mathcal{A}}(\mathbf{r})}{M_{\text{pl}}^2}. \quad (\mathcal{A} = \oplus, \mathcal{T}) \quad (16)$$

Here $\rho_{\mathcal{A}}(\mathbf{r})$ is the matter density of the object \mathcal{A} , and $\alpha_{\mathcal{A}}^{(2)} \sim d^{(2)}Q_{\mathcal{A}}$ denotes the effective scalar coupling to \mathcal{A} . In the notation $m_{\text{M},\mathcal{A}}$, “M” labels the matter-induced contribution to the scalar mass, while \mathcal{A} specifies the object in which this effective scalar mass is generated. Since the Earth dominates the scalar distribution, in this section we fix $\mathcal{A} = \oplus$ and solve for the scalar profile using only the Earth density distribution, neglecting the back-reaction from the test mass \mathcal{T} .

In general the induced mass depends on the position so ϕ obeys the Klein-Gordon equation

$$\square\phi + m_{\text{eff},\oplus}^2(\mathbf{r})\phi = 0, \quad (17)$$

where the spatially dependent scalar effective mass given by

$$m_{\text{eff},\oplus}^2(\mathbf{r}) = m_{\phi}^2 + m_{\text{M},\oplus}^2(\mathbf{r}). \quad (18)$$

To solve for the scalar configuration in the presence of a spatially-dependent matter contribution, we use the following ansatz in the NR approximation:

$$\phi(\mathbf{r}, t; \mathbf{k}) = \text{Re}[e^{-i\omega(\mathbf{k})t}\psi(\mathbf{r}; \mathbf{k})], \quad (19)$$

where \mathbf{k} labels the corresponding mode, $\omega(\mathbf{k}) = (m_{\phi}^2 + |\mathbf{k}|^2)^{1/2}$, ϕ denotes the real scalar-field, and ψ denotes its NR component.⁶ Because $|m_{\phi}\partial_t\psi|$ and $|\partial_t^2\psi|$ are much smaller than $|m_{\phi}^2\psi|$ in the NR limit, we know that ψ is only a function of the spatial coordinate \mathbf{r} , rather than the time coordinate t . Therefore, we have the Schrödinger-type equation

$$-\frac{1}{2m_{\phi}}\nabla^2\psi + V_{\text{eff},\oplus}(\mathbf{r})\psi = E_{\text{eff}}(\mathbf{k})\psi, \quad (20)$$

⁶ Another commonly used convention for the NR limit is $\phi(\mathbf{r}, t; \mathbf{k}) = \text{Re}[e^{-im_{\phi}t}\tilde{\psi}(\mathbf{r}, t; \mathbf{k})]$ [93, 94]. This is equivalent to the parameterization in Eq. (19) under the transformation $\tilde{\psi}(\mathbf{r}, t; \mathbf{k}) = e^{-iE_{\text{eff}}(\mathbf{k})t}\psi(\mathbf{r}; \mathbf{k})$ in the NR limit. In this convention, the Schrödinger-type equation takes the form $-\frac{1}{2m_{\phi}}\nabla^2\tilde{\psi} + V_{\text{eff},\oplus}(\mathbf{r})\tilde{\psi} = i\partial_t\tilde{\psi}$ in the NR limit $|m_{\phi}^2\partial_t^2\tilde{\psi}| \ll |m_{\phi}\partial_t\tilde{\psi}|$.

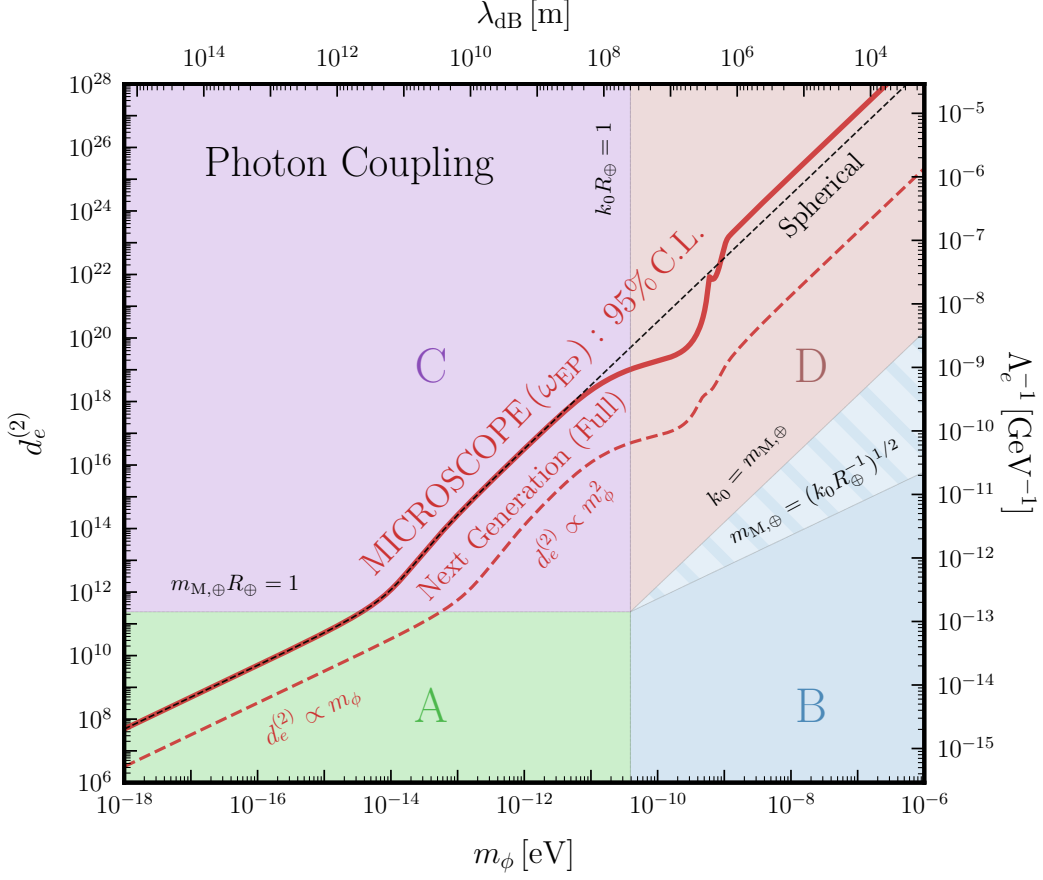


FIG. 1. Classification of the ULDM parameter space from Sec. III B 1 with the scalar–photon interaction as an example, showing the 95% C.L. constraint from MICROSCOPE as the **red solid** line (Sec. IV C) and the next-generation projected 95% C.L. sensitivity with the benchmark parameters inspired by the Galileo Galilei proposal [98–101] as the **red dashed** line (Sec. IV D). The **black dashed** line is taking the MICROSCOPE constraint in the spherically symmetric limit (Sec. III B 2). k_0 denotes the mean momentum of the ULDM and characterizes its wave-like behavior. $m_{M,\oplus}$ is the scalar mass induced by the Earth, which characterizes the interaction strength between ϕ and the SM sector, while R_\oplus is the Earth radius. In this work, the test mass \mathcal{T} is always treated as point-like. EP tests that treat the Earth as the source mass, such as MICROSCOPE [28, 102–104] and Galileo Galilei [98–101], probe regions (A), (C), and (D).

where the effective potential and the effective kinetic energy is given by

$$V_{\text{eff},\oplus}(\mathbf{r}) = \frac{m_{M,\oplus}^2(\mathbf{r})}{2m_\phi}, \quad E_{\text{eff}}(\mathbf{k}) = \frac{\mathbf{k}^2}{2m_\phi}, \quad (21)$$

respectively. In the limit where the Earth is approximated as a uniform sphere, we have $m_{M,\oplus}^2(\mathbf{r}) = m_{M,\oplus}^2 \theta(R_\oplus - |\mathbf{r}|)$, indicating that the matter-induced mass is non-zero only inside the Earth, i.e., for $|\mathbf{r}| \leq R_\oplus$. Here, $R_\oplus \simeq 6378$ km, as given in Refs. [95–97]. Since the Earth-induced potential $V_{\text{eff},\oplus}$ modifies the propagation of the scalar, the problem reduces to a standard scattering problem.

1. Scattering Theory Formalism

We can apply QM scattering theory to solve for the scalar distribution [105, 106]. Both the physical picture and the computational strategy for describing the scattering process depend on the scalar-field parameter space. In Fig. 1, we present the simplified classification of the calculation in terms of the mean scalar momentum $k_0 = m_\phi v_0$, where v_0 is the average DM speed, and the Earth-induced mass $m_{M,\oplus}$. A more detailed classification can be found in Ref. [30].

The four regions are:

- **(A): perturbative, low-momentum regime** ($m_{\text{M},\oplus}R_{\oplus} \lesssim 1$ and $k_0R_{\oplus} \lesssim 1$). The Born approximation provides a valid description of the scattering, since the scattering is perturbative ($|\psi_{\text{sc}}| \lesssim |\psi_0|$). In this regime, the source can be treated as point-like since $1/k_0 \gtrsim R_{\oplus}$, and the geometric structure of the source (the Earth) can be neglected. The behavior of \mathcal{F} depends on the distance r to the Earth center, or more specifically k_0r . On the other hand, for the near-field region $k_0r \lesssim 1$, the contributions from the bulk of the Earth and from different momentum modes add coherently to the potential, giving $\mathcal{F} = 1$. For the far-field region $k_0r \gtrsim 1$, the wave function becomes highly oscillatory. The phase cancellation induced by averaging over the finite DM phase space suppresses the potential as $\mathcal{F} \propto 1/(k_0r)^2$. This suppression is known as the *incoherence effect*.⁷
- **(B): semi-perturbative, high-momentum regime** ($m_{\text{M},\oplus} \lesssim k_0$ and $k_0R_{\oplus} \gtrsim 1$). The Born approximation remains applicable, and the form factor \mathcal{F} still exhibits perturbative behavior. However, since the full perturbative condition is more restrictive ($k_0R_{\oplus} \gtrsim 1$ and $m_{\text{M},\oplus} \lesssim (k_0/R_{\oplus})^{1/2}$) [30], we refer to this regime as “semi-perturbative.”⁸ In addition, since $k_0R_{\oplus} \gtrsim 1$, the Earth can no longer be treated as a point-object and finite-size effects come into play. Relative to region (A), the finite-size effects introduce an enhancement of $\mathcal{O}(1)$ – $\mathcal{O}(10)$ in \mathcal{F} .
- **(C): non-perturbative, low-momentum regime** ($m_{\text{M},\oplus}R_{\oplus} \gtrsim 1$ and $k_0R_{\oplus} \lesssim 1$). The Born approximation no longer holds in this regime, and we must use non-perturbative methods to calculate \mathcal{F} . In the near-field region, $k_0r \lesssim 1$, one may use the spherically symmetric ansatz of Refs. [14, 25, 29]. In this approximation, the potential is suppressed by $\mathcal{F} \simeq 3/(m_{\text{M},\oplus}R_{\oplus})^2$ compared to region (A). One factor of $1/(m_{\text{M},\oplus}R_{\oplus})$ arises from the suppression of the scalar field at the surface of the Earth, while the additional factor $3/(m_{\text{M},\oplus}R_{\oplus})$ reflects the fact that only a thin shell of thickness $m_{\text{M},\oplus}^{-1}$ contributes to the external potential, since $4\pi R_{\oplus}^2 m_{\text{M},\oplus}^{-1} \mathcal{V}_{\oplus} = 3/(m_{\text{M},\oplus}R_{\oplus})$. Both of these suppression factors are a result of the strong-coupling, which leads to a matter-induced *screening effect* of the scalar field. For the far-field region, $k_0r \gtrsim 1$, a complete treatment requires a full partial-wave analysis combined with phase-space averaging, as performed in this work.
- **(D): non-perturbative, high-momentum regime** ($m_{\text{M},\oplus} \gtrsim k_0$ and $k_0R_{\oplus} \gtrsim 1$). As in region (C), non-perturbative methods are required. Unlike in region (C), however, the spherically symmetric ansatz is no longer applicable, and one must instead use a partial-wave analysis combined with phase-space averaging for both the near- and far-field regions. For fixed $m_{\text{M},\oplus}$, increasing k_0 alleviates the screening effect in two stages. First, once $k_0R_{\oplus} \gtrsim 1$, the scalar kinetic energy is large enough to overcome the surface-gradient cost, so that the scalar wave can be pushed toward the vicinity of the potential barrier rather than being governed by the long-wavelength, spherically symmetric profile of region (C). Second, as k_0 becomes comparable to $m_{\text{M},\oplus}$, the scalar wave can further penetrate the potential barrier of the Earth. Together, these two stages progressively alleviate the *screening effect* discussed in region (C). We refer to this overall behavior as the *descreening effect*. In the high-momentum regime, the form factor is still suppressed by the *incoherence effect*. The descreening effect therefore appears as a partial compensation of the incoherence suppression found in regions (A) and (B). This saturation behavior can equivalently be understood as the approach to the optical limit discussed in Appendix D.

In the partial-wave analysis that follows, we will focus in particular on the non-perturbative regions (C) and (D), although the techniques introduced are also applicable to regions (A) and (B).

We start with the scattering between the monochromatic scalar field with momentum \mathbf{k} and the Earth. The wave function outside the Earth is represented as

$$\psi(\mathbf{r}; \mathbf{k}) = \psi_{\text{inc}}(\mathbf{r}; \mathbf{k}) + \psi_{\text{sc}}(\mathbf{r}; \mathbf{k}) \quad (r \geq R_{\oplus}), \quad (22)$$

⁷ The term “incoherence effect” here refers to the suppression caused by destructive cancellation, i.e. the loss of coherence, when integrating over the rapidly oscillating background-induced potential. This term can be viewed as the counterpart of coherent interactions between ULDM and a macroscopic object. We adopt this terminology from Refs. [80, 107]. The same effect is also referred to as the “decoherence effect” in Refs. [30, 83].

⁸ The detailed classification subdivides Region B according to whether non-perturbative features appear in the scattering cross section σ . For the background-induced force, however, this entire region remains effectively perturbative once the ULDM momentum is large enough to overcome the potential barrier, so the simplified classification suffices for our purposes.

where ψ_{inc} is the incident wave and ψ_{sc} is the scattered wave. Here, the incident wave is the plane wave $\psi_{\text{inc}} = |\psi_0| e^{i\mathbf{k}\cdot\mathbf{r}}$, where $|\psi_0| = |\phi_0|$ is the amplitude of the incident scalar wave. Using a partial-wave expansion (see Appendix C), we have

$$\psi(\mathbf{r}; \mathbf{k}) = |\psi_0| \sum_{l=0}^{\infty} (2l+1) i^l \mathcal{R}_l(kr) P_l(\cos\theta), \quad (23)$$

where $\mathcal{R}_l(kr)$ denotes the radial component of each partial wave and $\cos\theta = \hat{\mathbf{k}} \cdot \hat{\mathbf{r}}$. We focus on the wave function outside the Earth, which corresponds to the region where an Earth-orbiting satellite is located. Outside the Earth, the radial component is given by

$$\mathcal{R}_l(kr) = \underbrace{j_l(kr)}_{\text{inc}} + \underbrace{A_l h_l(kr)}_{\text{sc}} \quad (r \geq R_{\oplus}), \quad (24)$$

where the j_l term represents the incident plane wave and $A_l h_l$ represents the outgoing scattered wave. The scattered-wave coefficient A_l is obtained by matching the boundary conditions at $r = R_{\oplus}$ and is derived explicitly in Appendix C. Specifically, we have

$$A_l = -\frac{k j_l(k_{\oplus} R_{\oplus}) j_{l+1}(k R_{\oplus}) - k_{\oplus} j_l(k R_{\oplus}) j_{l+1}(k_{\oplus} R_{\oplus})}{k j_l(k_{\oplus} R_{\oplus}) h_{l+1}(k R_{\oplus}) - k_{\oplus} h_l(k R_{\oplus}) j_{l+1}(k_{\oplus} R_{\oplus})}, \quad (25)$$

where $k_{\oplus} = \sqrt{k^2 - m_{\text{M},\oplus}^2}$ is the scalar momentum inside the Earth. Importantly, the incident and scattered components converge at different partial-wave scales, which must be accounted for in the numerical computation. The incident plane wave requires partial waves up to $l_{\text{max}} \sim kr$, whereas the scattered wave is controlled by the size of the Earth and converges at $l_{\text{max}} \sim kR_{\oplus}$. Therefore, numerical computations must sum the plane-wave contribution to sufficiently high l even after the scattered-wave contribution has converged; truncating the incident-wave expansion prematurely will produce incorrect results.

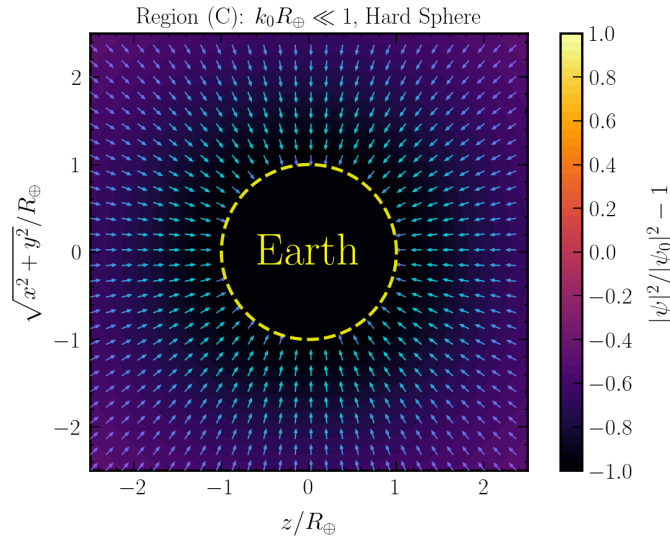


FIG. 2. Configuration of $|\psi|^2/|\psi_0|^2 - 1$ in the hard-sphere limit $m_{\text{M},\oplus} R_{\oplus} \gg 1$ with $k_0 R_{\oplus} \ll 1$, as previously discussed in Refs. [14, 25, 29]. This configuration corresponds to region (C) in Fig. 1. Matching the boundary conditions suppresses the scalar field at the surface of the sphere, giving $|\psi(r = R_{\oplus})|/|\psi_0| = 1/(m_{\text{M},\oplus} R_{\oplus})$, which reveals the screening effect. The arrows indicate the direction of the background-induced force, while their lightness of their color represents its magnitude. In this limit, the background-induced force is an attractive central force that vanishes both at the Earth's surface and asymptotically far from the Earth.

2. Spherically Symmetric Limit

Before proceeding, we discuss the $k_0 R_\oplus \ll 1$ limit where the solution to Eq. (20) has a simple analytical form and captures the main features of the screening effect. In this limit, it is sufficient to keep only the s -wave ($l = 0$) component and the system is spherically symmetric in the near-field region. The corresponding scattered-wave coefficient can be written as

$$A_0 = -i \frac{m_{M,\oplus} R_\oplus - \tanh(m_{M,\oplus} R_\oplus)}{m_{M,\oplus} R_\oplus} k R_\oplus + \dots, \quad (26)$$

where “...” denotes higher-order terms in the $k R_\oplus$ expansion. Noting that $h_0(kr) = -ie^{ikr}/kr$, the wavefunction outside the Earth is given by $\psi(\mathbf{r}; \mathbf{k}) \simeq |\psi_0| [e^{i\mathbf{k}\cdot\mathbf{r}} - iA_0 e^{ikr}/kr]$. For a satellite in near-Earth orbit, we have $r/R_\oplus \sim \mathcal{O}(1)$. Therefore, in the s -wave limit of $k_0 R_\oplus \ll 1$, we also have $k_0 r \ll 1$, and the exterior scalar profile reduces to

$$\psi_{\text{sph}}(r) \simeq |\psi_0| \left[1 - \frac{m_{M,\oplus}^2 \mathcal{V}_\oplus}{4\pi r} J_+(m_{M,\oplus} R_\oplus) \right] \quad (r \geq R_\oplus), \quad (27)$$

where the constant term is the incident plane wave and the $1/r$ term is the scattered s -wave contribution. $J_+ = 3[x - \tanh(x)]/x^3$ characterizes the screening behavior due to the induced mass and

$$J_+(m_{M,\oplus} R_\oplus) \simeq \begin{cases} 1, & m_{M,\oplus} R_\oplus \lesssim 1 \text{ Region (A)} \\ 3/(m_{M,\oplus} R_\oplus)^2, & m_{M,\oplus} R_\oplus \gtrsim 1 \text{ Region (C)} \end{cases} \quad (28)$$

and $\mathcal{V}_\oplus = 4\pi R_\oplus^3/3$ is the volume of the Earth. As an independent cross-check, the same configuration also follows from the spherically symmetric ansatz of Refs. [14, 25, 29], as reviewed in detail in Appendix B. In the hard sphere regime (C), where $m_{M,\oplus} R_\oplus \gg 1, k_0 R_\oplus \ll 1$, we have $\psi_{\text{sph}} \simeq |\psi_0| h/(R_\oplus + h)$, indicating that in this limit, at low altitudes the scalar field roughly linearly decreases with the height h . In Fig. 2, we show the field profile $\psi_{\text{sph}}^2/|\psi_0|^2 - 1$, which is spherically symmetric and exhibits the screening effect near the Earth’s surface.

Connecting Eq. (27) back to Eq. (11), we define the spherically symmetric potential form factor

$$\mathcal{F}_{\text{sph}}(r) = J_+(m_{M,\oplus} R_\oplus) \times \left[1 - \frac{1}{2} \frac{m_{M,\oplus}^2 \mathcal{V}_\oplus}{4\pi r} J_+(m_{M,\oplus} R_\oplus) \right], \quad (29)$$

which encodes the screening ($\mathcal{F}_{\text{sph}} = 1$ in the unscreened limit.) We see J_+ governs the behavior of $\mathcal{F}_{\text{sph}}(r)$, and therefore Eq. (29) follows the same behavior as Eq. (28) in which the potential is suppressed compared to the unscreened limit. From Eq. (27), we can compute the background-induced force for the spherically symmetric limit as

$$\mathbf{F}_{\text{bg}} = -\frac{\rho_\phi}{m_\phi^2} \frac{(m_{M,\mathcal{T}}^2 \mathcal{V}_{\mathcal{T}})(m_{M,\oplus}^2 \mathcal{V}_\oplus)}{4\pi r^2} \times r^2 \frac{d}{dr} \left(\frac{\mathcal{F}_{\text{sph}}(r)}{r} \right) \hat{\mathbf{r}}, \quad (30)$$

where the last term is

$$r^2 \frac{d}{dr} \left(\frac{\mathcal{F}_{\text{sph}}(r)}{r} \right) = J_+(m_{M,\oplus} R_\oplus) \times \left[1 - \frac{m_{M,\oplus}^2 \mathcal{V}_\oplus}{4\pi r} J_+(m_{M,\oplus} R_\oplus) \right], \quad (31)$$

which quantifies the screening effect and deviation from a Newtonian-type $1/r^2$ force. From Eq. (30) and Fig. 2, we see that within the spherically symmetric ansatz, the background-induced force is always a central force. Moreover, Eq. (31) is always positive, so this central background-induced force is always attractive in the spherically symmetric

ansatz [14, 25, 29]. For a satellite at a height h above the Earth's surface, we have

$$\text{screening factor: } r^2 \frac{d}{dr} \left(\frac{\mathcal{F}_{\text{sph}}(r)}{r} \right) \simeq \begin{cases} 1 & (m_{M,\oplus} R_\oplus \lesssim 1) \\ \frac{3}{(m_{M,\oplus} R_\oplus)^2} \frac{h}{R_\oplus + h} & (m_{M,\oplus} R_\oplus \gtrsim 1) \end{cases}, \quad (32)$$

where the first line is the unscreened, perturbative case while the second line shows the screening effect in the non-perturbative regime $m_{M,\oplus} R_\oplus \gtrsim 1$. As explained in Sec. III B 1, the factor $3/(m_{M,\oplus} R_\oplus)^2$ has two origins: one factor of $1/(m_{M,\oplus} R_\oplus)$ comes from the suppression of the scalar field at the Earth surface, $r = R_\oplus$. The additional factor $3/(m_{M,\oplus} R_\oplus)$ is a geometric correction that arises when the penetration depth is smaller than the Earth's radius, causing the scaling to shift from volume-based to surface-based. The factor $h/(R_\oplus + h)$ reflects the roughly linear dependence of the background-induced force on the altitude h in the low-altitude regime, and shows that this force vanishes at the Earth's surface in the hard-sphere limit.

The spherically symmetric limit provides useful insight into the behavior of EP-test constraints. In Fig. 1, which uses the photon coupling $d_e^{(2)}$ as a representative example, the black dashed curve follows the approximate scaling

$$d_i^{(2)} \propto \begin{cases} m_\phi & (m_{M,\oplus} R_\oplus \lesssim 1) \\ m_\phi^2 & (m_{M,\oplus} R_\oplus \gtrsim 1) \end{cases}, \quad (33)$$

which can be understood as follows. In the perturbative regime, $m_{M,\oplus} R_\oplus \lesssim 1$, we have $r^2 d(\mathcal{F}_{\text{sph}}/r)/dr \simeq 1$, so the background-induced force is unscreened and receives contributions from the full volumes of both the test mass and the Earth. Consequently,

$$|\mathbf{F}_{\text{bg}}| \propto \frac{m_{M,\tau}^2 m_{M,\oplus}^2}{m_\phi^2} \propto \frac{(d_i^{(2)})^2}{m_\phi^2} \quad \text{for } m_{M,\oplus} R_\oplus \lesssim 1, \quad (34)$$

implying the constraint scales as $d_i^{(2)} \propto m_\phi$. By contrast, for $m_{M,\oplus} R_\oplus \gtrsim 1$, the factor $3/(m_{M,\oplus} R_\oplus)^2$ in Eq. (32) limits the Earth's contribution. Substituting Eq. (32) into Eq. (30) shows that the force becomes independent of $m_{M,\oplus}$, yielding

$$|\mathbf{F}_{\text{bg}}| \propto \frac{m_{M,\tau}^2}{m_\phi^2} \propto \frac{d_i^{(2)}}{m_\phi^2} \quad \text{for } m_{M,\oplus} R_\oplus \gtrsim 1. \quad (35)$$

As a result, the constraint scales as $d_i^{(2)} \propto m_\phi^2$ in the screened regime.

Although this spherically symmetric ansatz is analytically simple and useful for describing the screening effect and the force behavior in the low-momentum limit, both the ansatz itself and the corresponding central-force picture break down once

$$k_0 R_\oplus \gtrsim 1 \quad \iff \quad m_\phi \gtrsim 4 \times 10^{-11} \text{ eV} \quad (\text{No Spherical Symmetry}). \quad (36)$$

In this high-momentum regime, the scalar profile becomes intrinsically non-spherical: while the force remains attractive in the forward direction, it reverses sign in the backward direction and becomes repulsive, as we show below. Therefore, the previous central-force description is no longer applicable. A proper treatment of this high-momentum regime, together with a correct description of the time-dependent signal template, requires a full partial-wave analysis combined with ensemble averaging over the DM phase space, which we discuss next.

C. Ensemble Averages and Multipole Expansion

In this section, we present a general formalism that combines the partial-wave method introduced in the previous section with the integration over DM phase space to compute the background-induced potential. Although this formalism applies throughout Fig. 1, it is particularly important in the non-perturbative, high-momentum region (D),

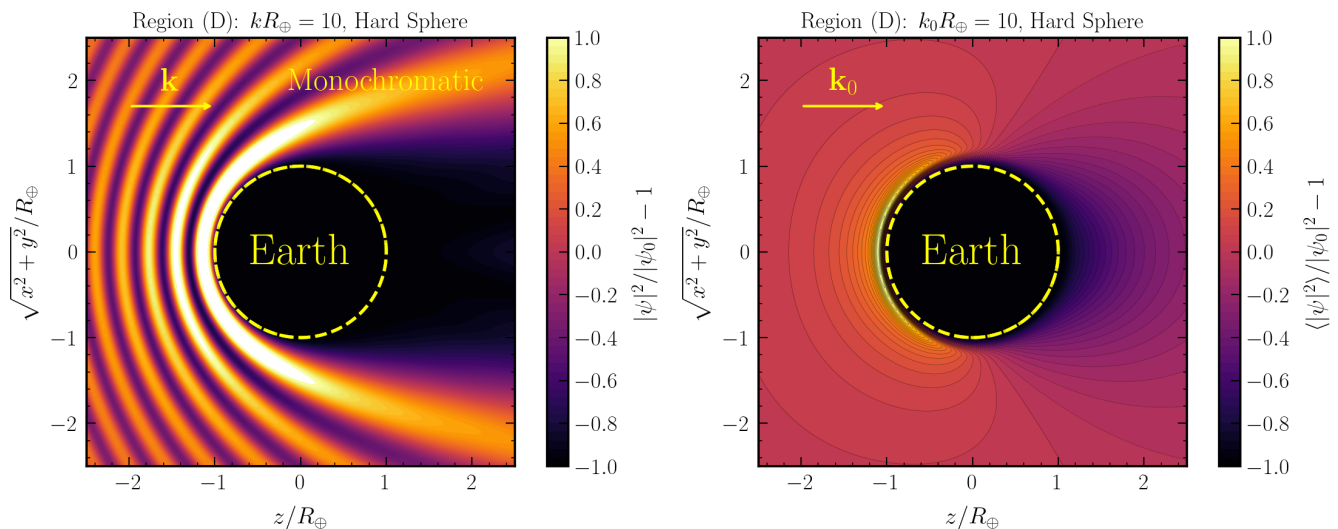


FIG. 3. The scalar field configurations in the hard-sphere limit at high incident momentum demonstrating the effect of ensemble averaging. **Left.** The scalar field configuration $|\psi|^2/|\psi_0|^2 - 1$ with monochromatic incident momentum peaked at \mathbf{k} , which satisfies $kR_\oplus = 10$. The profile becomes highly oscillatory and exhibits noticeable interference patterns. **Right.** The phase-space averaged scalar-field configuration $\langle |\psi|^2 \rangle / |\psi_0|^2 - 1$, where $\langle \dots \rangle$ denotes the ensemble average over the DM distribution in Eq. (40). Here, the mean scalar momentum satisfies $k_0 R_\oplus = 10$. The oscillatory structures in the left panel are substantially smeared out by the phase-space integration. The leading directional dependence is dominated by the dipole term a_1 . However, the scalar configuration deviations from a pure dipole pattern, indicating the presence of higher-multipole contributions.

where the simplifying approximations used in other regions break down. We present two equivalent numerical methods as cross-checks: the direct partial-wave computation used in Ref. [30], and the ensemble-averaged multipole expansion introduced in Ref. [108]. Using these methods, we compute the DM phase-space-averaged scalar profile $\langle \phi^2 \rangle$, which is a key ingredient of the background-induced potential.

1. Phase-Space Ensemble Average

Up to now, the discussion has assumed a monochromatic scalar field with momentum \mathbf{k} . We now generalize to the Maxwell-Boltzmann momentum distribution as expected for a virialized Galactic DM halo. Following the standard stochastic description of virialized ULDM [109–114], we write the real scalar field as

$$\phi(\mathbf{x}; t) = \frac{1}{2} \int d^3\mathbf{k} \left[a(\mathbf{k}) e^{-i\omega(\mathbf{k})t} \psi(\mathbf{x}; \mathbf{k}) + a^*(\mathbf{k}) e^{i\omega(\mathbf{k})t} \psi^*(\mathbf{x}; \mathbf{k}) \right], \quad (37)$$

where $a(\mathbf{k})$ is a phase-space weighted complex Gaussian random coefficient, and $a^*(\mathbf{k})$ is its complex conjugate. The random coefficient satisfies

$$\langle a(\mathbf{k}) a^*(\mathbf{k}') \rangle = (2\pi)^3 \frac{f_\phi(\mathbf{k})}{n_\phi} \delta^{(3)}(\mathbf{k} - \mathbf{k}'), \quad \langle a(\mathbf{k}) a(\mathbf{k}') \rangle = 0. \quad (38)$$

For a distribution sharply peaked at a single \mathbf{k} , Eq. (37) reduces to the monochromatic field of Eq. (19), up to an overall stochastic coefficient carried by $a(\mathbf{k})$. In the fixed-amplitude approximation, this coefficient reduces to an overall random phase. In the perturbative regime (A), where the matter effect is negligible, or sufficiently far away from the Earth where the scattered contribution becomes subdominant, the spatial part of the wave function is approximately a plane wave $\psi(\mathbf{x}; \mathbf{k}) \simeq |\psi_0| e^{i\mathbf{k}\cdot\mathbf{x}}$. In this limit, the stochastic field description reduces to the standard treatment discussed in Refs. [109–114].

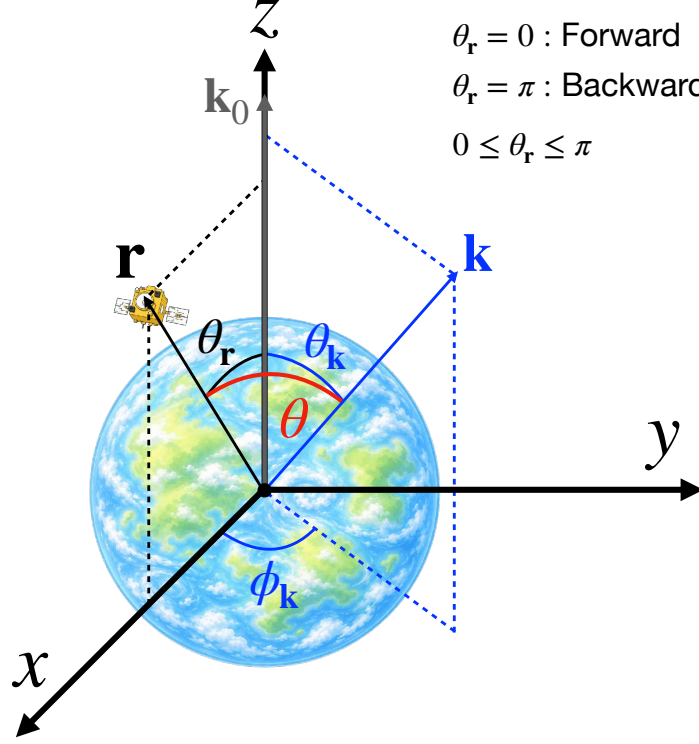


FIG. 4. Coordinate frame for phase space integration. The mean momentum \mathbf{k}_0 of the DM defines the z -axis, and the position vector \mathbf{r} lies in the x - z plane at an angle θ_r relative to \mathbf{k}_0 . The forward direction corresponds to $\theta_r = 0$, while the backward direction corresponds to $\theta_r = \pi$. A monochromatic mode in the phase space distribution is represented by \mathbf{k} , which has a polar angle θ_k and an azimuthal angle ϕ_k . $\cos \theta = \hat{\mathbf{k}} \cdot \hat{\mathbf{r}}$ defines the deflection angle in QM scattering as discussed in Sec. III B 1.

From Eq. (37) and Eq. (38), we have the ensemble average of the squared scalar field value

$$2\langle\phi^2\rangle = \langle|\psi|^2\rangle = \frac{1}{n_\phi} \int d^3\mathbf{k} f_\phi(\mathbf{k}) |\psi(\mathbf{x}; \mathbf{k})|^2. \quad (39)$$

Eq. (39) shows that there is no interference between different momentum modes after ensemble averaging. This follows directly from the $\delta^{(3)}(\mathbf{k} - \mathbf{k}')$ term in Eq. (38). Equivalently, writing $a(\mathbf{k}) = |a(\mathbf{k})| e^{i\chi(\mathbf{k})}$, the phase $\chi(\mathbf{k})$ is randomly and uniformly distributed for each momentum mode, so the cross terms between different momentum modes average to zero. The factor of “2” in Eq. (39) comes from the fast time average of a real scalar field: for any specific \mathbf{k} -mode, $\langle\phi^2\rangle = |\psi|^2 \langle\cos^2(\omega(\mathbf{k})t)\rangle = |\psi|^2/2$. In the parameter space of interest, the scalar oscillation frequency is much larger than the relevant experimental response frequencies, so this time average is valid for the observables considered here.

We describe the scalar phase-space distribution in the Solar rest frame using a boosted Maxwell–Boltzmann distribution truncated at the Galactic escape velocity,

$$f_\phi(\mathbf{k}) = \frac{n_\phi}{\mathcal{N}(k_{\text{esc}})} \left(\frac{2\pi}{\sigma_k^2}\right)^{3/2} \exp\left[-\frac{(\mathbf{k} - \mathbf{k}_0)^2}{2\sigma_k^2}\right] \Theta(k_{\text{esc}} - |\mathbf{k} - \mathbf{k}_0|), \quad (40)$$

where n_ϕ is the scalar number density. Here, $k_{\text{esc}} = m_\phi v_{\text{esc}}$, with $v_{\text{esc}} = 544$ km/s the Galactic escape speed, and $\mathbf{k}_0 = m_\phi \mathbf{v}_0$. We denote the mean DM velocity in the Solar frame by $\mathbf{v}_0 = -\mathbf{v}_\odot$, where \mathbf{v}_\odot is the Sun’s velocity relative to the Galactic rest frame, with magnitude $v_\odot \simeq 250$ km/s [115]. We neglect the Earth’s orbital motion, which produces only a subleading correction. Following the SHM [115], we take the velocity dispersion to be $\sigma_v \simeq v_{\text{LSR}}/\sqrt{2} \simeq 168$ km/s, which fixes $\sigma_k = m_\phi \sigma_v$.

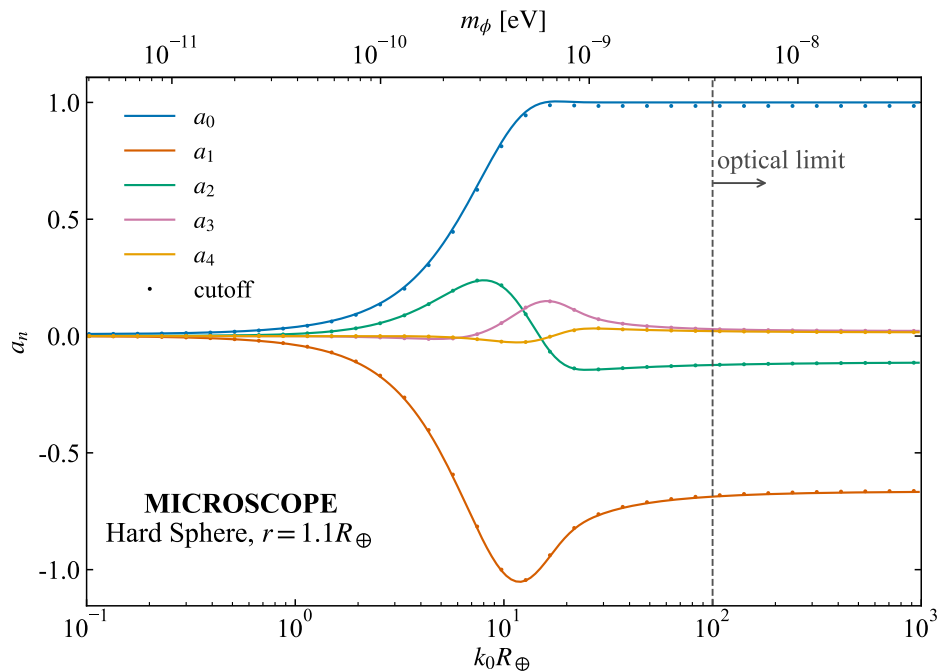


FIG. 5. Multipole coefficients a_L of $\langle |\psi|^2 \rangle$ for the first 5 moments as a function of $k_0 R_\oplus$ in the hard-sphere region (C and D) at $r = 1.1 R_\oplus$, corresponding to MICROSCOPE. **Solid** lines are computed in the infinite-cutoff limit, $k_{\text{esc}}/\sigma_k \rightarrow \infty$, while **dots** with the same colors denote the computation including the finite cutoff k_{esc} in the phase-space distribution Eq. (40). When $k_0 R_\oplus \gtrsim 100$, the system enters the optical limit and all a_L approach constant values. See Sec. III C 2 for discussion.

The normalization condition $\int d^3 \mathbf{k} f_\phi(\mathbf{k}) = n_\phi$ gives

$$\mathcal{N}(k_{\text{esc}}) = \text{erf}\left(\frac{k_{\text{esc}}}{\sqrt{2}\sigma_k}\right) - \sqrt{\frac{2}{\pi}} \frac{k_{\text{esc}}}{\sigma_k} \exp\left(-\frac{k_{\text{esc}}^2}{2\sigma_k^2}\right). \quad (41)$$

To simplify the numerical computation, we take $k_{\text{esc}}/\sigma_k \rightarrow \infty$ limit and set $\mathcal{N}(k_{\text{esc}}) \simeq 1$. We have verified that this simplification has negligible effects on our final results.

In Fig. 3, we compare the scalar profile for a monochromatic incident mode with that obtained after averaging over the phase-space distribution in Eq. (39). The left panel shows $|\psi|^2/|\psi_0|^2 - 1$ for a fixed momentum \mathbf{k} with $kR_\oplus = 10$, where the field exhibits pronounced oscillations due to interference. The right panel shows the averaged profile $\langle |\psi|^2 \rangle/|\psi_0|^2 - 1$ for $k_0 R_\oplus = 10$. Averaging over the momentum distribution in Eq. (40) smooths out the oscillatory features of the monochromatic solution. In both cases, the scalar density is enhanced on the backward hemisphere ($\cos \theta_{\mathbf{r}} \lesssim 0$), where the ULDM wind accumulates near the Earth, and suppressed on the forward hemisphere ($\cos \theta_{\mathbf{r}} \gtrsim 0$), where the Earth partially shadows the incident flux. Here, $\cos \theta_{\mathbf{r}} = \hat{\mathbf{k}}_0 \cdot \hat{\mathbf{r}}$ defines the polar angle of \mathbf{r} relative to the mean ULDM wind direction (Fig. 4). As $k_0 R_\oplus$ increases further, the scalar profile approaches the optical limit and becomes only weakly dependent on $k_0 R_\oplus$. Although the optical approximation breaks down in the weak-coupling regime (B) [15, 30, 83, 116–118], it remains valid in the strongly coupled regime (D) considered here. We also find that the shadowed region is not completely depleted after averaging over the phase-space distribution in Eq. (40) and the fraction of ULDM remains at the $\mathcal{O}(10\%)$ level. This residual density arises from the finite velocity dispersion, which allows a fraction of ULDM modes to arrive from directions substantially misaligned with the mean wind and populate the shadow region.

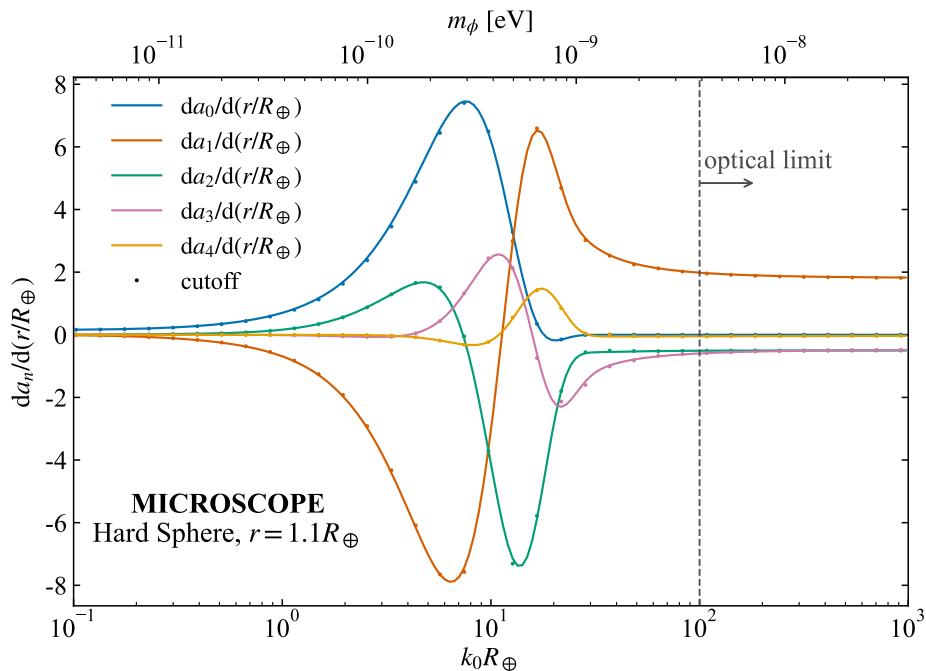


FIG. 6. The radial derivatives $da_L/d(r/R_\oplus)$ for the first 5 moments as a function of $k_0 R_\oplus$ in the hard-sphere region (C and D). **Solid** lines are computed in the infinite-cutoff limit, $k_{\text{esc}}/\sigma_k \rightarrow \infty$, while **dots** denote the computation given the finite cutoff k_{esc} in Eq. (40). When $k_0 R_\oplus \gtrsim 100$, the system enters the optical limit and $da_L/d(r/R_\oplus)$ approach constants. See Sec. III C 2 for discussion.

2. Multipole Expansion

The previous section developed the formalism and provided an intuitive picture for the ensemble average $\langle |\psi|^2 \rangle$, which is a key ingredient of the background-induced potential. The corresponding force is obtained from its spatial gradient. Previous calculations of $\langle |\psi|^2 \rangle$ either integrated the partial-wave solution over the DM phase-space distribution [30] or relied on numerical simulations with many random realizations [15]. More recently, Ref. [108] reformulated the result as a rapidly convergent multipole expansion, substantially simplifying the computation. We present this approach in this section and verify that it reproduces the direct calculation of Ref. [30] for arbitrary spatial angles in the appendices (see Fig. C.2).

Because the system is symmetric around the mean DM momentum \mathbf{k}_0 , $\langle |\psi|^2 \rangle$ is only a function of r and $\cos \theta_{\mathbf{r}} = \hat{\mathbf{k}}_0 \cdot \hat{\mathbf{r}}$. Therefore, it can be expanded as

$$\langle |\psi|^2 \rangle = |\psi_0|^2 \sum_{L=0}^{\infty} a_L(r; k_0, m_{M,\oplus}) P_L(\cos \theta_{\mathbf{r}}), \quad (42)$$

where a_L is the L -th multipole coefficient of $\langle |\psi|^2 \rangle$. The sum over L converges rapidly as L_{max} increases, and we find that truncating the multipole expansion at $L_{\text{max}} \geq 4$ is sufficient to accurately describe $\langle |\psi|^2 \rangle$.

To summarize this simplified method, we introduce two major reduction steps following Ref. [108]. The first step is to compute $|\psi|^2$ for a fixed \mathbf{k} mode by linearizing the product of two Legendre polynomials that appear in the partial-wave expansion. Next is to use the Clebsch–Gordan relation,

$$P_l(\cos \theta) P_{l'}(\cos \theta) = \sum_{L=|l-l'|}^{l+l'} \mathcal{C}_{ll'L} P_L(\cos \theta), \quad (43)$$

where the coefficients $\mathcal{C}_{ll'L}$ are listed in Eq. (C19) and $\cos \theta = \hat{\mathbf{k}} \cdot \hat{\mathbf{r}}$. Note that l labels the partial waves for a

fixed \mathbf{k} while L is for the ensemble-averaged expansion. We apply Eq. (43) to Eq. (23), integrate over the azimuthal coordinate $\phi_{\mathbf{k}}$ and after some algebra, acquire the multipole expansion in Eq. (42). Specifically, in the infinite cutoff limit $k_{\text{esc}}/\sigma_k \rightarrow \infty$, we have

$$\begin{aligned} a_L(r; k_0, m_{M,\oplus}) &= \left(\frac{1}{2\pi\sigma_k^2}\right)^{3/2} 4\pi \int_0^\infty dk k^2 \exp\left[-\frac{k^2 + k_0^2}{2\sigma_k^2}\right] c_L(r; k, m_{M,\oplus}) i_L\left(\frac{kk_0}{\sigma_k^2}\right) \\ \frac{da_L(r; k_0, m_{M,\oplus})}{dr} &= \left(\frac{1}{2\pi\sigma_k^2}\right)^{3/2} 4\pi \int_0^\infty dk k^2 \exp\left[-\frac{k^2 + k_0^2}{2\sigma_k^2}\right] \frac{dc_L(r; k, m_{M,\oplus})}{dr} i_L\left(\frac{kk_0}{\sigma_k^2}\right). \end{aligned} \quad (44)$$

Here, $i_L(x) = \sqrt{\frac{\pi}{2x}} I_{L+\frac{1}{2}}(x)$ is the spherical modified Bessel function of the first kind. We present the detailed derivation of the above multipole expansion and the generic forms of a_L and c_L for arbitrary L in Appendix C.

A particularly instructive component is the monopole coefficient a_0 :

$$a_0 = \left(\frac{1}{2\pi\sigma_k^2}\right)^{1/2} \frac{1}{k_0} \int_0^\infty dk k \left\{ \exp\left[-\frac{(k-k_0)^2}{2\sigma_k^2}\right] - \exp\left[-\frac{(k+k_0)^2}{2\sigma_k^2}\right] \right\} \times \sum_{l=0}^\infty (2l+1) |\mathcal{R}_l|^2. \quad (45)$$

a_0 corresponds to the angular average $\langle\langle |\psi|^2 \rangle\rangle_{\Omega_{\mathbf{r}}} / |\psi_0|^2 = a_0$, where $\langle\cdots\rangle_{\Omega_{\mathbf{r}}} \equiv (1/4\pi) \int d\phi_{\mathbf{r}} d\theta_{\mathbf{r}} \sin\theta_{\mathbf{r}} (\cdots)$. Eq. (45) has been used as a benchmark computation in Refs. [30, 31, 119]. In the limit $k_0/\sigma_k \rightarrow 0$, Eq. (45) reproduces the result for an isotropic phase-space distribution. In the low-momentum regime, we have

$$a_0 \simeq \psi_{\text{sph}}^2 / |\psi_0|^2, \quad \text{for } k_0 R_{\oplus} \ll 1. \quad (46)$$

In this regime, the background-induced potential is dominated by $a_0 - 1 \simeq \psi_{\text{sph}}^2 / |\psi_0|^2 - 1$, and the force is dominated by $da_0/dr \simeq d(\psi_{\text{sph}}^2 / |\psi_0|^2)/dr$. In the high-momentum regime, $k_0 R_{\oplus} \gtrsim 10$, the $L=0$ monopole contributions from da_0/dr are strongly suppressed, and the dominant ULDM signal instead comes from higher multipoles from da_L/dr with $L \geq 1$. Equivalently, angular averaging over $\Omega_{\mathbf{r}}$ corresponds to averaging over observer orientations, so the observer effectively experiences the DM wind from all directions, which leads to a suppression similar to the isotropic case. As we will see below, in the region $k_0 R_{\oplus} \gg 10$, corresponding to region (D), the MICROSCOPE constraint is dominated by the non-monopole multipoles, $L = 1, 2, \dots$, rather than by the monopole contribution with $L = 0$.

Fig. 5 and Fig. 6 show the multipole coefficients a_L and their radial derivatives for the hard-sphere limit ($m_{M,\oplus} \gtrsim k_0$ and $m_{M,\oplus} \gtrsim R_{\oplus}^{-1}$) at $r = 1.1 R_{\oplus}$, which corresponds to the MICROSCOPE orbit. Shown are the calculations with a finite and infinite momentum cutoff, and the results are in excellent agreement. Both a_L and $da_L/d(r/R_{\oplus})$ decrease rapidly with L and become negligible for $L \gtrsim 5$. In the spherically symmetric regime, $k_0 R_{\oplus} \ll 1$, which corresponds to region (C), the monopole terms a_0 and $da_0/d(r/R_{\oplus})$ dominate.⁹ However, as $k_0 R_{\oplus}$ increases and we enter region (D), the dipole contribution a_1 becomes comparable to the monopole, while the monopole derivative is suppressed and the force becomes dominated by the derivatives of the higher multipoles, particularly the dipole and quadrupole terms. This demonstrates that the spherically symmetric ansatz is no longer valid in region (D). We also find that both a_L and $da_L/d(r/R_{\oplus})$ approach constant values for $k_0 R_{\oplus} \gtrsim 100$, signaling the onset of the optical limit. In this regime, where the scalar de Broglie wavelength is much smaller than R_{\oplus} , the field behaves as a collection of classical particles and the spatial distribution of $\langle|\psi|^2\rangle$, or equivalently the scalar density ρ_ϕ , is determined primarily by geometric parameters such as r/R_{\oplus} and σ_k/k_0 . In Appendix D, we give detailed steps on computing the multipole coefficients a_L using geometric optics, which provides a simple way to compute a_L in the regime $k_0 R_{\oplus} \gg 1$ and $k_0 h \gg 1$. The latter condition ensures that the satellite altitude is much larger than the de Broglie wavelength. We have numerically verified that the resulting geometric-optics calculation agrees with the full partial-wave and phase-space-integrated calculation.

⁹ Note the same behavior holds for region (A), where $m_{M,\oplus} R_{\oplus} \lesssim 1$ and $k_0 R_{\oplus} \lesssim 1$.

D. Final Expressions

Now that we have $\langle \phi^2 \rangle (= \langle |\psi|^2 \rangle / 2)$, we can compute the background-induced potential and the corresponding force. To start with, we review the motion of the test mass \mathcal{T} driven by the scalar background following Refs. [14, 25, 30]. In the ULDM mass range considered here, the scalar oscillation frequency is much larger than the relevant experimental response frequencies. The test-mass action can therefore be written as $S_{\mathcal{T}} = \int dt L_{\mathcal{T}} = - \int dt M_{\mathcal{T}}(\langle \phi^2 \rangle) \sqrt{g_{\mu\nu} (dx^\mu/dt)(dx^\nu/dt)}$, where t is the coordinate time and $L_{\mathcal{T}}$ is the corresponding Lagrangian. Because the test mass motion is non-relativistic, and the test mass variation in terms of ϕ^2 is given in Eq. (13), the leading order Lagrangian is

$$L_{\mathcal{T}} = M_{\mathcal{T}} \frac{\mathbf{v}_{\mathcal{T}}^2}{2} - \left. \frac{dM_{\mathcal{T}}}{d\langle \phi^2 \rangle} \right|_{\phi=0} \langle \phi^2 \rangle + \dots, \quad (47)$$

where the second term containing $\langle \phi^2 \rangle$ acts as the scalar-induced potential for the test mass. Using the Euler–Lagrange equation for Eq. (47), the scalar-induced acceleration of the test mass is $\mathbf{a}_{\mathcal{T}} = -\nabla M_{\mathcal{T}}/M_{\mathcal{T}}$. Since $\mathbf{F}_{\text{bg}} = M_{\mathcal{T}} \mathbf{a}_{\mathcal{T}} = -\nabla V_{\text{bg}}$, the background-induced potential can be identified with the scalar-induced mass shift, $V_{\text{bg}} = \Delta M_{\mathcal{T}}$. Using Eq. (13), we obtain

$$V_{\text{bg}} = \alpha_{\mathcal{T}}^{(2)} \frac{4\pi M_{\mathcal{T}} \langle \phi^2 \rangle}{M_{\text{pl}}^2} + \text{const} \quad \Longleftrightarrow \quad \underbrace{V_{\text{bg}} = \frac{m_{\text{M},\mathcal{T}}^2 \mathcal{V}_{\mathcal{T}}}{4} (\langle |\psi|^2 \rangle - |\psi_0|^2)}_{\text{This work}}. \quad (48)$$

To see the equivalence between the two expressions in Eq. (48), we recall that the effective mass in the test mass medium is given by $m_{\text{M},\mathcal{T}}^2 = \alpha_{\mathcal{T}}^{(2)} (4\pi \rho_{\mathcal{T}}/M_{\text{pl}}^2)$ based on Eq. (16), $\langle \phi^2 \rangle = \langle |\psi|^2 \rangle / 2$ from $\langle \cos^2(m_{\phi} t) \rangle = 1/2$, and the test mass $M_{\mathcal{T}} = \rho_{\mathcal{T}} \mathcal{V}_{\mathcal{T}}$. Although the two representations of V_{bg} in Eq. (48) are mathematically equivalent, we use the form on the right-hand side as the default convention in this work. The reason is that the $m_{\text{M},\oplus}$ -dependence is contained in $\langle |\psi|^2 \rangle$, allowing V_{bg} to be written in a more symmetric Newtonian form with the form factor \mathcal{F} , as in Eq. (11). Note that the right-hand side of Eq. (48) fixes the additive constant such that $V_{\text{bg}} \propto \langle |\psi|^2 \rangle - |\psi_0|^2$, following similar convention to Refs. [15, 30, 116–118]. This choice is convenient because it implies

$$V_{\text{bg}} \propto \langle |\psi|^2 \rangle / |\psi_0|^2 - 1 \propto \frac{\Delta \rho_{\phi}}{\rho_{\phi}}, \quad (49)$$

since only spatial variations in the ULDM density contribute to the background-induced force.

Using the ensemble-averaged multipole expansion, we can now express the background-induced potential and the corresponding force in terms of the coefficients a_L :

$$V_{\text{bg}}(\mathbf{r}, \mathbf{k}_0) = -\frac{m_{\text{M},\mathcal{T}}^2 \mathcal{V}_{\mathcal{T}}}{4} |\psi_0|^2 \left[1 - \sum_{L=0}^{\infty} a_L(r; k_0, m_{\text{M},\oplus}) P_L(\cos \theta_{\mathbf{r}}) \right]. \quad (50)$$

To compare with the spherically symmetric scenario discussed in Sec. III B 2, we note that $\rho_{\phi} = \frac{1}{2} m_{\phi}^2 |\phi_0|^2 = \frac{1}{2} m_{\phi}^2 |\psi_0|^2$ and write

$$V_{\text{bg}}(\mathbf{r}, \mathbf{k}_0) = -\frac{|\psi_0|^2}{2} \frac{(m_{\text{M},\mathcal{T}}^2 \mathcal{V}_{\mathcal{T}})(m_{\text{M},\oplus}^2 \mathcal{V}_{\oplus})}{4\pi r} \times \mathcal{F}_{\text{sph}}(r) \times \tilde{\mathcal{F}}(\mathbf{r}, \mathbf{k}_0), \quad (51)$$

where the reduced form factor

$$\tilde{\mathcal{F}}(\mathbf{r}, \mathbf{k}_0, m_{\text{M},\oplus}) \equiv \frac{\mathcal{F}(\mathbf{r}, \mathbf{k}_0, m_{\text{M},\oplus})}{\mathcal{F}_{\text{sph}}(r, m_{\text{M},\oplus})}, \quad (52)$$

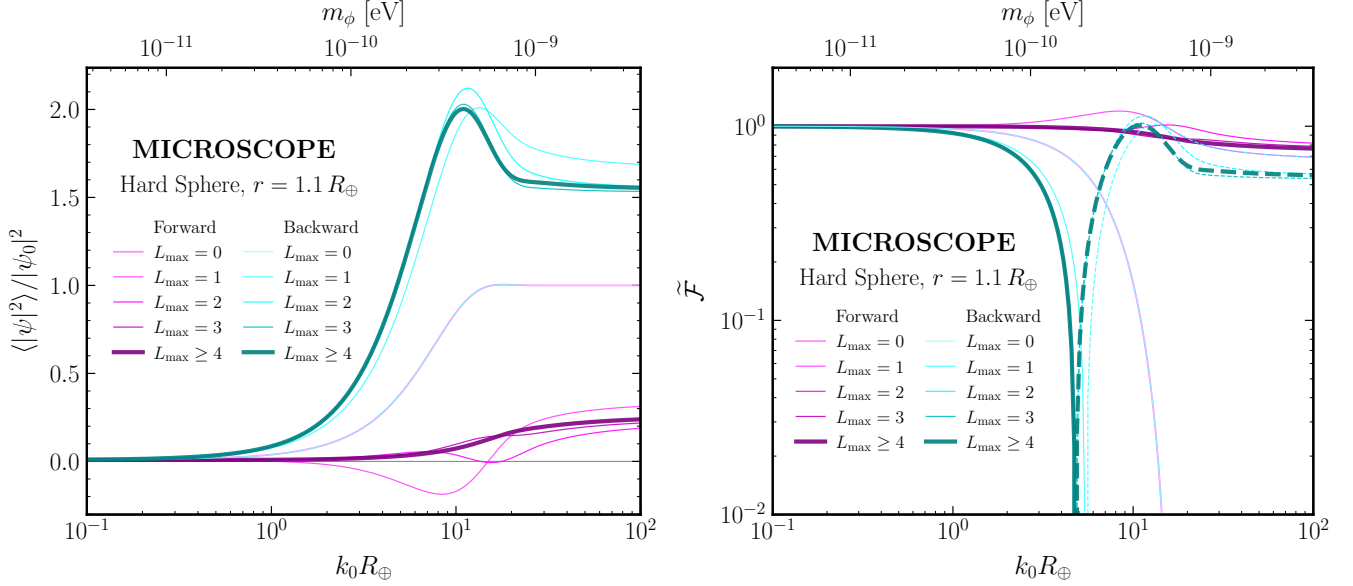


FIG. 7. Dependence of the scalar configuration $\langle |\psi|^2 \rangle / |\psi_0|^2$ (**left**) and the reduced force form factor $\tilde{\mathcal{F}}$ (**right**) on $k_0 R_\oplus$ for MICROSCOPE ($r = 1.1 R_\oplus$). The results are shown in the hard-sphere regions (C) and (D), as defined in Fig. 1. **Cyan** denotes the backward direction, $\theta_{\mathbf{r}} = \pi$. **Magenta** denotes the forward direction, $\theta_{\mathbf{r}} = 0$. The color intensity indicates the truncation order L_{\max} in the multipole expansion of Eq. (42), with darker curves corresponding to larger L_{\max} . For $L_{\max} \gtrsim 4$, the multipole expansion in Eq. (42) provides a converged description of the scalar configuration.

quantifies the deviation from the spherically symmetric ansatz. Comparing Eq. (50) and Eq. (51), we see that

$$\tilde{\mathcal{F}}(\mathbf{r}, \mathbf{k}_0, m_{M,\oplus}) = \left(\frac{2\pi r}{m_{M,\oplus}^2 \mathcal{V}_\oplus} \times \frac{1}{\mathcal{F}_{\text{sph}}(r)} \right) \times \left[1 - \sum_{L=0}^{\infty} a_L(r; k_0, m_{M,\oplus}) P_L(\cos \theta_{\mathbf{r}}) \right]. \quad (53)$$

In the limit $k_0 R_\oplus \ll 1$, we have

$$1 - \sum_{L=0}^{+\infty} a_L(r; k_0, m_{M,\oplus}) P_L(\cos \theta_{\mathbf{r}}) \simeq 1 - \frac{\psi_{\text{sph}}^2}{|\psi_0|^2} \quad \text{for } k_0 R_\oplus \ll 1. \quad (54)$$

Therefore, when $k_0 R_\oplus \ll 1$, substituting Eq. (27) into Eq. (54) and combining it with Eq. (29) gives $\tilde{\mathcal{F}} \simeq 1$, as expected from the spherically symmetric limit. However, when $k_0 R_\oplus \gtrsim 1$, this reduced form factor describes the deviation of the background-induced potential, $V_{\text{bg}} \propto \langle |\psi|^2 \rangle - |\psi_0|^2$, from the spherically symmetric ansatz. In Fig. 7, we show the dependence of the scalar configuration $\langle |\psi|^2 \rangle / |\psi_0|^2$ and $\tilde{\mathcal{F}}$ on $k_0 R_\oplus$, or equivalently on m_ϕ , for the MICROSCOPE satellite at $r = 1.1 R_\oplus$ in the forward ($\theta_{\mathbf{r}} = 0$) and backward ($\theta_{\mathbf{r}} = \pi$) directions. Fig. 7 shows that the scalar configuration and form factor behave qualitatively differently in these two directions. In the forward direction, $\langle |\psi|^2 \rangle < |\psi_0|^2$ throughout the range of $k_0 R_\oplus$ shown, indicating persistent screening of the ULDM density at the MICROSCOPE orbit, and $\tilde{\mathcal{F}}$ is always positive. In contrast, the backward direction exhibits a density enhancement for $k_0 R_\oplus \gtrsim 5$, reaching $\langle |\psi|^2 \rangle \simeq 2$ near $k_0 R_\oplus \sim 10$ due to the accumulation of ULDM behind the Earth. $\tilde{\mathcal{F}}$ goes from positive to negative at $k_0 R_\oplus \gtrsim 5$, indicating that $\langle |\psi|^2 \rangle > |\psi_0|^2$ here. As expected from the spherically symmetric limit, $\tilde{\mathcal{F}} \simeq 1$ when $k_0 R_\oplus \ll 1$.

Moving on, we define the rescaled background-induced force

$$\tilde{\mathbf{F}}_{\text{bg}} \equiv \frac{\mathbf{F}_{\text{bg}}}{|\psi_0|^2 m_{M,\mathcal{T}}^2 \mathcal{V}_{\mathcal{T}}/4} = -\nabla \left[\langle |\psi|^2 \rangle / |\psi_0|^2 \right], \quad (55)$$

which factors out the the test-mass dependence and isolates the Earth-induced contribution. Substituting the

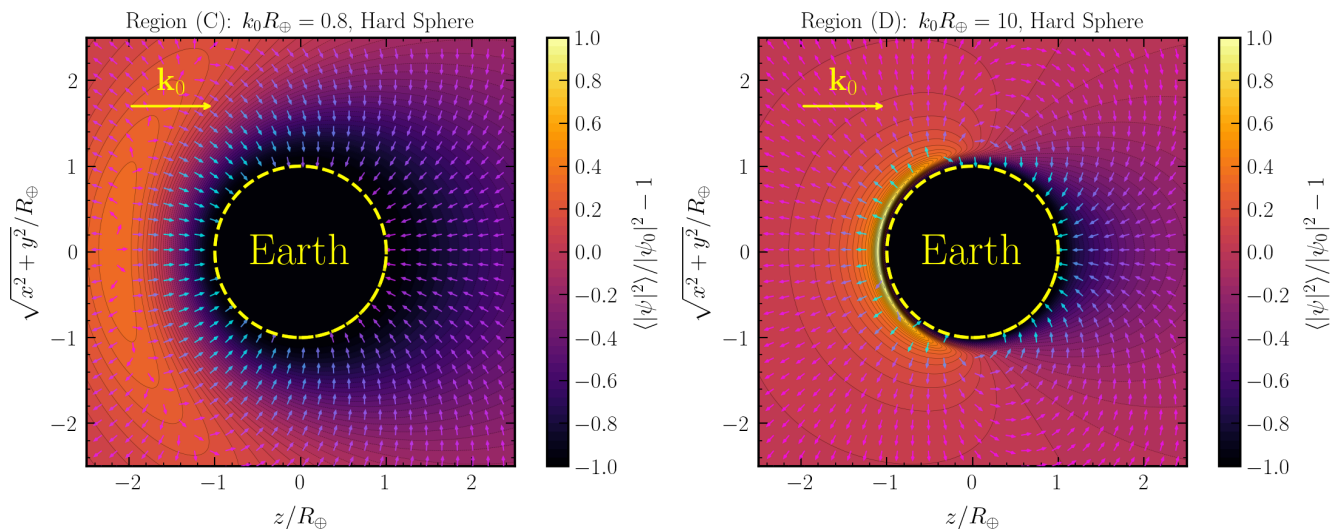


FIG. 8. Illustration of how the direction of the background-induced force changes as $k_0 R_\oplus$ increases. **Left.** $k_0 R_\oplus = 0.8$. The scalar profile starts to accumulate at a finite distance from the Earth. Near the Earth’s surface, the background-induced force still points toward the Earth, acting as an attractive force. However, the scalar configuration starts to deviate from spherical symmetry. **Right.** $k_0 R_\oplus = 10$. The system becomes strongly anisotropic. The DM wind compresses the scalar profile near the Earth’s surface in the backward hemisphere ($\cos \theta_{\mathbf{r}} \lesssim 0$). In this case, the background-induced force in the backward hemisphere reverses direction and points away from the Earth, acting as a repulsive force. By contrast, the force in the forward hemisphere ($\cos \theta_{\mathbf{r}} \gtrsim 0$) still points toward the Earth, acting as an attractive force. This strongly anisotropic force distribution at low altitude, generated by the Earth’s scattering of the high-momentum ULDM wind, is the key origin of the unique band-split signal in the MICROSCOPE frequency space discussed below.

ensemble-averaged multipole expansion of $\langle |\psi|^2 \rangle$ in Eq. (42) and evaluating the gradient in spherical coordinates, we obtain

$$\tilde{\mathbf{F}}_{\text{bg}} = \underbrace{-\hat{\mathbf{r}} \sum_L \frac{da_L}{dr} P_L(\cos \theta_{\mathbf{r}})}_{\text{Radial derivative}} + \underbrace{\frac{1}{r} (\sin \theta_{\mathbf{r}} \hat{\boldsymbol{\theta}}_{\mathbf{r}}) \sum_{L=0}^{\infty} a_L(r) P'_L(\cos \theta_{\mathbf{r}})}_{\text{Angular derivative}}, \quad (56)$$

where $\hat{\mathbf{r}} = \mathbf{r}/|\mathbf{r}|$ is the unit vector in radial direction and $\hat{\boldsymbol{\theta}}_{\mathbf{r}} = \hat{\mathbf{r}} \times (\hat{\mathbf{r}} \times \hat{\mathbf{k}}_0)/|\hat{\mathbf{r}} \times \hat{\mathbf{k}}_0|$ is the unit vector in polar angle direction, and $P'_L(\cos \theta_{\mathbf{r}}) = dP_L/d\cos \theta_{\mathbf{r}}$. Thus, the background-induced force is fully determined by a_L and da_L/dr , which characterize the angular and radial derivative of V_{bg} , respectively.

Before proceeding, we highlight one of the unique characteristics of the background-induced force, compared with the force obtained in the spherically symmetric approximation in the hard-sphere limit, as demonstrated in Fig. 8. In the left panel, where $k_0 R_\oplus = 0.8$, the scalar profile already starts to accumulate near the Earth. However, the background-induced force, denoted by the small arrows, remains attractive and points toward the Earth’s center. In the right panel, where $k_0 R_\oplus = 10$, the incident scalar momentum is large enough for the DM wind to compress the scalar profile near the Earth’s surface. In this case, the background-induced force in the backward hemisphere ($\cos \theta_{\mathbf{r}} \lesssim 0$) reverses direction and becomes repulsive, while the force in the forward hemisphere ($\cos \theta_{\mathbf{r}} \gtrsim 0$) remains attractive. This anisotropy is a key feature leading to the band-split signal in MICROSCOPE and future EP experiments, providing a unique smoking-gun signature. We will discuss this smoking-gun signature in satellite EP tests in the following section.

IV. EQUIVALENCE PRINCIPLE TESTS

The acceleration caused by the background-induced potential, given by Eq. (56), can be measured in EP tests (see Table III). As a representative example, we use the setup of the MICROSCOPE space mission [120], which operated

from April 2016 to October 2018 and tested the universality of free fall using pairs of Ti- and Pt-alloy test masses onboard the satellite. The satellite was in a nearly circular orbit around the Earth at 710 km of altitude. At this altitude, the Earth's gravitational acceleration is about 7.9 m/s^2 . The two test masses are co-axial hollow cylinders. The electrostatic accelerometers measure the acceleration of each test mass. EP violation would manifest itself as a differential acceleration between the two test masses. We define the longitudinal axis of the test-mass cylinders as $\hat{\mathbf{X}}$, along which MICROSCOPE has its greatest acceleration sensitivity.

A. Kinematics

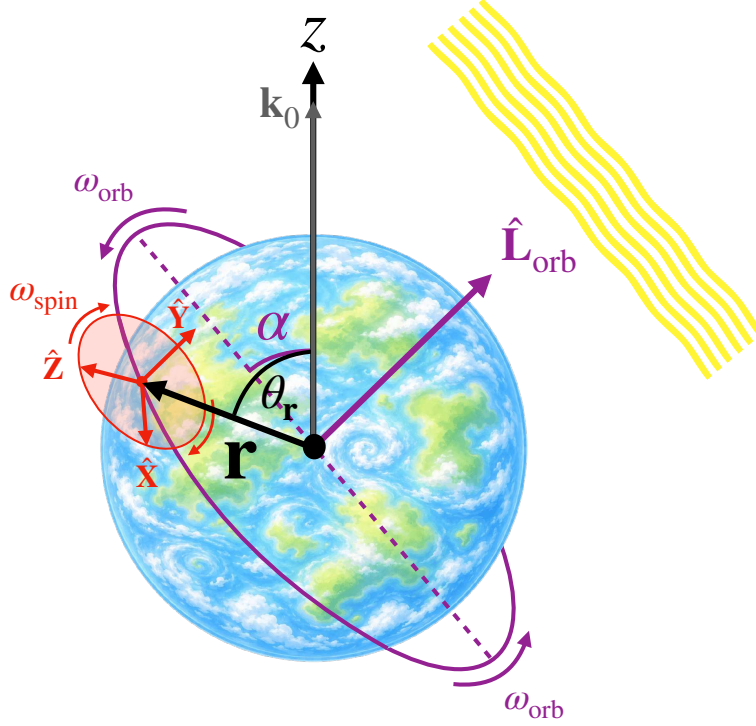


FIG. 9. The schematic plot of the coordinate system for the orbital motion of MICROSCOPE satellite. α is the angle between the MICROSCOPE orbital plane (**purple**) and the DM momentum \mathbf{k}_0 . θ_r is the angle between \mathbf{r} and \mathbf{k}_0 , where \mathbf{r} is the Earth-centered satellite position vector. The satellite orbits the Earth with angular frequency ω_{orb} . For DDSSO, the unit vector of the orbital angular momentum, $\hat{\mathbf{L}}_{\text{orb}} = \mathbf{L}_{\text{orb}}/|\mathbf{L}_{\text{orb}}|$, approximately tracks the Sun direction. In the spin mode, MICROSCOPE instrument frame (**red**) rotates with the satellite: the $\hat{\mathbf{Y}}$ axis is fixed parallel to the orbital angular momentum, $\hat{\mathbf{Y}} \equiv -\hat{\omega}_{\text{spin}} \simeq \hat{\mathbf{L}}_{\text{orb}}$, while the $\hat{\mathbf{X}}$ and $\hat{\mathbf{Z}}$ axes lie in the orbital plane and rotate about $\hat{\mathbf{Y}}$. Since the instrument-frame rotation is opposite to the orbital rotation, the EP signal frequency for spherically symmetric central force is $\omega_{\text{EP}} = \omega_{\text{spin}} + \omega_{\text{orb}}$.

The MICROSCOPE satellite operates in a dawn–dusk Sun-synchronous orbit (DDSSO); Fig. 9 shows its orbit and the orientation and rotation of the instrument axes $\hat{\mathbf{X}}$, $\hat{\mathbf{Y}}$, $\hat{\mathbf{Z}}$,¹⁰ with the Sun direction indicating the DDSSO configuration. Its orbital motion and the annual precession of the orbital plane lead to characteristic frequency-space signatures on the background-induced force. To describe these signals, we first review the DDSSO kinematics and compute the annual modulation of the angle $\alpha(t)$ between the orbital plane and the mean DM momentum \mathbf{k}_0 . We

¹⁰ The MICROSCOPE literature [28, 121, 122] uses both the instrument and satellite frames, related approximately by $\hat{\mathbf{X}}_{\text{inst}} \simeq -\hat{\mathbf{Z}}_{\text{sat}}$, $\hat{\mathbf{Y}}_{\text{inst}} \simeq \hat{\mathbf{X}}_{\text{sat}}$, and $\hat{\mathbf{Z}}_{\text{inst}} \simeq -\hat{\mathbf{Y}}_{\text{sat}}$. Throughout this work, $\hat{\mathbf{X}}$, $\hat{\mathbf{Y}}$, and $\hat{\mathbf{Z}}$ denote $\hat{\mathbf{X}}_{\text{inst}}$, $\hat{\mathbf{Y}}_{\text{inst}}$, and $\hat{\mathbf{Z}}_{\text{inst}}$, respectively.

then determine the rotation of the MICROSCOPE axes $\hat{\mathbf{X}}$, $\hat{\mathbf{Y}}$, and $\hat{\mathbf{Z}}$, and derive the geometric projection factors needed to express the background-induced force in the instrument frame.

MICROSCOPE has a local time of ascending node (LTAN) of 18:00, which corresponds to the local time at which the satellite crosses the equatorial plane from south to north. Because MICROSCOPE operated in a DDSSO, its orbital angular momentum $\hat{\mathbf{L}}_{\text{orb}}$ approximately tracked the Sun. As a result, the right ascension of the ascending node (RAAN), Ω , precessed at $\dot{\Omega} \simeq \omega_{\odot} = 360^{\circ}/\text{yr}$, where ω_{\odot} is the annual solar angular frequency.¹¹ Therefore, we have

$$\Omega - 90^{\circ} \simeq \omega_{\odot} t + \delta_{\text{orb}}. \quad (57)$$

Here, we choose $t = 0$ at the spring equinox. The small phase offset $\delta_{\text{orb}} \simeq -2.7^{\circ}$ is determined by comparing this analytic parametrization with satellite orbital data [123]. Such a positive nodal precession requires a retrograde orbit, with inclination $90^{\circ} < i_{\text{orb}} < 180^{\circ}$, where i_{orb} denotes the inclination of the satellite orbit with respect to the equatorial plane. Using the nodal-precession formula [124], we obtain

$$\cos i_{\text{orb}} \simeq -\frac{2\dot{\Omega}}{3J_2} \left(\frac{R_{\oplus} + h}{R_{\oplus}} \right)^2 \frac{1}{\omega_{\text{orb}}} \implies i_{\text{orb}} \simeq 98.2^{\circ}. \quad (58)$$

Here $\omega_{\text{orb}} = 2\pi/T_{\text{orb}}$ is the orbital angular frequency, $T_{\text{orb}} = 5946\text{s}$ is the orbital period [121, 122], and $J_2 = 1.0826 \times 10^{-3}$ is the Earth's dynamical form factor, which quantifies the deviation of the Earth's gravitational potential from spherical symmetry [95, 96]. Since MICROSCOPE followed an almost circular orbit, we neglect the orbital eccentricity. For $i_{\text{orb}} > 90^{\circ}$, the torque from the Earth's oblateness gives a positive nodal precession, so that the orbital angular momentum \mathbf{L}_{orb} precesses around the Earth's spin axis, approximately toward the north celestial pole (NCP). The orbital angular-momentum direction $\hat{\mathbf{L}}_{\text{orb}} = \mathbf{L}_{\text{orb}}/|\mathbf{L}_{\text{orb}}|$ in the ECL frame can then be written as

$$(\hat{\mathbf{L}}_{\text{orb}})_{\text{ECL}} = \begin{pmatrix} 1 & 0 & 0 \\ 0 & \cos \varepsilon & \sin \varepsilon \\ 0 & -\sin \varepsilon & \cos \varepsilon \end{pmatrix} \begin{pmatrix} \sin i_{\text{orb}} \cos(\Omega - 90^{\circ}) \\ \sin i_{\text{orb}} \sin(\Omega - 90^{\circ}) \\ \cos i_{\text{orb}} \end{pmatrix}. \quad (59)$$

where $\varepsilon = 23.44^{\circ}$ is the obliquity of the ecliptic, i.e. the angle between the ecliptic and equatorial planes [95, 96]. Here the matrix on the right-hand side of Eq. (59) is the rotation matrix from the EQU frame to the ECL frame, while the vector multiplying it is $(\hat{\mathbf{L}}_{\text{orb}})_{\text{EQU}}$, parametrized by the inclination i_{orb} and the equatorial longitude $\Omega - 90^{\circ}$ of the direction of \mathbf{L}_{orb} .

In the ECL coordinate system, the mean DM momentum direction $\hat{\mathbf{k}}_0$ is fixed and points opposite to the Cygnus (DM wind apex) direction $\hat{\mathbf{r}}_{\text{cyg}}$, as given by

$$\hat{\mathbf{k}}_0 = -\hat{\mathbf{r}}_{\text{cyg}}. \quad (60)$$

Specifically, the ECL components of $\hat{\mathbf{r}}_{\text{cyg}}$ are $\hat{\mathbf{r}}_{\text{cyg}} = (\cos \beta_{\text{cyg}} \cos \lambda_{\text{cyg}}, \cos \beta_{\text{cyg}} \sin \lambda_{\text{cyg}}, \sin \beta_{\text{cyg}})_{\text{ECL}}$ with $(\lambda_{\text{cyg}}, \beta_{\text{cyg}}) = (341.6^{\circ}, 60.6^{\circ})$, where λ_{cyg} and β_{cyg} are the ecliptic longitude and ecliptic latitude, respectively. The values of $(\lambda_{\text{cyg}}, \beta_{\text{cyg}})$ are obtained by identifying the DM wind apex direction with the solar velocity direction in the Galactic frame, $\hat{\mathbf{r}}_{\text{cyg}} = \mathbf{v}_{\odot}/|\mathbf{v}_{\odot}|$, using the velocity parameters in Ref. [115], and then transforming this direction to the ECL frame at equinox J2000 using Ref. [125].

The annual modulation of the MICROSCOPE orbit is characterized by the angle between the orbital plane and $\hat{\mathbf{k}}_0$,

$$\alpha(t) = \arcsin(\hat{\mathbf{L}}_{\text{orb}} \cdot \hat{\mathbf{k}}_0). \quad (61)$$

This angle exhibits an annual modulation due to the Earth's revolution around the Sun. In Fig. 10, we show the annual modulation of $\alpha(t)$ during the MICROSCOPE mission. To our knowledge, this modulation has not been

¹¹ We use radians and degrees interchangeably when appropriate. In discussions of satellite kinematics and astronomical coordinates, we often express angles in degrees, denoted by $^{\circ}$, following the common convention in the relevant literature.

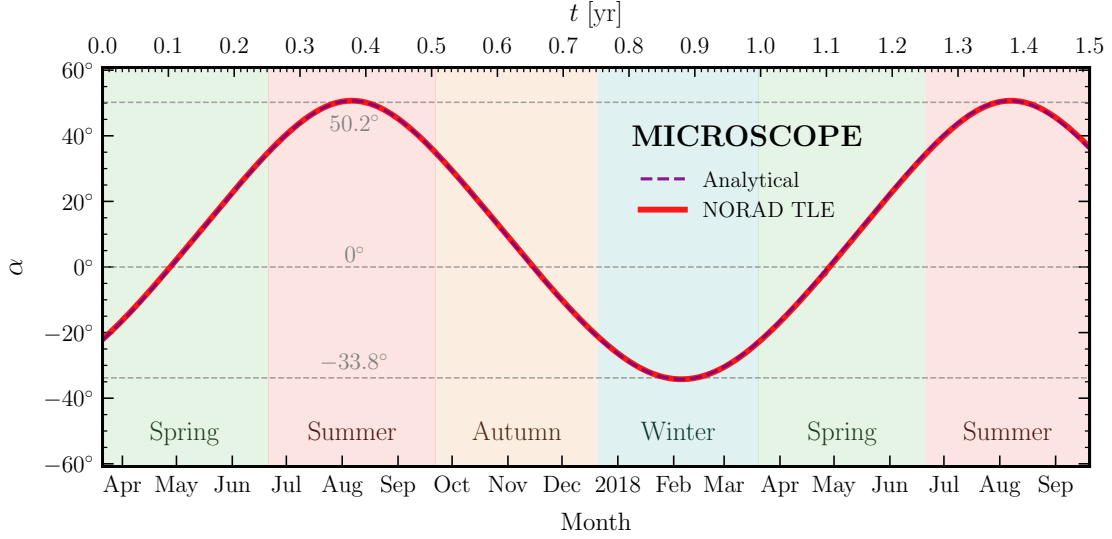


FIG. 10. Annual modulation of the angle $\alpha(t)$ between the MICROSCOPE orbital plane and the mean DM momentum \mathbf{k}_0 as the Earth orbits the Sun. The **thick red** line is computed using the real-time TLE data from NORAD [123]. The **purple dashed** line shows the analytic result, which agrees well with the TLE-based computation. Here $t = 0$ is chosen at the spring equinox in 2017.

explicitly discussed in previous MICROSCOPE EP-test analyses, which mainly focused on central-force signals. The thick red solid line is computed using satellite two-line element (TLE) data from the North American Aerospace Defense Command (NORAD). The purple dashed line shows the analytic result obtained by substituting Eq. (57), Eq. (59), and Eq. (60) into Eq. (61), and agrees well with the TLE-based result. Moreover, $\alpha(t)$ varies between -33.8° and 50.2° , where the sign specifies on which side of the orbital plane $\hat{\mathbf{k}}_0$ lies. Thus, the MICROSCOPE orbital plane is never perpendicular to $\hat{\mathbf{k}}_0$. This nonzero projection is important for the frequency band splitting in the $\hat{\mathbf{X}}$ -axis signal in the regime $k_0 R_\oplus \gtrsim 1$. Since MICROSCOPE data are collected in several-day-long sessions at different times during the mission, the annual variation of $\alpha(t)$ shown in Fig. 10 allows us to include the corresponding angular information in the data analysis, as discussed later.

We now describe the satellite orbital motion and the spin of the instrument frame. For convenience of illustration, we perform the computation in the orbital frame. We start with the position vector \mathbf{r} , the DM mean momentum \mathbf{k}_0 , and instrument axes $\hat{\mathbf{X}}, \hat{\mathbf{Y}}, \hat{\mathbf{Z}}$, as given by

$$\hat{\mathbf{r}} = \begin{pmatrix} \cos \Theta_{\text{orb}} \\ \sin \Theta_{\text{orb}} \\ 0 \end{pmatrix}_{\text{orb}}, \quad \hat{\mathbf{k}}_0 = \begin{pmatrix} 0 \\ -\cos \alpha \\ \sin \alpha \end{pmatrix}_{\text{orb}}, \quad \hat{\mathbf{X}} = \begin{pmatrix} \cos(-\Theta_{\text{spin}}) \\ \sin(-\Theta_{\text{spin}}) \\ 0 \end{pmatrix}_{\text{orb}}, \quad \hat{\mathbf{Y}} = \begin{pmatrix} 0 \\ 0 \\ 1 \end{pmatrix}_{\text{orb}}, \quad \hat{\mathbf{Z}} = \begin{pmatrix} \cos(-\frac{\pi}{2} - \Theta_{\text{spin}}) \\ \sin(-\frac{\pi}{2} - \Theta_{\text{spin}}) \\ 0 \end{pmatrix}_{\text{orb}} \quad (62)$$

where the subscript “orb” denotes components in the orbital frame, shown in purple in Fig. 9. For the orbital frame, the z -axis is given by $\hat{\mathbf{z}}_{\text{orb}} = \hat{\mathbf{L}}_{\text{orb}}$ and the x -axis of the orbital frame is given by $\hat{\mathbf{x}}_{\text{orb}} = \mathbf{L}_{\text{orb}} \times \mathbf{k}_0 / |\mathbf{L}_{\text{orb}} \times \mathbf{k}_0|$. Here, Θ_{orb} and Θ_{spin} denote the orbital and spin phases, respectively, given by

$$\Theta_{\text{orb}} = \omega_{\text{orb}} t + \Theta_{\text{orb},0}, \quad \Theta_{\text{spin}} = \omega_{\text{spin}} t + \Theta_{\text{spin},0}, \quad (63)$$

where ω_{orb} and ω_{spin} are the orbital and spin angular frequencies, and $\Theta_{\text{orb},0}$ and $\Theta_{\text{spin},0}$ are the corresponding initial phases at $t = 0$. Eq. (62) shows that $\hat{\mathbf{Z}}$ is obtained from $\hat{\mathbf{X}}$ by the substitution $\Theta_{\text{spin}} \rightarrow \Theta_{\text{spin}} + \pi/2$. Note that the MICROSCOPE satellite has multiple modes [121, 122]: inertial mode, V2 mode, and V3 mode, where the first is used

for calibration and the latter two for the EP tests. Specifically, we have

$$\underbrace{\omega_{\text{spin,inertial}} = 0}_{\text{Calibration}}, \quad \underbrace{\omega_{\text{spin},2} = \frac{9}{2}\omega_{\text{orb}}, \quad \omega_{\text{spin},3} = \frac{35}{2}\omega_{\text{orb}}}_{\text{EP Tests}}. \quad (64)$$

For a conventional fifth-force search with a spherically symmetric central force, the signal is searched for at $\omega_{\text{EP}} = \omega_{\text{spin}} + \omega_{\text{orb}}$, where the plus sign arises because the instrument-frame rotation is opposite to the orbital rotation. In the nonspherical background-induced force search as we will discuss later, the EP-violating signal contains multiple frequency bands around ω_{EP} . For consistency with previous literature, we also define $\omega_{\text{EP}} = \omega_{\text{spin}} + \omega_{\text{orb}}$.

The angle between $\hat{\mathbf{r}}$ and \mathbf{k}_0 is given by

$$\cos \theta_{\mathbf{r}} = \hat{\mathbf{k}}_0 \cdot \hat{\mathbf{r}} = -\cos \alpha \sin \Theta_{\text{orb}}, \quad (65)$$

which describes the relative angle between the satellite position vector and the mean momentum \mathbf{k}_0 . Since $\alpha(t)$ varies only on the annual timescale, the time dependence of $\theta_{\mathbf{r}}$ within a given MICROSCOPE session is dominated by the orbital period T_{orb} .

B. Force Projection and Frequency Band Structure

In this section, we project the background-induced force in Eq. (56) onto the instrument-frame axes $\hat{\mathbf{X}}$, $\hat{\mathbf{Y}}$, and $\hat{\mathbf{Z}}$, to find $\hat{\mathbf{X}} \cdot \tilde{\mathbf{F}}_{\text{bg}}$, $\hat{\mathbf{Y}} \cdot \tilde{\mathbf{F}}_{\text{bg}}$, and $\hat{\mathbf{Z}} \cdot \tilde{\mathbf{F}}_{\text{bg}}$, which determine the signal measured by the instrument. Using the kinematics discussed in Sec. IV A, we first compute the geometric factors required for the projection, namely the inner products of the instrument-frame axes with $\hat{\mathbf{r}}$ and $\hat{\theta}_{\mathbf{r}}$. We then compute the projected force and express it in both the time and frequency domains. Next, we extract the ω_{EP} component along the sensitive axis $\hat{\mathbf{X}}$, which determines the main-band Eötvös parameter used in the MICROSCOPE data analysis. We further find that the main-band amplitude carries an annual modulation through its dependence on α , an effect we incorporate into the MICROSCOPE data analysis. Finally, we discuss the main band and the orbital sidebands generated by the orbital motion. As we discuss below, these bands provide a distinctive smoking-gun signature in frequency space and can improve the detection sensitivity in a full spectral analysis.

We begin by computing the geometric factors, namely the inner products of the instrument-frame axes with $\hat{\mathbf{r}}$ and $\hat{\theta}_{\mathbf{r}}$. This is most conveniently done in the \mathbf{k}_0 -frame, where the scalar profile is axially symmetric. Using the definition of $\hat{\theta}_{\mathbf{r}}$ and the equation $|\hat{\mathbf{r}} \times (\hat{\mathbf{r}} \times \hat{\mathbf{k}}_0)| = \sin \theta_{\mathbf{r}}$, we have

$$\sin \theta_{\mathbf{r}} \hat{\theta}_{\mathbf{r}} = \hat{\mathbf{r}} \times (\hat{\mathbf{r}} \times \hat{\mathbf{k}}_0) = \cos \theta_{\mathbf{r}} \hat{\mathbf{r}} - \hat{\mathbf{k}}_0. \quad (66)$$

Using the expressions for $\hat{\mathbf{r}}$ and $\hat{\mathbf{k}}_0$ in Eq. (62), we obtain $\hat{\theta}_{\mathbf{r}}$ in the orbital frame. The geometric factors are then

$$\begin{aligned} \hat{\mathbf{r}} \cdot \hat{\mathbf{X}} &= \cos \Theta_{\text{EP}} & \hat{\mathbf{r}} \cdot \hat{\mathbf{Y}} &= 0 & \hat{\mathbf{r}} \cdot \hat{\mathbf{Z}} &= -\sin \Theta_{\text{EP}} \\ \sin \theta_{\mathbf{r}} \hat{\theta}_{\mathbf{r}} \cdot \hat{\mathbf{X}} &= -\cos \alpha \cos \Theta_{\text{orb}} \sin \Theta_{\text{EP}} & \sin \theta_{\mathbf{r}} \hat{\theta}_{\mathbf{r}} \cdot \hat{\mathbf{Y}} &= -\sin \alpha & \sin \theta_{\mathbf{r}} \hat{\theta}_{\mathbf{r}} \cdot \hat{\mathbf{Z}} &= -\cos \alpha \cos \Theta_{\text{orb}} \cos \Theta_{\text{EP}} \end{aligned} \quad (67)$$

Here, $\Theta_{\text{EP}} = \Theta_{\text{spin}} + \Theta_{\text{orb}}$. As shown in Eq. (67), the geometric factors for the $\hat{\mathbf{Z}}$ axis can be obtained from those for the $\hat{\mathbf{X}}$ axis by the substitution $\Theta_{\text{EP}} \rightarrow \Theta_{\text{EP}} + \pi/2$. This equivalence through substitution can be seen directly from Eq. (62), as $\hat{\mathbf{Z}}$ can be acquired from $\hat{\mathbf{X}}$ through $\Theta_{\text{spin}} \rightarrow \Theta_{\text{spin}} + \pi/2$, while Θ_{orb} remains the same.

Substituting Eq. (67) into Eq. (56), we obtain the projections of the background-induced force onto the three

instrument axes:

$$\begin{aligned}
\hat{\mathbf{X}} \cdot \tilde{\mathbf{F}}_{\text{bg}} &= \underbrace{\left(-\cos \Theta_{\text{EP}} \sum_{L=0}^{\infty} \frac{da_L}{dr} P_L(\cos \theta_{\mathbf{r}}) \right)}_{(\hat{\mathbf{X}} \cdot \tilde{\mathbf{F}}_{\text{bg}})_{\mathbf{r}}} + \underbrace{\left(-\cos \alpha \cos \Theta_{\text{orb}} \sin \Theta_{\text{EP}} \sum_{L=0}^{\infty} \frac{a_L(r)}{r} P'_L(\cos \theta_{\mathbf{r}}) \right)}_{(\hat{\mathbf{X}} \cdot \tilde{\mathbf{F}}_{\text{bg}})_{\hat{\theta}_{\mathbf{r}}}}, \\
\hat{\mathbf{Y}} \cdot \tilde{\mathbf{F}}_{\text{bg}} &= \underbrace{\left(-\sin \alpha \sum_{L=0}^{\infty} \frac{a_L(r)}{r} P'_L(\cos \theta_{\mathbf{r}}) \right)}_{(\hat{\mathbf{Y}} \cdot \tilde{\mathbf{F}}_{\text{bg}})_{\hat{\theta}_{\mathbf{r}}}}, \\
\hat{\mathbf{Z}} \cdot \tilde{\mathbf{F}}_{\text{bg}} &= \underbrace{\left(\sin \Theta_{\text{EP}} \sum_{L=0}^{\infty} \frac{da_L}{dr} P_L(\cos \theta_{\mathbf{r}}) \right)}_{(\hat{\mathbf{Z}} \cdot \tilde{\mathbf{F}}_{\text{bg}})_{\mathbf{r}}} + \underbrace{\left(-\cos \alpha \cos \Theta_{\text{orb}} \cos \Theta_{\text{EP}} \sum_{L=0}^{\infty} \frac{a_L(r)}{r} P'_L(\cos \theta_{\mathbf{r}}) \right)}_{(\hat{\mathbf{Z}} \cdot \tilde{\mathbf{F}}_{\text{bg}})_{\hat{\theta}_{\mathbf{r}}}}.
\end{aligned} \tag{68}$$

Since the $\hat{\mathbf{X}}$ and $\hat{\mathbf{Z}}$ lie in and rotate within the orbital plane, their projections of $\tilde{\mathbf{F}}_{\text{bg}}$ receive both radial and angular contributions, while the $\hat{\mathbf{Y}}$ projection, which is perpendicular to the plane, receives only the angular contribution.

To make the frequency band structure in Eq. (68) explicit, we expand

$$P_L(\cos \theta_{\mathbf{r}}) = \frac{1}{2^L} \sum_{k=0}^{\lfloor L/2 \rfloor} (-1)^k \binom{L}{k} \binom{2L-2k}{L} (\cos \theta_{\mathbf{r}})^{L-2k}, \tag{69}$$

where $\lfloor \dots \rfloor$ represents the floor function, and use Eq. (65). This expansion shows that the $\hat{\mathbf{X}}$ and $\hat{\mathbf{Z}}$ projections contain terms like $\cos \Theta_{\text{EP}} (\sin \Theta_{\text{orb}})^{\mathcal{N}}$ or $\sin \Theta_{\text{EP}} (\sin \Theta_{\text{orb}})^{\mathcal{N}}$, while the $\hat{\mathbf{Y}}$ projection contains terms like $(\sin \Theta_{\text{orb}})^{\mathcal{N}}$ where \mathcal{N} is a non-negative integer. This structure makes explicit that the $\hat{\mathbf{X}}$ and $\hat{\mathbf{Z}}$ projections contain a main band at ω_{EP} and orbital sidebands at $\omega_{\text{EP}} \pm n \omega_{\text{orb}}$, while the $\hat{\mathbf{Y}}$ projection has a frequency-independent (DC) main band and sidebands $n \omega_{\text{orb}}$ ($n \geq 1$). Note that for the background-induced force described in the spherically symmetric case [14, 25, 29], or the Yukawa-type central force [2, 3, 27, 72–78], the force projection in $\hat{\mathbf{X}}$ and $\hat{\mathbf{Z}}$ only has the main $n = 0$ band and no $\hat{\mathbf{Y}}$ -axis signal, and so previous MICROSCOPE analyses focused on the main ω_{EP} band [28, 102–104, 122].

We now discuss the $\hat{\mathbf{X}}$ projection in detail, since MICROSCOPE is most sensitive along this axis. Combining Eq. (65), Eq. (69) and Eq. (68), we decompose the $\hat{\mathbf{X}}$ projection as

$$\begin{aligned}
\hat{\mathbf{X}} \cdot \tilde{\mathbf{F}}_{\text{bg}} &= R_0^X \cos \Theta_{\text{EP}} \\
&+ \sum_{n=1}^{\infty} \left[(R_n^X + T_n^X) \cos \left(\Theta_{\text{EP}} + n \Theta_{\text{orb}} + \frac{n\pi}{2} \right) + (R_n^X - T_n^X) \cos \left(\Theta_{\text{EP}} - n \Theta_{\text{orb}} - \frac{n\pi}{2} \right) \right].
\end{aligned} \tag{70}$$

Here R_n^X denotes the contribution from the radial component of the force, while T_n^X denotes the contribution from the angular component.

The MICROSCOPE measurements focus on the acceleration along the $\hat{\mathbf{X}}$ direction with the frequency of ω_{EP} , which corresponds to the main-band coefficient R_0^X :

$$\text{Main band in } \hat{\mathbf{X}} \text{ } (\omega_{\text{EP}}): \quad R_0^X = -\frac{da_0}{dr} + \left(\frac{1}{2} - \frac{3}{4} \cos^2 \alpha \right) \frac{da_2}{dr} + \dots \tag{71}$$

When $k_0 R_{\oplus} \ll 1$, $da_2/dr \ll da_0/dr$, and so $R_0^X \simeq -da_0/dr \simeq -d(\psi_{\text{sph}}^2/|\psi_0|^2)/dr$, which reduces to the analytical result in Refs. [14, 25, 29]. However, as shown in Fig. 6, da_0/dr deviates from $d(\psi_{\text{sph}}^2/|\psi_0|^2)/dr$ when $k_0 R_{\oplus} \gtrsim 1$. Furthermore, when $k_0 R_{\oplus} \gtrsim 10$, da_0/dr vanishes, while da_2/dr dominates. This indicates that in this regime, the MICROSCOPE constraint from the ω_{EP} -band still holds, but is dominated by the quadrupole contribution, da_2/dr , rather than the monopole contribution, da_0/dr . Moreover, the coefficient of da_2/dr in Eq. (71) depends on α , and is therefore annually modulated. Therefore, when treating the MICROSCOPE data in different segments given by Table II, we can incorporate the annual orbit-angle modulation shown in Fig. 10.

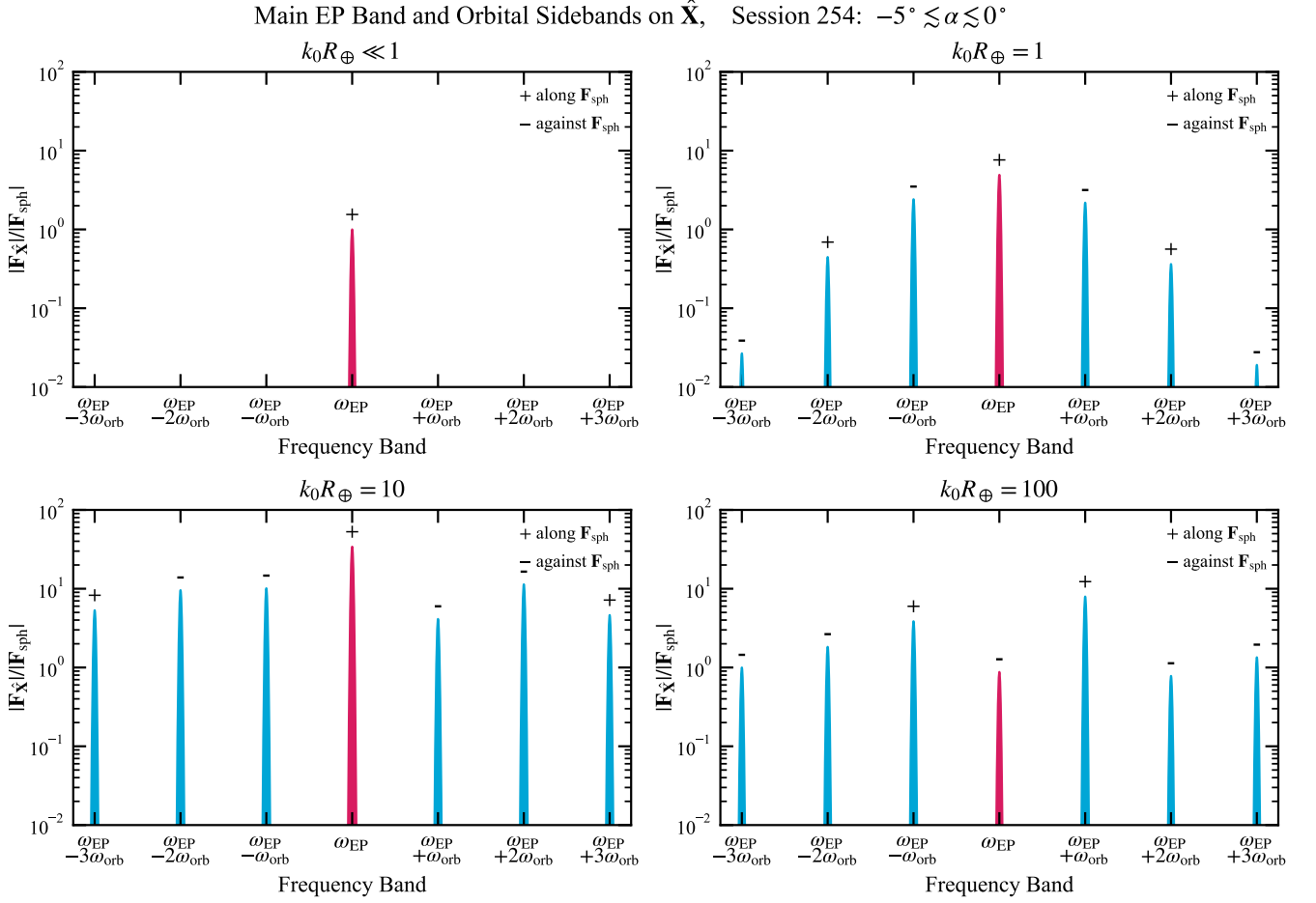


FIG. 11. Illustration of the main band and orbital sidebands of the $\hat{\mathbf{X}}$ -projected background-induced force $\mathbf{F}_{\hat{\mathbf{X}}}$ for MICROSCOPE Session 254. The vertical axis shows the relative force amplitude, $|\mathbf{F}_{\hat{\mathbf{X}}}|/|\mathbf{F}_{\text{sph}}|$, where $|\mathbf{F}_{\text{sph}}|$ is the magnitude of the background-induced force in the spherically symmetric ansatz, given in Eq. (30). The **magenta** peak denotes the main band at ω_{EP} and the **cyan** peaks denote the sidebands at $\omega_{\text{EP}} \pm \omega_{\text{orb}}$, $\omega_{\text{EP}} \pm 2\omega_{\text{orb}}$, and $\omega_{\text{EP}} \pm 3\omega_{\text{orb}}$. We assign a $+/-$ sign to each peak when the corresponding $\mathbf{F}_{\hat{\mathbf{X}}}$ component points parallel/anti-parallel to the direction of \mathbf{F}_{sph} , which points toward the Earth as shown in Fig. 2. When $k_0 R_{\oplus} \ll 1$, the background-induced force is dominated by the monopole contribution. In this limit, the signal contains a single peak at ω_{EP} , and the force has the same direction and magnitude as \mathbf{F}_{sph} . By contrast, when $k_0 R_{\oplus} \gtrsim 1$, higher multipoles become important and generate the sideband structure. Including these sidebands can improve the sensitivity, especially when $k_0 R_{\oplus} \gtrsim 100$, corresponding to $m_{\phi} \gtrsim 4 \times 10^{-9}$ eV.

We now turn to the remaining Fourier components at $\omega_{\text{EP}} \pm n\omega_{\text{orb}}$ with $n = 1, 2, 3, \dots$. Organizing them by the sideband number n , we obtain the leading terms

$$\text{First sideband in } \hat{\mathbf{X}} (\pm\omega_{\text{orb}}): \quad \begin{cases} R_1^X = \cos \alpha \left[-\frac{1}{2} \frac{da_1}{dr} + \left(\frac{3}{4} - \frac{15}{16} \cos^2 \alpha \right) \frac{da_3}{dr} + \dots \right], \\ T_1^X = \cos \alpha \left[\frac{1}{2} \frac{a_1}{r} + \left(-\frac{3}{4} + \frac{15}{16} \cos^2 \alpha \right) \frac{a_3}{r} + \dots \right]. \end{cases} \quad (72)$$

$$\text{Second sideband in } \hat{\mathbf{X}} (\pm 2\omega_{\text{orb}}): \quad \begin{cases} R_2^X = \cos^2 \alpha \left[-\frac{3}{8} \frac{da_2}{dr} + \left(\frac{15}{16} - \frac{35}{32} \cos^2 \alpha \right) \frac{da_4}{dr} + \dots \right], \\ T_2^X = \cos^2 \alpha \left[\frac{3}{4} \frac{a_2}{r} + \left(-\frac{15}{8} + \frac{35}{16} \cos^2 \alpha \right) \frac{a_4}{r} + \dots \right]. \end{cases} \quad (73)$$

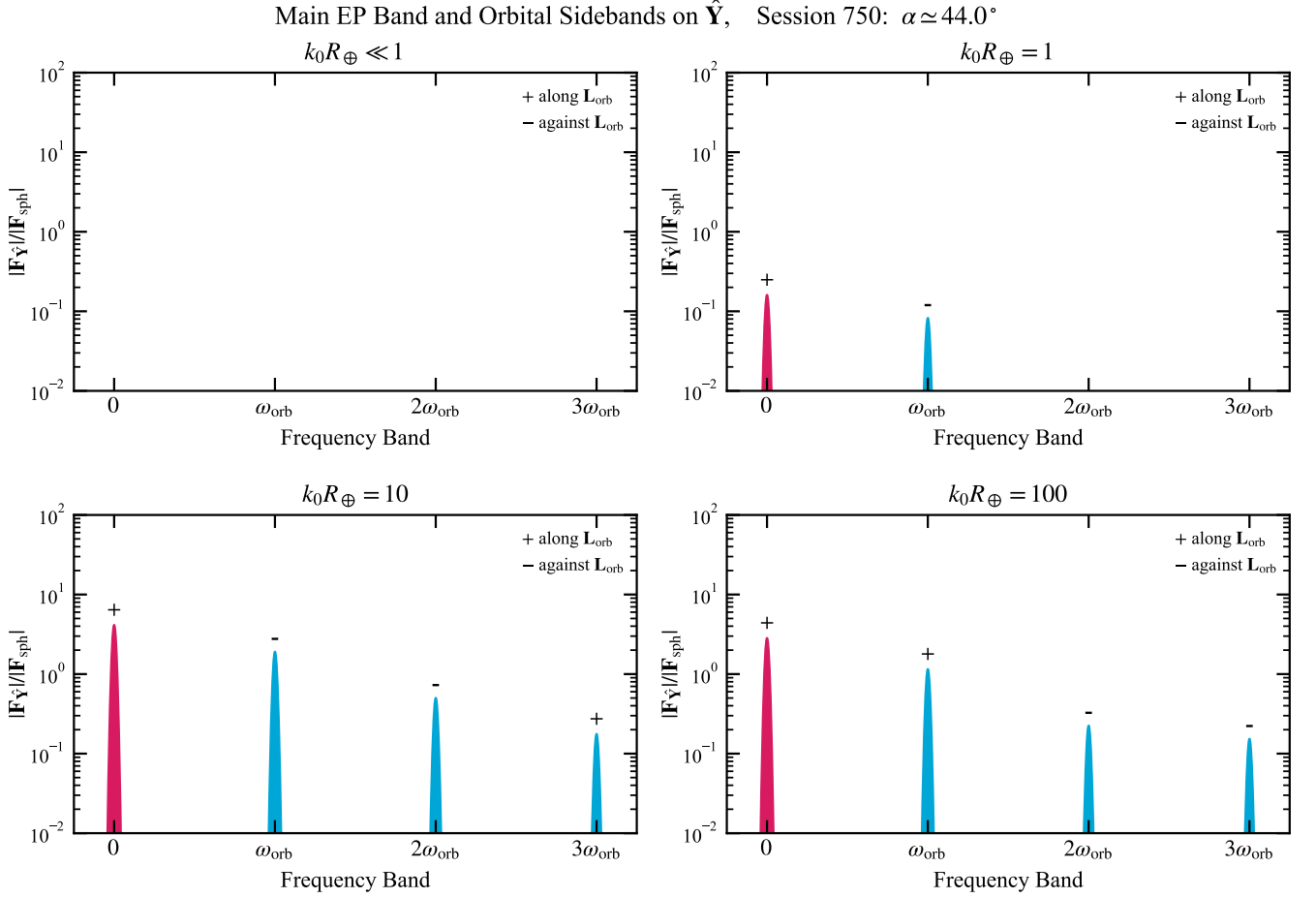


FIG. 12. Illustration of the main DC component and orbital sidebands of the $\hat{\mathbf{Y}}$ -projected background-induced force $\mathbf{F}_{\hat{\mathbf{Y}}}$ induced by the MICROSCOPE orbital motion for Session 750. The **magenta** peak denotes the main band, which gives the DC signal, where $\omega = 0$. The vertical axis shows the normalized force amplitude, $|\mathbf{F}_{\hat{\mathbf{Y}}}|/|\mathbf{F}_{\text{sph}}|$, where $|\mathbf{F}_{\text{sph}}|$ is the magnitude of the background-induced force in the spherically symmetric ansatz, given in Eq. (30). The **cyan** peaks denote the sidebands at ω_{orb} , $2\omega_{\text{orb}}$, and $3\omega_{\text{orb}}$, etc. We use +/- for each peak if the corresponding $\mathbf{F}_{\hat{\mathbf{Y}}}$ is parallel/anti-parallel to the direction of $\hat{\mathbf{L}}_{\text{orb}}$. Note that there is no signal when $k_0 R_{\oplus} \ll 1$ since there is no force on the tangential direction in spherically symmetric case.

$$\text{Third sideband in } \hat{\mathbf{X}} (\pm 3\omega_{\text{orb}}): \quad \begin{cases} R_3^X = \cos^3 \alpha \left[-\frac{5}{16} \frac{da_3}{dr} + \left(\frac{35}{32} - \frac{315}{256} \cos^2 \alpha \right) \frac{da_5}{dr} + \dots \right], \\ T_3^X = \cos^3 \alpha \left[\frac{15}{16} \frac{a_3}{r} + \left(-\frac{105}{32} + \frac{945}{256} \cos^2 \alpha \right) \frac{a_5}{r} + \dots \right]. \end{cases} \quad (74)$$

In Fig. 11, we show the relative amplitudes of the main band and orbital sidebands. We find that in the low-momentum regime ($k_0 R_{\oplus} \ll 1$), the main band dominates, because the DM field profile is nearly spherically symmetric around the Earth and a_0 dominates the series expansion. When increasing m_ϕ toward the high momentum region, $k_0 R_{\oplus} \gg 1$, the incident DM waves start to resolve the finite size of the Earth, and the contribution from a_L and da_L/dr for $L \geq 1$ become substantial, and could dominate over the spherically symmetrical contribution from a_0 . Physically speaking, for the high momentum region, the DM field would develop a non-spherical field profile $\langle |\psi|^2 \rangle$ around the Earth, with sizable dipole, quadrupole, and higher-multipole components. As a result, the signals probed by the satellite experience an extra ‘‘orbital modulation’’ beyond ω_{EP} , and it is the reason why the sideband of $\omega_{\text{EP}} \pm \omega_{\text{orb}}$ becomes comparable or even dominates over the main band when $k_0 R_{\oplus} \gg 1$. As shown in Fig. 11, when $k_0 R_{\oplus} \gtrsim 100$, corresponding to $m_\phi \gtrsim 4 \times 10^{-9}$ eV, the first sidebands at $\omega_{\text{EP}} \pm \omega_{\text{orb}}$ are about one order of magnitude larger than the main band. Assuming that the noise power spectrum at the sideband frequencies is not qualitatively different from

that at the main band, including the sidebands can considerably improve the sensitivity. We explore this possibility further in Sec. IV D. Since Eq. (70) gives the time-domain evolution in terms of R_n^X and T_n^X , the same formalism can also be applied to a full time-domain analysis using MICROSCOPE time-series data.

The same mechanism populates the $\hat{\mathbf{Y}}$ projection: the higher multipoles ($L \geq 1$) that grow at large $k_0 R_\oplus$ generate components at the orbital harmonics $n \omega_{\text{orb}}$. The key difference is that for the $\hat{\mathbf{Y}}$ projection, the leading component has zero frequency and therefore corresponds to a DC signal. For completeness, we give the $\hat{\mathbf{Y}}$ projection:

$$\hat{\mathbf{Y}} \cdot \tilde{\mathbf{F}}_{\text{bg}} = T_0^Y + \sum_{n=1}^{\infty} T_n^Y \cos\left(n \Theta_{\text{orb}} + n \frac{\pi}{2}\right). \quad (75)$$

Here T_0^Y denotes the DC component, while T_n^Y with $n \geq 1$ denote the orbital-harmonic coefficients, and

$$\text{Main band in } \hat{\mathbf{Y}} \text{ (DC Component):} \quad T_0^Y = -\sin \alpha \left[\frac{a_1}{r} + \left(-\frac{3}{2} + \frac{15}{4} \cos^2 \alpha \right) \frac{a_3}{r} + \dots \right], \quad (76)$$

$$\text{First sideband in } \hat{\mathbf{Y}} \text{ } (\omega_{\text{orb}}): \quad T_1^Y = -\sin \alpha \cos \alpha \left[3 \frac{a_2}{r} + \left(-\frac{15}{2} + \frac{105}{8} \cos^2 \alpha \right) \frac{a_4}{r} + \dots \right], \quad (77)$$

$$\text{Second sideband in } \hat{\mathbf{Y}} \text{ } (2\omega_{\text{orb}}): \quad T_2^Y = -\sin \alpha \cos^2 \alpha \left[\frac{15}{4} \frac{a_3}{r} + \left(-\frac{105}{8} + \frac{315}{16} \cos^2 \alpha \right) \frac{a_5}{r} + \dots \right], \quad (78)$$

$$\text{Third sideband in } \hat{\mathbf{Y}} \text{ } (3\omega_{\text{orb}}): \quad T_3^Y = -\sin \alpha \cos^3 \alpha \left[\frac{35}{8} \frac{a_4}{r} + \left(-\frac{315}{16} + \frac{3465}{128} \cos^2 \alpha \right) \frac{a_6}{r} + \dots \right]. \quad (79)$$

$T_1^Y, T_2^Y, T_3^Y, \dots$ are the one-sided sideband components, as shown in Fig. 12. Note that the force signal in the $\hat{\mathbf{Y}}$ -axis has more apparent annual modulation, given that there is a universal factor $\sin \alpha$ at the front of all coefficients in Eq. (75).

We emphasize that the frequency-band structure shown in Fig. 11 and Fig. 12 is a distinctive smoking-gun signature. For a force described by a spherically symmetric ansatz [14, 25, 29], or for a Yukawa-type central force [2, 3, 27, 72–78], the force has only a radial component. It therefore produces only the ω_{EP} main-band signal along the $\hat{\mathbf{X}}$ axis, while the $\hat{\mathbf{Y}}$ projection vanishes. Although the relative amplitudes depend on the unknown parameter m_ϕ through $k_0 R_\oplus$, the frequency spacing is fixed by the orbital frequency ω_{orb} . Moreover, such an orbital-sideband structure is resolvable by MICROSCOPE [28, 102–104, 122], or the future Galileo Galilei experiment [98–101]. Specifically, for these satellites, $\omega_{\text{orb}} \sim 1$ mHz is much larger than the Fourier resolution $\Delta\omega = 2\pi/T_{\text{session}} \sim 0.01$ mHz for a several-day session. The annual modulation of α can in principle generate additional yearly sidebands around each component, separated by ω_\odot . However, this annual splitting, $\omega_\odot \sim 1 \text{ yr}^{-1} \sim 10^{-5}$ mHz, is much smaller than both the session-level frequency resolution and the orbital-sideband spacing. We therefore neglect this effect in Fig. 11 and Fig. 12.

C. Revised MICROSCOPE Constraints

In this section, we rederive the MICROSCOPE constraints on quadratically coupled ULDM using the force formalism developed above. The constraints from MICROSCOPE found in 2022 a limit on the Eötvös parameter [104],

$$\eta(\text{Ti, Pt}) = 2 \frac{a_{\text{Ti}, \oplus} - a_{\text{Pt}, \oplus}}{a_{\text{Ti}, \oplus} + a_{\text{Pt}, \oplus}} = [-1.5 \pm 2.3 \text{ (stat)} \pm 1.5 \text{ (syst)}] \times 10^{-15}. \quad (80)$$

This MICROSCOPE constraint currently provides one of the leading sensitivities in space-based EP tests, and has been used to constrain a wide range of models, including long-range forces [126–128], axions [30, 57, 83], DM-nuclear scattering [129, 130], and scalar ULDM [14, 24, 25, 30, 40, 59, 119]. In our analysis, we go beyond the Eötvös parameter

Segment	Spin	Date (Start)	Duration (orbits)	α_{start}	α_{end}	η_{obs} (10^{-15})	σ_{stat} (10^{-15})	σ_{sys} (10^{-15})	σ_{tot} (10^{-15})
210	V3	2017-02-14	50	-34°	-33°	-29.2	13.1	1.8	13.2
212	V3	2017-02-18	60	-33°	-32°	9.5	11.9	1.0	11.9
218	V3	2017-02-28	120	-31°	-28°	6.7	8.1	1.1	8.2
234	V3	2017-03-15	92	-25°	-22°	5.9	8.3	1.0	8.4
236	V3	2017-03-21	120	-22°	-18°	2.6	6.6	1.2	6.7
238	V3	2017-03-29	120	-18°	-13°	5.8	6.4	1.2	6.5
252	V3	2017-04-13	106	-9°	-5°	-14.9	7.3	1.1	7.4
254	V3	2017-04-20	120	-5°	0°	-14.1	7.0	1.5	7.2
256	V3	2017-04-29	120	1°	6°	-5.3	7.4	1.1	7.5
326-1	V3	2017-09-27	66	32°	29°	-16.3	9.6	1.6	9.7
326-2	V3	2017-10-01	34	29°	28°	-10.4	13.5	1.6	13.6
358	V3	2017-10-14	92	21°	17°	15.8	10.9	1.1	11.0
402	V2	2017-12-06	18	-13°	-14°	28.4	43.6	7.3	44.2
404	V3	2017-12-07	120	-14°	-18°	4.7	6.7	1.0	6.8
406	V3	2017-12-16	20	-19°	-19°	5.9	14.9	3.2	15.2
438	V2	2018-01-16	32	-31°	-32°	-23.4	24.6	5.5	25.2
442	V2	2018-01-22	40	-33°	-33°	-1.5	19.1	7.3	20.4
748	V2	2018-09-03	24	45°	44°	-23.4	24.6	7.3	25.6
750	V3	2018-09-05	8	44°	44°	66.9	38.4	7.3	39.1

TABLE II. MICROSCOPE SUEP data for the 19 science segments from Ref. [28] used in this work. The labels V2 and V3 denote the satellite spin modes, with $\omega_{\text{spin},2} = (9/2)\omega_{\text{orb}}$ and $\omega_{\text{spin},3} = (35/2)\omega_{\text{orb}}$, respectively. The orbital period is $T_{\text{orb}} = 5946\text{ s}$ [121, 122]. The angles α_{start} and α_{end} denote the angle between the MICROSCOPE orbital plane and the mean DM momentum direction \mathbf{k}_0 at the beginning and end of each segment, as given by Fig. 10. The per-session estimate of the Eötvös parameter along the $\hat{\mathbf{X}}$ axis, η_{obs} , and its uncertainties, σ_{stat} , σ_{sys} , σ_{tot} , are quoted in units of 10^{-15} .

and use the segment-level MICROSCOPE data [28], presented in Table II, which precisely takes into account of the satellite position and orientation during each segment.

Before presenting our analysis, we first review previous studies of MICROSCOPE constraints on quadratically coupled ULDM. The MICROSCOPE constraint on repulsive quadratically coupled ULDM was first explored in Ref. [14], using the spherically symmetric ansatz and recasting the first MICROSCOPE constraint on the Eötvös parameter [27]. This constraint was later updated in Ref. [25] using the same ansatz and the final MICROSCOPE constraint on the Eötvös parameter [104]. The attractive case was considered in Refs. [40, 59], where only the s -wave component was included when deriving the constraint. Ref. [30] went beyond the s -wave approximation by including the full partial-wave expansion and phase-space integration. However, its MICROSCOPE recast was intended only as a simplified illustration: it showed that the constraint does not vanish in the high- k_0 regime, due to the interplay between descreening and incoherence, which is clarified in this work as the nonzero higher-multipole contributions. However, it avoided the full numerical treatment by considering only the forward and backward directions. Ref. [119] also considered the full partial-wave expansion and phase-space integration. However, it performed an angular average, which is equivalent to retaining only the da_0/dr component, and therefore obtained a conservative constraint. Including higher multipoles with $L \geq 1$ can further strengthen the constraint, since these contributions do not vanish in the high-momentum regime. Moreover, none of the above works included the MICROSCOPE satellite orbital motion, the instrument-frame rotation, or the annual modulation of the angle between the orbital plane and \mathbf{k}_0 , all of which induce distinctive smoking-gun signal features. With these prior developments in mind, we revisit the MICROSCOPE constraint using the toolbox developed in this work, together with previous efforts, especially Refs. [30, 108, 119].

In this work, we use the MICROSCOPE data reported in Ref. [28] which, along with the corresponding $\alpha(t)$ for each segment computed in this work, are summarized in Table II. Importantly, this data is for the main frequency band ω_{EP} . The analysis includes all 19 SUEP (Sensor Unit for the Equivalence Principle test) data segments, which measure the Eötvös parameter $\eta_{\hat{\mathbf{X}}}|\omega_{\text{EP}}$. From Eq. (80) we can compute the Eötvös parameter induced by the background-induced force. Because the constraint in Ref. [28] for each segment is for the main band $\omega = \omega_{\text{EP}}$ projected on the $\hat{\mathbf{X}}$ -axis, we have for the numerator

$$a_{\text{Ti},\oplus} - a_{\text{Pt},\oplus} = |\psi_0|^2 \frac{m_{\text{M,Ti}}^2 \mathcal{V}_{\text{Ti}}}{4M_{\text{Ti}}} R_0^X - |\psi_0|^2 \frac{m_{\text{M,Pt}}^2 \mathcal{V}_{\text{Pt}}}{4M_{\text{Pt}}} R_0^X. \quad (81)$$

Here R_0^X is the signed coefficient of the $\cos \Theta_{\text{EP}}$ term in the decomposition of $\hat{\mathbf{X}} \cdot \tilde{\mathbf{F}}_{\text{bg}}$ in Eq. (70). Eq. (16) gives $m_{\text{M},\mathcal{T}}^2 \mathcal{V}_{\mathcal{T}}/4M_{\mathcal{T}} = \pi \alpha_{\mathcal{T}}^{(2)}/M_{\text{pl}}^2$, where $\mathcal{T} = \text{Ti, Pt}$, and $|\psi_0|^2 = 2\rho_\phi/m_\phi^2$. The denominator of Eq. (80), $a_{\text{Pt},\oplus} + a_{\text{Ti},\oplus} \simeq 2g$, where $g = (1/M_{\text{pl}}^2) M_\oplus/(R_\oplus + h)^2 \simeq 7.9 \text{ m/s}^2$ is the gravitational acceleration at the MICROSCOPE orbit. Therefore, we have

$$\eta_{\hat{\mathbf{X}}}|\omega_{\text{EP}} = -\frac{2\rho_\phi}{m_\phi^2} \frac{\pi (\alpha_{\text{Ti}}^{(2)} - \alpha_{\text{Pt}}^{(2)}) (R_\oplus + h)^2}{M_\oplus R_\oplus} \left[\frac{da_0}{d(r/R_\oplus)} - \left(\frac{1}{2} - \frac{3}{4} \cos^2 \alpha \right) \frac{da_2}{d(r/R_\oplus)} + \dots \right]. \quad (82)$$

In the above equation, $\alpha_{\mathcal{T}}^{(2)}$ is the effective coupling between the scalar and the testmass $\mathcal{T} = \text{Ti, Pt}$, as defined in Eq. (13). Since $\alpha_{\mathcal{T}}^{(2)}$ is a function of $d_i^{(2)}$, we can recast the MICROSCOPE constraint on the $m_\phi - d_i^{(2)}$ plane afterwards. Comparing with the spherically symmetric ansatz in Refs. [14, 25], we have

$$\frac{\eta_{\hat{\mathbf{X}}}|\omega_{\text{EP}}}{\eta_{\text{sph}}} = \frac{1}{\frac{d(\psi_{\text{sph}}^2/|\psi_0|^2)}{d(r/R_\oplus)}} \left[\frac{da_0}{d(r/R_\oplus)} - \left(\frac{1}{2} - \frac{3}{4} \cos^2 \alpha \right) \frac{da_2}{d(r/R_\oplus)} \right], \quad (83)$$

which we show in ten curves uniformly sampled over $0^\circ \lesssim \alpha \lesssim 50^\circ$ in Fig. 13. For $k_0 R_\oplus \ll 1$, where $a_0 \simeq \psi_{\text{sph}}^2/|\psi_0|^2$, the Eötvös parameter from the background-induced force reproduces the result of Refs. [14, 25]. As $k_0 R_\oplus \gtrsim 0.1$, however, the a_0 -derivative departs from the spherically symmetric ansatz, enhancing $\eta_{\hat{\mathbf{X}}}|\omega_{\text{EP}}$ by up to a factor of 30. For $k_0 R_\oplus \gtrsim 10$, the a_2 -derivative dominates, highlighting the importance of performing the full calculation beyond spherical symmetry. For $k_0 R_\oplus \gtrsim 100$, the system enters the optical-limit regime and Eq. (83) becomes approximately constant. In this regime, throughout the range of α covered by the MICROSCOPE science sessions, $|\eta_{\hat{\mathbf{X}}}|\omega_{\text{EP}}| < |\eta_{\text{sph}}|$.

To calculate the bound on $d_i^{(2)}$ from MICROSCOPE, we perform a χ^2 test on the data in Table II. The statistical uncertainty is obtained by MICROSCOPE [28] from their data-analysis framework, and it is also verified that the statistical error in each segment is compatible with the Gaussian distribution. The systematic uncertainty is separately reported by MICROSCOPE by combining the error budgets. Following the common convention, we evaluate the total error σ_{tot} by adding the statistical and systematic errors in quadrature, i.e., $\sigma_{\text{tot}} = \sqrt{\sigma_{\text{stat}}^2 + \sigma_{\text{sys}}^2}$. From now we use $\eta_{\text{obs},I}$ and $\sigma_{\text{tot},I}$ to indicate the observed Eötvös parameter and total error, respectively, for the I -th SUEP segment given in Table II. We treat the MICROSCOPE data in each segment as Gaussian distributed around the theoretical prediction, with the standard deviation given by $\sigma_{\text{tot},I}$. We follow the likelihood analysis method in Ref. [131] and use the χ^2 statistic without nuisance parameters or correlated noise between segments. For the 19 scientific segments and for a certain m_ϕ , the χ^2 statistic with respect to the coupling $d_i^{(2)}$ is,

$$\chi^2(d_i^{(2)}; m_\phi) = \sum_{I=1}^{N_{\text{seg}}} \left[\frac{\eta_{\text{obs},I} - \eta_{\hat{\mathbf{X}}}|\omega_{\text{EP}}(d_i^{(2)}; m_\phi, \alpha_I)}{\sigma_{\text{tot},I}} \right]^2, \quad (84)$$

where $\eta_{\hat{\mathbf{X}}}|\omega_{\text{EP}}(d_i^{(2)}; m_\phi, \alpha_I)$ is the contribution from ULDM ϕ with mass m_ϕ and coupling $d_i^{(2)}$, estimated at the I -th segment with DM wind direction α_I , and $N_{\text{seg}} = 19$ is the number of SUEP scientific segments as given in Table II. We restrict our analysis to scenarios in which only a single coupling $d_i^{(2)}$ is nonzero. Here our χ^2 statistic Eq. (84) is

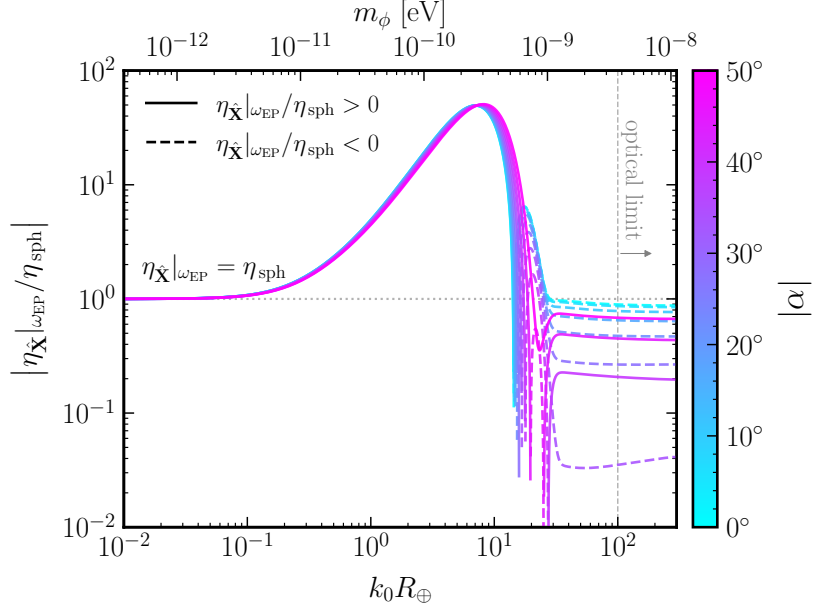


FIG. 13. Ratio between the Eötvös parameter $\eta_{\hat{\mathbf{X}}}|\omega_{\text{EP}}$ along the sensitive axis $\hat{\mathbf{X}}$ in the main ω_{EP} band, defined in Eq. (82), and the corresponding Eötvös parameter obtained in the spherically symmetric ansatz of Refs. [14, 25]. We show ten curves with $|\alpha|$ uniformly sampled from 0° to 50° , with colors varying from cyan to magenta.

equivalent to the log-likelihood for the Gaussian distributed errors

$$L(d_i^{(2)}; m_\phi) = \prod_{I=1}^{N_{\text{seg}}} \frac{1}{\sqrt{2\pi} \sigma_{\text{tot},I}} \exp \left[-\frac{1}{2} \left(\frac{\eta_{\text{obs},I} - \eta_{\hat{\mathbf{X}}}|\omega_{\text{EP}}(d_i^{(2)}; m_\phi, \alpha_I)}{\sigma_{\text{tot},I}} \right)^2 \right]. \quad (85)$$

Therefore $\chi^2 = -2 \log L + \text{const.}$ To generate the upper limit of the coupling $d_i^{(2)}$, we use the test statistic $\Delta\chi^2$ defined as

$$\Delta\chi^2(d_i^{(2)}; m_\phi) = \chi^2(d_i^{(2)}; m_\phi) - \min_{d_i^{(2)}} \chi^2(d_i^{(2)}; m_\phi), \quad (86)$$

where the second term minimizes $\chi^2(d_i^{(2)}; m_\phi)$ in terms of $d_i^{(2)}$ for a fixed m_ϕ . It is equivalent to the log-likelihood ratio of $L(d_i^{(2)}; m_\phi)$ and the maximized likelihood $\max_{d_i^{(2)}} L(d_i^{(2)}; m_\phi)$ as $\Delta\chi^2 = -2 \log(L / \max_{d_i^{(2)}} L)$. Based on Wilks' theorem, $\Delta\chi^2$ follows a χ^2 -distribution with one degree-of-freedom. We set a 95% C.L. one-sided upper limit on $d_i^{(2)}$ by requiring $\Delta\chi^2(d_i^{(2)}; m_\phi) = 2.71$.

Compared with previous studies that assumed a spherically symmetric ansatz, we find notable modifications to the resulting constraints. We find that for $m_\phi \sim 10^{-11}$ eV, the constraint receives an enhancement by over an order of magnitude, but weakens at higher masses, for all values of α considered (see Fig. 13). Both of these effects are consequences of deviating from spherical symmetry. The combined result is shown in Fig. 14. Here, we compare the upper bound on $d_e^{(2)}$ obtained from two χ^2 analyses – one using the previous spherically symmetric ansatz [14, 25], and the other using the EP-band signal $\eta_{\hat{\mathbf{X}}}|\omega_{\text{EP}}$ in Eq. (82) – together with the ratio between the upper bounds. We find similar results for the other couplings, which we show in Fig. 16.

Note that when imposing the MICROSCOPE constraint in this section using χ^2 -analysis, we only consider the main EP band with $\omega = \omega_{\text{EP}}$, i.e., the magenta band in Fig. 11. As we have discussed in the previous section, performing an analysis with the full frequency band structure can further enhance the constraint. We quantify this enhancement in the next section.

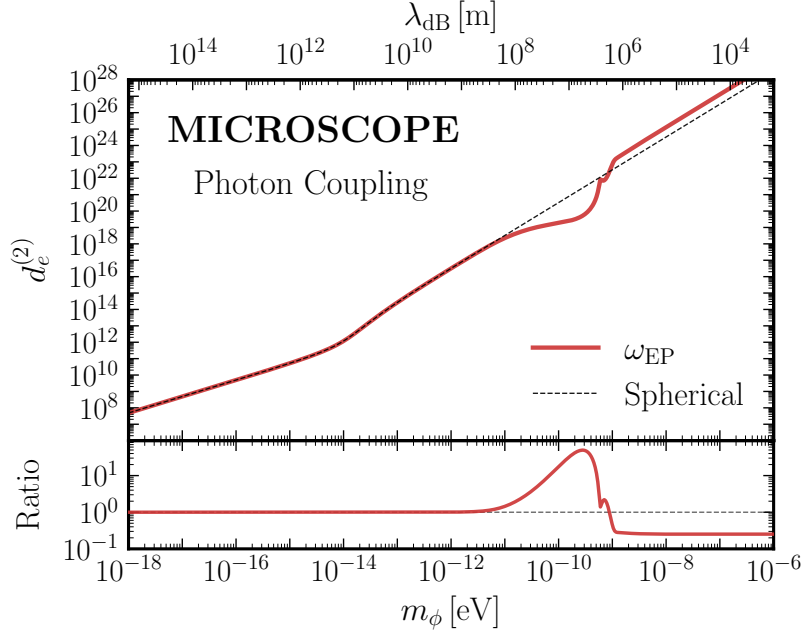


FIG. 14. χ^2 upper-limit on $d_e^{(2)}$ from MICROSCOPE. The **red solid** line is derived from the EP-band signal $\eta_{\hat{\mathbf{X}}|\omega_{\text{EP}}}$ in Eq. (82), while the **black dashed** line is obtained using the previous spherically symmetric ansatz [14, 25]. The lower panel shows the ratio of the limit on $d_e^{(2)}$ obtained using the previous spherically symmetric ansatz to that obtained using the EP-band signal $\eta_{\hat{\mathbf{X}}|\omega_{\text{EP}}}$ in Eq. (82). Note that this ratio does not depend on the specific scalar–SM coupling considered.

D. Future Experimental Probes and Analyses

In the previous section, we derived the MICROSCOPE constraint using our force formalism and the published segment-level measurements in the main ω_{EP} band [28], as given in Table II. The same force formalism also predicts orbital sidebands at $\omega_{\text{EP}} \pm n\omega_{\text{orb}}$. In principle, these sidebands can provide additional sensitivity, because they contain independent coherent components of the same background-induced force signal. A full frequency-band analysis of MICROSCOPE, however, would require the frequency-dependent uncertainties at each sideband, which are not directly available from Ref. [28]. We therefore leave a dedicated full-band MICROSCOPE analysis to future work. In this section, we instead formulate the general $\Delta\chi^2$ including the sideband contributions and illustrate its impact with next-generation EP-tests (see Table III). The benchmark parameters are inspired by the Galileo Galilei proposal [98–101], but the result should be interpreted as a generic next-generation projection.

For the benchmark projection, we consider a rapidly spinning space-based EP test with $\omega_{\text{spin}} \simeq 2\pi \times 1$ Hz, an observing time $T_{\text{obs}} \simeq 1$ day, and an effective Eötvös sensitivity $|\eta_{\text{NG}}| \lesssim 10^{-17}$ representative of a next-generation target. Motivated by the reference geometry of the MICROSCOPE mission [28, 104, 122] and the proposed Galileo Galilei design [98–101], we adopt a configuration where the spin axis is perpendicular to the orbital plane and the force-sensitive plane coincides with the orbital plane. We do not attempt to model the mission-long evolution of the spin–orbit geometry or the associated systematic-errors. With this benchmark geometry, the $\hat{\mathbf{X}}$ -projected force decomposition in Eq. (70) directly gives the multiband Eötvös signal,

$$\begin{aligned} \eta_{\hat{\mathbf{X}}}(t) &= \eta_{\hat{\mathbf{X}}|\omega_{\text{EP}}} \cos \Theta_{\text{EP}} \\ &+ \sum_{n=1}^{\infty} \left[\eta_{\hat{\mathbf{X}}|\omega_{\text{EP}+n\omega_{\text{orb}}}} \cos \left(\Theta_{\text{EP}} + n\Theta_{\text{orb}} + \frac{n\pi}{2} \right) + \eta_{\hat{\mathbf{X}}|\omega_{\text{EP}-n\omega_{\text{orb}}}} \cos \left(\Theta_{\text{EP}} - n\Theta_{\text{orb}} - \frac{n\pi}{2} \right) \right]. \end{aligned} \quad (87)$$

Here, the coefficients of the Eötvös parameter in the frequency domain are given by

$$\eta_{\hat{\mathbf{X}}|\omega_{\text{EP}} \pm n \omega_{\text{orb}}} = \frac{2\rho_{\phi}}{m_{\phi}^2} \frac{\pi (\alpha_{\text{Ti}}^{(2)} - \alpha_{\text{Pt}}^{(2)}) (R_{\oplus} + h)^2}{M_{\oplus} R_{\oplus}} \times (R_n^X \pm T_n^X), \quad (88)$$

where R_n^X and T_n^X are given in Sec. IV B. Note that when $n = 0$, where $T_0^X = 0$, Eq. (88) simplifies to the expression for the main band Eq. (82). We first compute the autocorrelation of Eq. (88) using $C_{\eta}(\tau) = \langle \eta_{\hat{\mathbf{X}}}(t) \eta_{\hat{\mathbf{X}}}(t+\tau) \rangle_t$, and then use the Wiener–Khinchin theorem to obtain the two-sided power spectral density (PSD) $S_{\eta}^{(2)}(f) = \int_{-\infty}^{\infty} d\tau e^{-2i\pi f\tau} C_{\eta}(\tau)$. Since $f \geq 0$, $2S_{\eta}^{(2)} \rightarrow S_{\eta}$ and we have the one-sided PSD

$$S_{\eta}(f) = \underbrace{\frac{1}{2} \left[\eta_{\hat{\mathbf{X}}|\omega_{\text{EP}}} \right]^2 \delta(f - f_{\text{EP}})}_{\text{Main band}} + \underbrace{\sum_{n=1,2,\dots} \frac{1}{2} \left[\eta_{\hat{\mathbf{X}}|\omega_{\text{EP}} \pm n \omega_{\text{orb}}} \right]^2 \delta(f - (f_{\text{EP}} \pm n f_{\text{orb}}))}_{\text{Sidebands}}. \quad (89)$$

The main band and orbital sidebands are spectrally resolved because $f_{\text{orb}} \gg 1/T_{\text{obs}}$. Using a matched-filter statistic for the coherent oscillatory signal induced by the Earth’s background-induced force [132], we have

$$\text{SNR}^2 = 2 N_{\text{sens}} T_{\text{obs}} \int_0^{\infty} df \frac{S_{\eta}(f)}{S_n(f)}, \quad (90)$$

where $S_n(f)$ is the one-sided noise power spectrum. N_{sens} is the number of independent force-sensitive axes: $N_{\text{sens}} = 1$ for MICROSCOPE (sensitive along $\hat{\mathbf{X}}$ only) and $N_{\text{sens}} = 2$ for Galileo Galilei which has a 2D force-sensitive plane [99–101]. Because $\omega_{\text{spin}} \gg \omega_{\text{orb}}$, we approximately have the noise power spectrum $S_n(f_{\text{EP}} \pm n f_{\text{orb}}) \simeq S_n(f_{\text{EP}})$ in the first few sidebands, which gives the dominant contribution to the signal. Therefore, from the previous SNR analysis, we have $\Delta\chi^2 = \text{SNR}^2$, which gives

$$\Delta\chi^2(d_i^{(2)}; m_{\phi}) = \underbrace{N_{\text{sens}} \left[\frac{\eta_{\hat{\mathbf{X}}|\omega_{\text{EP}}}(d_i^{(2)}; m_{\phi}, \alpha)}{\sigma_{\text{tot}}} \right]^2}_{\text{Main band}} + \underbrace{N_{\text{sens}} \sum_{n=1,2,\dots} \left\{ \left[\frac{\eta_{\hat{\mathbf{X}}|\omega_{\text{EP}} + n \omega_{\text{orb}}}(d_i^{(2)}; m_{\phi}, \alpha)}{\sigma_{\text{tot}}} \right]^2 + \left[\frac{\eta_{\hat{\mathbf{X}}|\omega_{\text{EP}} - n \omega_{\text{orb}}}(d_i^{(2)}; m_{\phi}, \alpha)}{\sigma_{\text{tot}}} \right]^2 \right\}}_{\text{Sidebands}}, \quad (91)$$

where $\sigma_{\text{tot}} \simeq \sqrt{S_n(f_{\text{EP}})/T_{\text{obs}}}$ for main band and adjacent sidebands. Compared with Eq. (84), the additional terms in the second line account for the sidebands $\omega_{\text{EP}} \pm n \omega_{\text{orb}}$, where $n = 1, 2, \dots$

To illustrate the impact of the sidebands on the sensitivity, we consider a single observation window at $\alpha = 25^\circ$, which is a typical value of the angle between the orbital plane and \mathbf{k}_0 , as shown in Table II. As before, we take the 95% C.L. one-sided upper limit $\Delta\chi^2 = 2.71$ on $d_i^{(2)}$. We estimate the uncertainty as $\sigma_{\text{tot}} \simeq |\eta_{\text{NG}}|/\sqrt{2.71} \simeq 10^{-17}/\sqrt{2.71}$. In Fig. 15, we show the sensitivity lines for the next-generation EP-tests from considering the only main band at ω_{EP} and from including the sidebands $\omega_{\text{EP}} \pm n \omega_{\text{orb}}$. We find that including the sidebands can improve the sensitivity by more than an order of magnitude relative to the main band for $m_{\phi} \gtrsim 10^{-11}$ eV. This enhancement can be understood from Fig. 11, which shows that the sideband force becomes comparable to, and can even exceed, the main-band force at large $k_0 R_{\oplus}$. Furthermore, we find that the $n = 1$ sideband dominates over the higher orbital sidebands, so including modes with $n > 1$ provides little additional gain in sensitivity.

Note that the ratio shown in Fig. 15 depends only on the geometric parameter α and is independent of $d_i^{(2)}$. While varying α changes the numerical value of the ratio, it modifies the full-band sensitivity by at most an $\mathcal{O}(1)$ factor and does not change the conclusion that including the sidebands improves the sensitivity. This is because, for $k_0 R_{\oplus} \lesssim 10$, the sensitivity is dominated by the α -independent da_0/dr contribution to $\eta_{\hat{\mathbf{X}}|\omega_{\text{EP}}}$. For $k_0 R_{\oplus} \gtrsim 10$, the sensitivity is instead dominated by the first sidebands at $\omega_{\text{EP}} \pm \omega_{\text{orb}}$, whose amplitudes are proportional to $\cos \alpha$ (see Eq. (72)). Since α remains acute throughout the orbit (see Fig. 10), the resulting variation remains an $\mathcal{O}(1)$

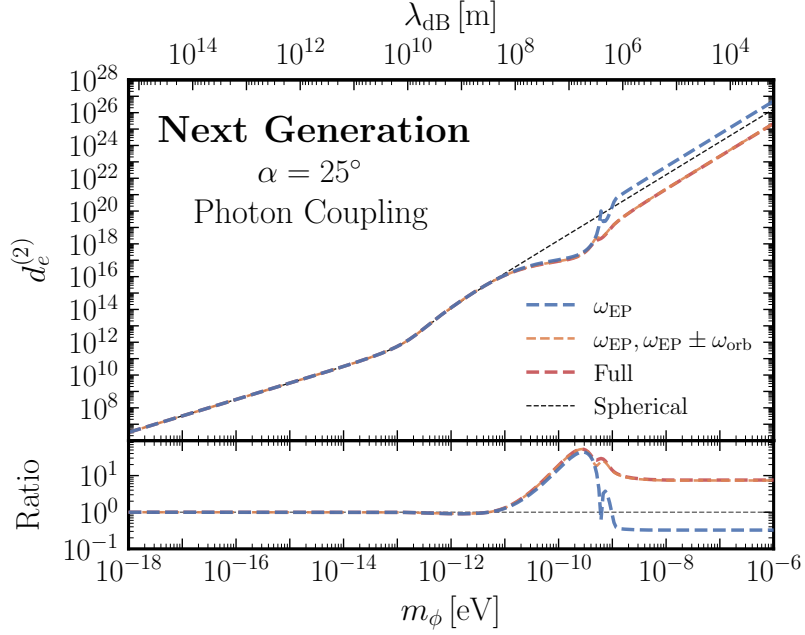


FIG. 15. Next-generation EP test sensitivity to $d_e^{(2)}$ with the benchmark parameters inspired by the Galileo Galilei proposal [98–101]. The **blue dashed** is the EP-band signal $\eta_{\mathbf{X}}|_{\omega_{\text{EP}}}$ in Eq. (82). The **red dashed** and **orange dashed** lines correspond to adding the first sideband $\omega_{\text{EP}} \pm \omega_{\text{orb}}$ and all sidebands, respectively. The **black dashed** line comes from the spherically symmetric ansatz [14, 25]. The lower panel shows the ratio of $d_e^{(2)}$ obtained using the spherically symmetric ansatz over that obtained using the band information listed above. Including the sideband information can strengthen the constraint by roughly one order of magnitude for $m_\phi \gtrsim 10^{-9}$ eV. This ratio is independent of the choice of scalar–SM coupling. Varying α changes the ratio by $\mathcal{O}(1)$ but not the qualitative conclusion.

Category	Experiment	Altitude h [km]	Eötvös η	Status
Satellite	MICROSCOPE [28, 104, 122]	710	$[-1.5 \pm 2.3 \pm 1.5] \times 10^{-15}$	Completed
	CSS [135, 136]	390	$[-3.1 \pm 4.6] \times 10^{-7}$	Completed
	Galileo Galilei [98–101]	600	$(\sim 10^{-17})$	Proposed
	STE-QUEST [137, 138]	1400	$(\sim 10^{-17})$	Proposed
	STEP [139, 140]	550	$(\sim 10^{-18})$	Proposed
	QTEST [141]	400	(5×10^{-16})	Proposed
Sounding Rocket	SR-POEM [142]	≥ 800	$(\leq 10^{-16})$	Proposed
Torsion-Balance	Eöt-Wash [143]	0.07	$[0.3 \pm 1.8] \times 10^{-13}$	Completed

TABLE III. Representative EP-test experiments considered in this work. We list their categories, approximate altitudes, Eötvös sensitivities, and status. Values in parentheses denote projected sensitivities for proposed experiments.

effect. We summarize the MICROSCOPE constraints and next-generation experiment sensitivities for the full suite of dilatonic couplings in Fig. 16. For comparison, the constraints from BBN [33] and black hole superradiance [133, 134] are shown in gray. As shown in Ref. [33], the BBN constraints do not apply to the symmetric quark coupling $d_m^{(2)}$. Therefore, for this coupling, MICROSCOPE provides the strongest existing constraint. More generally, for scalar–SM couplings to which BBN constraints apply, next-generation EP tests such as Galileo Galilei and STE-QUEST can reach sensitivities comparable to, or even stronger than, the BBN constraints.

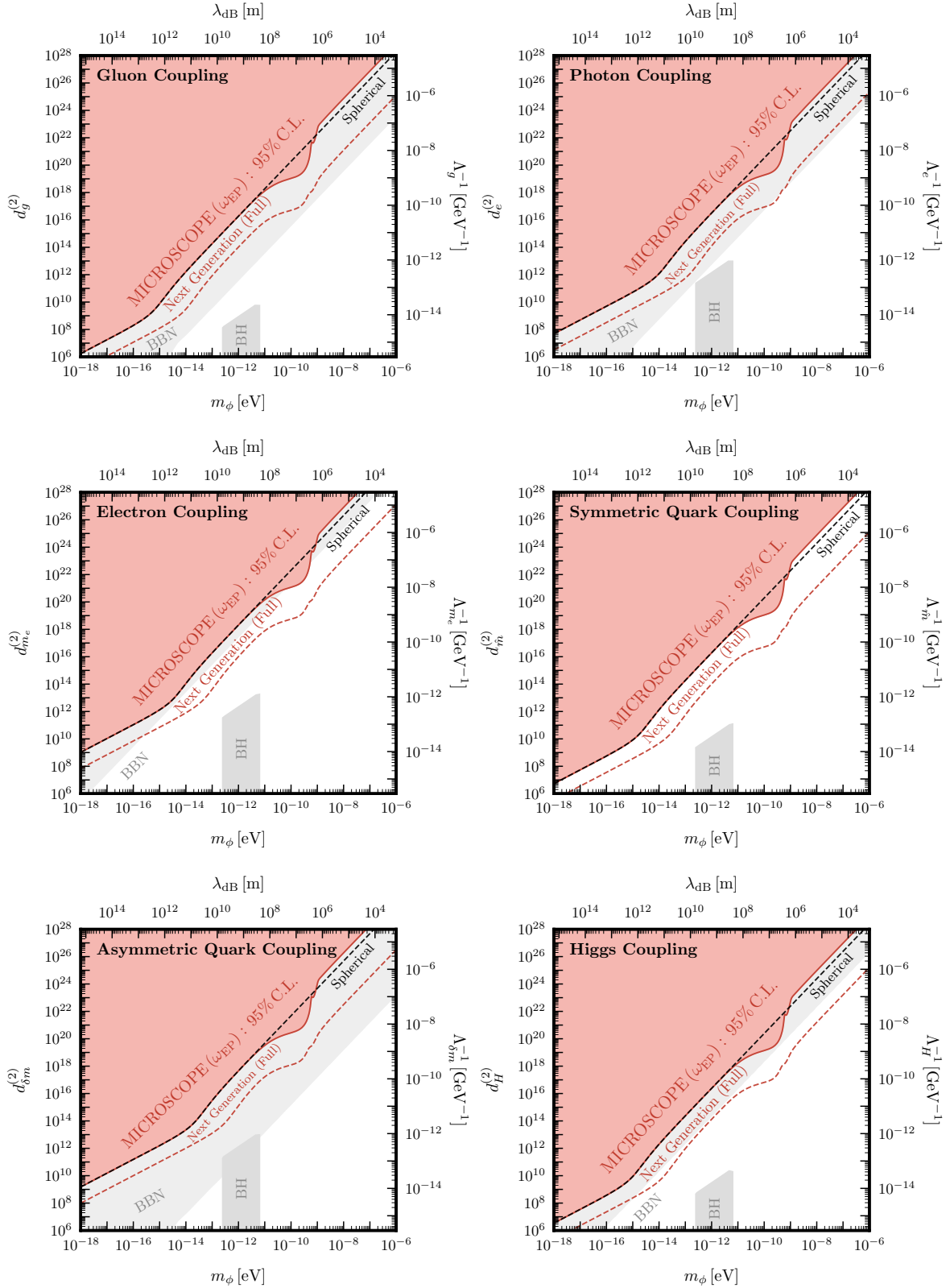


FIG. 16. MICROSCOPE 95% C.L. constraints from the EP-band signal (**red**) and the spherically symmetric ansatz (**black dashed**), and the full-band 95% C.L. projections from a next-generation experiment (**red dashed**) for $d_i^{(2)}$. Also shown in **gray** are the constraints from BBN [33] and black hole superradiance (BH) [133, 134]. Note that the BBN constraints do not apply for the symmetric quark coupling $d_m^{(2)}$.

V. DISCUSSION AND CONCLUSION

Quadratically coupled ultralight scalar dark matter remains a comparatively unexplored dark-matter candidate despite its rich phenomenology and the strong experimental sensitivity of equivalence-principle (EP) tests. A central challenge in interpreting these searches is that the coupling to ordinary matter modifies not only fundamental parameters but also the scalar field configuration itself, giving rise to screening effects and a background-induced force. Accurately predicting observable signals therefore requires a self-consistent treatment of the scalar distribution in the presence of matter.

In this work, we developed a general framework that incorporates phase-space averaging for calculating the background-induced force beyond the spherically symmetric approximation. We showed that the commonly used spherically symmetric ansatz breaks down once the ULDM de Broglie wavelength becomes comparable to the Earth’s radius, $m_\phi \gtrsim 10^{-11}$ eV, and that the resulting modifications can substantially alter the predicted experimental signal. Applying our formalism to the MICROSCOPE mission, we derived updated constraints on the dilatonic couplings that differ significantly from previous results in this regime, by more than an order of magnitude at some masses.

A key result of this work is the identification of a novel frequency-band structure generated by Earth screening. We found that the orbital motion of satellite EP tests lead to characteristic orbital sidebands in the sensitive axis ($\hat{\mathbf{X}}$) signal and generate nonzero signals along the spin axis ($\hat{\mathbf{Y}}$). This results in a signal that exhibits a nontrivial structure in frequency space, suggesting that a full-band analysis could substantially improve experimental sensitivity. Using the proposed Galileo Galilei mission as a benchmark, we find that a full-band analysis improves the reach by more than an order of magnitude, and we expect comparable gains for STE-QUEST. These findings also motivate a dedicated reanalysis of the MICROSCOPE data using the full frequency-band information.

We further demonstrated that the high-mass and strongly coupled regime, corresponding to region (D), admits a simple physical interpretation. In this region, the scalar field approaches the optical-limit configuration and be accurately described using geometric optics. The agreement between the geometric-optics and partial-wave descriptions provides a unified understanding of the scalar distribution across a wide range of parameters.

The methods developed here are readily applicable beyond the scenario considered in this work, including scattering between scalar field and the test mass, as well as attractive scalar interactions, axions, long-range neutrino-mediated forces, and vector models such as $B - L$ gauge bosons. More broadly, our results highlight the importance of matter-induced distortions of ULDM fields and demonstrate that they can generate qualitatively new experimental signatures. The physical insights obtained in this work may help guide the design of future experiments and analyses aimed at probing ULDM and other weakly coupled new physics.

Note Added: While this work was being completed, we became aware of overlapping work in preparation from [144].

ACKNOWLEDGEMENT

We thank Dawid Brzemiński, Yifan Chen, Shao-Feng Ge, Aaron Pierce, G eraldine Servant, Lian-Tao Wang, and Yue Zhao for helpful discussions. The work of X.G. is supported by the Deutsche Forschungsgemeinschaft under Germany’s Excellence Strategy - EXC 2121 “Quantum Universe” - 390833306. H.X. is supported by the Siyuan Postdoctoral (Overseas Talent Recruitment) Program of Shanghai Jiao Tong University and the Shanghai “Super Postdoc” Incentive Program. T-T.Y. is supported by the U.S. Department of Energy under Grant Number DE-SC0011640.

Appendix A: Dilaton Charges

The dimensionless scalar–SM coupling $\alpha_{\mathcal{A}}^{(2)}$, defined as the fractional change in the mass of body \mathcal{A} induced by the background scalar field, governs the interaction between the scalar and SM. Its composition dependence is encoded in the material-dependent dilaton charges $(Q_{\mathcal{A}})_i$, which are determined by hadronic, nuclear, and atomic physics.

Following Refs. [2, 3], we present a pedagogical and self-contained derivation of the scalar and dilaton charges, and give closed-form analytical expressions in terms of the mass and atomic numbers (A, Z), the QCD nucleon matrix elements ($\sigma_{\pi N}, \Delta\sigma$), the electromagnetic nucleon-mass parameters (C_p, C_n), the electron mass m_e , and the nuclear binding-energy parameters entering the semi-empirical mass formula (SEMF). Previous literature [2, 3, 14, 33] has quoted numerical values for these charges. The analytical forms derived here make the composition dependence explicit and are updated with modern hadronic inputs. The dilaton charges for the effective scalar–SM coupling are discussed in Sec. II A and have been widely studied in Refs. [2, 3, 14, 33]. For completeness, we also provide the corresponding expressions for the Higgs portal in Sec. II B and for the universal coupling and light QCD axion in Sec. II C. Although we take the quadratic coupling as the benchmark example throughout this work, the discussion in this section generalizes straightforwardly to scalar–SM couplings with other powers of the scalar field.

1. Scalar–SM Coupling

In this subsection, we derive the scalar–SM coupling $\alpha_{\mathcal{A}}^{(2)}$ and express it in terms of the dilaton charges $(Q_{\mathcal{A}})_i$, which characterize the sensitivity of a test mass to variations of fundamental constants. We first consider a single-component object and discuss the multicomponent generalization at the end of the subsection.

We begin by defining the dimensionless scalar–SM coupling:

$$\frac{\Delta M_{\mathcal{A}}}{M_{\mathcal{A}}} = \frac{\Delta m_{\mathcal{A}}}{m_{\mathcal{A}}} = \alpha_{\mathcal{A}}^{(2)} \times \Phi^{(2)}, \quad \text{where} \quad \Phi^{(2)} = \frac{2\pi\phi^2}{M_{\text{pl}}^2}. \quad (\text{A1})$$

In the above equation, “ \mathcal{A} ” is the subscript labeling the object, and “(2)” indicates a quadratic coupling. Here, $\Phi^{(2)}$ is the dimensionless representation of the quadratic scalar.¹² $M_{\mathcal{A}} = N_{\mathcal{A}} \times m_{\mathcal{A}}$ is the mass of macroscopic object, while $m_{\mathcal{A}}$ is the atomic mass and $N_{\mathcal{A}}$ is the total number of atoms.

The atomic mass receives three contributions that motivate its parametrization:

- *Nucleon masses* – In the combined chiral limit $m_u, m_d \rightarrow 0$ and electromagnetic-decoupling limit $\alpha_{\text{em}} \rightarrow 0$, Λ_{QCD} , generated through dimensional transmutation in the QCD sector, is the only scale determining ordinary hadron masses. This reflects the fact that the dominant chirally symmetric contribution to hadron masses is set by gluodynamics [147, 148]. Once the non-zero chiral-symmetry-breaking parameters $\hat{m}/\Lambda_{\text{QCD}}$ and $\delta m/\Lambda_{\text{QCD}}$, as well as a non-zero α_{em} , are restored, hadron masses (such as the proton and neutron masses) are correspondingly shifted.
- *Nuclear binding energy* – The nuclear binding energy is controlled by Λ_{QCD} , $\hat{m}/\Lambda_{\text{QCD}}$, and α_{em} .
- *Electron mass* – The electron rest mass, which arises from the Higgs mechanism independently of QCD, contributes directly to the atomic mass.

Together, these three contributions, lead to the following parametrization [3]:

$$m_{\mathcal{A}} = \Lambda_{\text{QCD}} \times \bar{m}_{\mathcal{A}} \left(\alpha_{\text{em}}, \frac{m_e}{\Lambda_{\text{QCD}}}, \frac{\hat{m}}{\Lambda_{\text{QCD}}}, \frac{\delta m}{\Lambda_{\text{QCD}}} \right). \quad (\text{A2})$$

Here, Λ_{QCD} is chosen as the reference scale, since it dominates the hadronic contributions to atomic mass. The reduced atomic mass $\bar{m}_{\mathcal{A}}$ is therefore dimensionless and depends only on the dimensionless variables α_{em} , m_e/Λ_{QCD} , $\hat{m}/\Lambda_{\text{QCD}}$, $\delta m/\Lambda_{\text{QCD}}$. We expand on the atomic mass discussion in Sec. A 2.

¹² The discussion in this section extends directly to an \mathcal{N} -th power scalar coupling to the SM sector, defined by $\Phi^{(\mathcal{N})} = (\sqrt{4\pi}\phi/M_{\text{pl}})^{\mathcal{N}}/\mathcal{N}!$, where $\mathcal{N}!$ is the symmetry factor. The corresponding theories are obtained from the effective scalar–SM interaction (Sec. II A), the Higgs portal (Sec. II B), and the universal coupling (Sec. II C) upon the replacement $\Phi^{(2)} \rightarrow \Phi^{(\mathcal{N})}$. However, the interaction of the QCD axion remains quadratic, as ensured by the \mathbb{Z}_2 CP symmetry [30, 55, 145, 146]. The linear case in Ref. [3] is recovered by taking $\Phi^{(1)} = \sqrt{4\pi}\phi/M_{\text{pl}}$. In this work, we focus on the quadratic case, $\Phi^{(2)}$.

Differentiating Eq. (A1) with respect to $\Phi^{(2)}$, we have $\alpha_{\mathcal{A}}^{(2)} = \partial \log m_{\mathcal{A}} / \partial \Phi^{(2)}$. Substituting Eq. (A2) and applying the chain rule, we obtain

$$\alpha_{\mathcal{A}}^{(2)} = (Q_{\mathcal{A}})_g d_g^{(2)} + (Q_{\mathcal{A}})_e d_e^{(2)} + (Q_{\mathcal{A}})_{m_e} (d_{m_e}^{(2)} - d_g^{(2)}) + (Q_{\mathcal{A}})_{\hat{m}} (d_{\hat{m}}^{(2)} - d_g^{(2)}) + (Q_{\mathcal{A}})_{\delta m} (d_{\delta m}^{(2)} - d_g^{(2)}), \quad (\text{A3})$$

where $d_i^{(2)}$ is the dimensionless couplings varying the fundamental constants as given by Eq. (3). Then we have the dilaton charges defined as

$$\begin{aligned} (Q_{\mathcal{A}})_g &= 1, & (Q_{\mathcal{A}})_e &= \frac{\partial \log \bar{m}_{\mathcal{A}}}{\partial \log \alpha_{\text{em}}}, & (Q_{\mathcal{A}})_{m_e} &= \frac{\partial \log \bar{m}_{\mathcal{A}}}{\partial \log (m_e / \Lambda_{\text{QCD}})}, \\ (Q_{\mathcal{A}})_{\hat{m}} &= \frac{\partial \log \bar{m}_{\mathcal{A}}}{\partial \log (\hat{m} / \Lambda_{\text{QCD}})}, & (Q_{\mathcal{A}})_{\delta m} &= \frac{\partial \log \bar{m}_{\mathcal{A}}}{\partial \log (\delta m / \Lambda_{\text{QCD}})}, \end{aligned} \quad (\text{A4})$$

which quantify the sensitivities of the atomic mass to variations in the fundamental constants. Note that $(Q_{\mathcal{A}})_g = \partial \log m_{\mathcal{A}} / \partial \log \Lambda_{\text{QCD}} = 1$, because Λ_{QCD} is chosen as the reference scale for the atomic mass, as given by Eq. (A2).

We now generalize the above discussion to multicomponent objects, such as the Earth or the test masses used in EP experiments. We let I label the different constituents, and write the total mass as $M_{\mathcal{A}} = \sum_I m_{\mathcal{A}_I} N_{\mathcal{A}_I}$. We define $f_{\mathcal{A}_I} = m_{\mathcal{A}_I} N_{\mathcal{A}_I} / M_{\mathcal{A}}$ to be the mass fraction of constituent I , where $m_{\mathcal{A}_I}$ and $N_{\mathcal{A}_I}$ denote the atomic mass and the number of atoms of constituent I , respectively. Since the scalar-SM coupling is defined through the fractional mass variation in Eq. (A1), it follows that $\alpha_{\mathcal{A}}^{(2)}$ is the mass-fraction-weighted average of the constituent couplings. Applying Eq. (A1) and Eq. (A3) to each constituent then yields the corresponding dilaton charges,

$$\alpha_{\mathcal{A}}^{(2)} = \sum_I f_{\mathcal{A}_I} \alpha_{\mathcal{A}_I}^{(2)}, \quad (Q_{\mathcal{A}})_i = \sum_I f_{\mathcal{A}_I} (Q_{\mathcal{A}_I})_i, \quad (\text{A5})$$

with $\sum_I f_{\mathcal{A}_I} = 1$. For a realistic object with multiple constituents, we evaluate its scalar-SM coupling and dilaton charges using Eq. (A5).

2. Atomic Mass

In this section, we introduce the composition of atomic mass in terms of the constituent rest masses and the nuclear binding energy. We briefly explain its origin and then discuss how it depends on variations of the fundamental constants given by Eq. (3).

To start with, we decompose the atomic mass $m_{\mathcal{A}}$ as

$$m_{\mathcal{A}} = (E_{\mathcal{A}})_{\text{rm}} + (E_{\mathcal{A}})_{\text{bind}}, \quad (\text{A6})$$

where $(E_{\mathcal{A}})_{\text{rm}}$ is the rest mass of the nucleons and electrons, and $(E_{\mathcal{A}})_{\text{bind}}$ is the nuclear binding energy. Here, the rest mass is

$$(E_{\mathcal{A}})_{\text{rm}} = Z m_p + N m_n + Z m_e, \quad (N = A - Z) \quad (\text{A7})$$

where m_n is the neutron mass, m_p is the proton mass, m_e is the electron mass. The electron mass arises from the Higgs mechanism, so it is free from the variation of α_{em} , Λ_{QCD} , \hat{m} , δm . The proton and neutron masses are given by

$$m_p = m_{N,0} + \sigma_{\pi N} - \frac{1}{2} \Delta \sigma + C_p, \quad m_n = m_{N,0} + \sigma_{\pi N} + \frac{1}{2} \Delta \sigma + C_n. \quad (\text{A8})$$

In the above equation, $m_{N,0}$ is the nucleon mass in the chiral limit ($m_u, m_d \rightarrow 0$), arising purely from gluon dynamics; $\sigma_{\pi N} = \hat{m} \partial m_{p,n} / \partial \hat{m} = m_{\pi}^2 \partial m_{p,n} / \partial m_{\pi}^2$ is the pion-nucleon sigma term; $\Delta \sigma = -2 \delta m \partial m_p / \partial \delta m = 2 \delta m \partial m_n / \partial \delta m$ quantifies the neutron-proton mass difference arising from isospin violation ($\delta m = m_d - m_u \neq 0$) at electroweak scale; and $C_{p,n} = \alpha_{\text{em}} \partial m_{p,n} / \partial \alpha_{\text{em}}$ is the electromagnetic contribution to the proton and neutron masses. Specifically, we

have

$$m_{N,0} \propto \Lambda_{\text{QCD}}, \quad \sigma_{\pi N} \propto \Lambda_{\text{QCD}} \cdot \left(\frac{\hat{m}}{\Lambda_{\text{QCD}}} \right), \quad \Delta\sigma \propto \Lambda_{\text{QCD}} \cdot \left(\frac{\delta m}{\Lambda_{\text{QCD}}} \right), \quad C_{p,n} \propto \alpha_{\text{em}} \cdot \Lambda_{\text{QCD}}. \quad (\text{A9})$$

The nuclear binding energy is modeled by the Bethe–Weizsäcker semi-empirical mass formula (SEMF) [149–152], given by

$$(E_{\mathcal{A}})_{\text{bind}} = \underbrace{\mathcal{E}_{\text{vol}} A}_{(E_{\mathcal{A}})_{\text{vol}}} + \underbrace{\mathcal{E}_{\text{surf}} A^{2/3}}_{(E_{\mathcal{A}})_{\text{surf}}} + \underbrace{\mathcal{E}_{\text{asym}} \frac{(A-2Z)^2}{A}}_{(E_{\mathcal{A}})_{\text{asym}}} + \underbrace{\mathcal{E}_{\text{em}} \frac{Z(Z-1)}{A^{1/3}}}_{(E_{\mathcal{A}})_{\text{em}}} + \dots. \quad (\text{A10})$$

In the above equation, the subscripts “vol”, “surf”, “asym”, and “em” represent the volume, surface, asymmetry, and Coulomb (electrostatic) energy contributions, respectively. The ellipsis “...” denotes the pairing energy, which is subdominant and therefore neglected. The (Z, A) dependence of each term can be understood through simple physical arguments. The volume term is the binding energy which A nucleus in the bulk contribute, so $(E_{\mathcal{A}})_{\text{vol}} < 0$ and $(E_{\mathcal{A}})_{\text{vol}} \propto A$. The surface term is the correction to the volume term, since the nucleons at the nuclear surface are not attracted by the bulk nucleons, giving $(E_{\mathcal{A}})_{\text{surf}} > 0$ and $(E_{\mathcal{A}})_{\text{surf}} \propto A^{2/3}$. The asymmetric term comes from the asymmetric Pauli exclusion of the number of proton and neutron in the nuclei. When $Z \neq N$, the proton and neutron Fermi surfaces are different, giving the dominant contribution to the energy difference. In addition, ρ -meson exchange generates an extra but subdominant contribution when $Z \neq N$ [153, 154]. Therefore, we have $(E_{\mathcal{A}})_{\text{asym}} > 0$. The factor $[(N-Z)/A]^2$ indicates the lowest order expansion, since the linear expansion in terms of $(N-Z)/A$ vanishes because the nuclear force is invariant under the isospin symmetry $n \leftrightarrow p$ ($N \leftrightarrow Z$). Multiplying the extra bulk extensivity factor A gives $(E_{\mathcal{A}})_{\text{asym}} \propto A \times [(N-Z)/A]^2 \propto (A-2Z)^2/A$. The Coulomb energy term describes the repulsion among protons inside the nucleus. Therefore, we have $(E_{\mathcal{A}})_{\text{em}} > 0$. The numerator $Z(Z-1)$ counts the number of distinct proton pairs, obtained by subtracting the unphysical self-energy of each proton from the naive Z^2 counting. The denominator $A^{1/3}$ reflects the fact that the Coulomb energy is inversely proportional to the nuclear radius $(R_{\mathcal{A}})_{\text{nucleus}} \propto A^{1/3}$.

We now discuss the dependence of each coefficient \mathcal{E} on α_{em} and m_{π} , where the latter follows the Gell-Mann–Oakes–Renner relation $m_{\pi}^2 \propto \hat{m}$ [42, 43]. From Ref. [155], the volume term \mathcal{E}_{vol} and surface term $\mathcal{E}_{\text{surf}}$ both arise from the nuclear central force mediated by pion exchange, and therefore both vary with m_{π}^2 . The asymmetry term $\mathcal{E}_{\text{asym}}$ depends on the Fermi momentum k_F , which is set by the nuclear saturation density n_{sat} [153, 154]. Since the saturation condition is determined by the balance of nuclear forces governed by pion exchange, k_F inherits a dependence on m_{π}^2 [155]. The Coulomb term is given by $(E_{\mathcal{A}})_{\text{em}} = (3/5) \alpha_{\text{em}} Z(Z-1)/(R_{\mathcal{A}})_{\text{nucleus}}$ [149–152], where $(R_{\mathcal{A}})_{\text{nucleus}} = A^{1/3} r_0$. This follows from modeling the nucleus as a uniformly charged liquid drop, with r_0 the empirical nucleon radius. This gives $\mathcal{E}_{\text{em}} = (3/5) \alpha_{\text{em}}/r_0 \propto \alpha_{\text{em}}$. Furthermore, the relation $r_0 k_F = (9\pi/8)^{1/3}$ follows from combining the nuclear saturation density $n_{\text{sat}} = 1/(\frac{4\pi}{3} r_0^3)$ with the degenerate Fermi gas expression $n_{\text{sat}} = \gamma_N \int_{|\mathbf{k}| \leq k_F} \frac{d^3 \mathbf{k}}{(2\pi)^3}$, where $\gamma_N = 2 \times 2$ accounts for the spin of both proton and neutron. Since k_F is governed by m_{π}^2 through the saturation condition, r_0 inherits the same dependence, and consequently \mathcal{E}_{em} acquires an implicit dependence on m_{π}^2 .

3. Dilaton Charge: Analytical Expressions

In this section, we derive the dilaton charge for the coupling scenarios discussed in this work: the effective scalar–SM coupling, the Higgs portal, the universal coupling, and the light QCD axion. The analytical results for the effective scalar–SM coupling are consistent with Ref. [3], but is expressed in a more compact form that makes individual contributions explicit and readily accommodates updated QCD and nuclear inputs. We also define $F_{\mathcal{A}} \equiv A m_{\text{amu}}/m_{\mathcal{A}} \simeq 1$,¹³ where $m_{\text{amu}} \equiv m_{12C}/12 \simeq 931.49$ MeV [156].

¹³ This ratio accounts for the deviation of the atomic mass from the naive estimate $A m_{\text{amu}}$ due to nuclear binding, neutron-proton mass differences, and electron masses with ordering $\mathcal{O}(\text{MeV})$. The deviation from unity is therefore suppressed as $F_{\mathcal{A}} - 1 \sim \mathcal{O}(10^{-3})$, and can be safely set to $F_{\mathcal{A}} \simeq 1$ in the computation of the dilaton charge.

We begin with the effective scalar–SM coupling introduced in Eq. (2) of Sec. II A. Combining Eq. (A6), Eq. (A7), and Eq. (A10), we obtain the atomic mass $m_{\mathcal{A}}$. Substituting $m_{\mathcal{A}}$ into Eq. (A4) and using the scaling relations given in Eq. (A8), we find

$$\begin{aligned}
(Q_{\mathcal{A}})_e &= F_{\mathcal{A}} \frac{1}{m_{\text{amu}}} \left[C_n + (C_p - C_n) \frac{Z}{A} + \mathcal{E}_{\text{em}} \frac{Z(Z-1)}{A^{4/3}} \right], & (\text{Effective Scalar-SM, Sec. II A}), \\
(Q_{\mathcal{A}})_{m_e} &= F_{\mathcal{A}} \frac{m_e}{m_{\text{amu}}} \frac{Z}{A}, \\
(Q_{\mathcal{A}})_{\hat{m}} &= F_{\mathcal{A}} \frac{1}{m_{\text{amu}}} \left[\sigma_{\pi N} + \frac{\partial \mathcal{E}_{\text{vol}}}{\partial \log m_{\pi}^2} + \frac{\partial \mathcal{E}_{\text{surf}}}{\partial \log m_{\pi}^2} \frac{1}{A^{1/3}} + \frac{\partial \mathcal{E}_{\text{asym}}}{\partial \log m_{\pi}^2} \frac{(A-2Z)^2}{A^2} + \frac{\partial \mathcal{E}_{\text{em}}}{\partial \log m_{\pi}^2} \frac{Z(Z-1)}{A^{4/3}} \right], \\
(Q_{\mathcal{A}})_{\delta m} &= F_{\mathcal{A}} \frac{\Delta\sigma}{2m_{\text{amu}}} \frac{A-2Z}{A}.
\end{aligned} \tag{A11}$$

The dilaton charge $(Q_{\mathcal{A}})_e$ for the variation of α_{em} receives two contributions: the electromagnetic self-energies of the proton and neutron (the first two terms), and the Coulomb energy in the nuclear binding energy (the third term). The dilaton charge $(Q_{\mathcal{A}})_{m_e}$ for the electron mass variation is proportional to the electron number fraction Z/A in ordinary matter. This dilaton charge is actually equivalent to doing replacement $\bar{\psi}_e \psi_e \rightarrow \langle \bar{\psi}_e \psi_e \rangle = n_e$ to include the matter effect in the Lagrangian directly. The dilaton charge $(Q_{\mathcal{A}})_{\hat{m}}$ for the symmetric quark mass variation has two main contributions: the pion-mass dependence of the nucleon mass, encoded in the $\sigma_{\pi N}$ term, and the pion-mass dependence of the nuclear binding energy coefficients, encoded in the remaining terms. Finally, the dilaton charge $(Q_{\mathcal{A}})_{\delta m}$ for the asymmetric quark mass variation arises solely from isospin violation ($\delta m = m_d - m_u \neq 0$). Here, nuclear binding contributes no additional term here because the nuclear force maintains isospin symmetry. After acquiring the dilaton charge given by Eq. (A11), one can compute the total effective scalar-SM coupling $\alpha_{\mathcal{A}}^{(2)}$ using Eq. (A3).

Secondly, we discuss the dilaton charge for the Higgs portal of Sec. II B, where the scalar-SM interaction $\alpha_{\mathcal{A}}^{(2)}$ is determined by the single UV parameter $d_H^{(2)}$. Substituting Eq. (8) into Eq. (A3), then we have

$$\alpha_{\mathcal{A}}^{(2)} = (Q_{\mathcal{A}})_H d_H^{(2)}, \quad (Q_{\mathcal{A}})_H = \frac{2}{9} + \frac{\alpha_{\text{em}}}{\pi} (Q_{\mathcal{A}})_e + \frac{7}{9} [(Q_{\mathcal{A}})_{m_e} + (Q_{\mathcal{A}})_{\hat{m}} + (Q_{\mathcal{A}})_{\delta m}] \quad (\text{Higgs Portal, Sec. II B}), \tag{A12}$$

where $(Q_{\mathcal{A}})_H$ is the dilaton charge associated with the Higgs portal. The factor $2/9$ is universal for all materials and therefore cancels in the differential dilaton charge between two test masses in EP tests. However, this factor still contributes to the dilaton charge of the source mass and dominates over the other contributions. We also see that the contribution from $(Q_{\mathcal{A}})_e$ is suppressed by the one-loop factor α_{em}/π arising from the $h\gamma\gamma$ vertex, as discussed in Sec. II B, and can therefore be neglected when computing the dilaton charge.

Thirdly, we discuss the universal coupling of Sec. II C, in which the scalar-SM coupling originates from the ϕ -dependent conformal rescaling of the spacetime metric. In this scenario, the conformal transformation is controlled by a single parameter d_{univ} . Substituting Eq. (10) into Eq. (A3), we obtain

$$\alpha_{\mathcal{A}}^{(2)} = (Q_{\mathcal{A}})_{\text{univ}} d_{\text{univ}}^{(2)}, \quad (Q_{\mathcal{A}})_{\text{univ}} = 1 \quad (\text{Universal Coupling, Sec. II C}). \tag{A13}$$

$(Q_{\mathcal{A}})_{\text{univ}}$ is the dilaton charge for the universal coupling, corresponding to the case in which the effective scalar–SM coupling is identical for all mass terms. Therefore, the equivalence principle is strictly preserved, as illustrated in Refs. [48–52].

Finally, we discuss the charge for the light QCD axion from Sec. II C. Based on the QCD-axion-induced quark field rotation derived in Refs. [54–56], we have

$$\frac{\Delta m_{\pi}^2}{m_{\pi}^2} = \frac{\Delta \hat{m}}{\hat{m}} = \mathcal{F}_{\phi}(\theta_{\phi}) - 1, \quad \frac{\Delta \delta m}{\delta m} = \frac{\mathcal{F}_{\phi}(\theta_{\phi}) - 1}{\mathcal{F}_{\phi}(\theta_{\phi})}, \quad \text{where } \mathcal{F}_{\phi}(\theta_{\phi}) = \sqrt{1 - \beta_{ud} \sin^2 \left(\frac{\theta_{\phi}}{2} \right)}. \tag{A14}$$

In Eq. (A14), $\theta_{\phi} = \phi/f_{\phi}$ is the axion misalignment angle, and $\beta_{ud} = 4m_u m_d / (m_u + m_d)^2 \simeq 0.88$. Substituting $\Delta m_{\pi}^2/m_{\pi}^2$ and $\Delta \delta m/\delta m$ from Eq. (A14) into Eq. (A8) gives the proton and neutron rest masses as functions of θ_{ϕ} .

Similarly, substituting $\Delta m_\pi^2/m_\pi^2$ into Eq. (A10) gives the nuclear binding energy as a function of θ_ϕ . The QCD axion charge and its analytic representation can then be defined in direct analogy with the dilaton case. Defining $(Q_{\mathcal{A}})_{\text{axion}} \equiv \partial \log m_{\mathcal{A}}/\partial(\delta\theta_\phi^2/2)$, where $\delta\theta_\phi \equiv \delta\phi/f_\phi$ is the deviation from the extrema, $\theta_\phi = 0$ (maximum) and $\theta_\phi = \pi$ (minimum), we obtain

$$\begin{aligned} \alpha_{\mathcal{A}}^{(2)}|_{\theta_\phi=0,\pi} &= (Q_{\mathcal{A}})_{\text{axion}}|_{\theta_\phi=0,\pi} \frac{M_{\text{pl}}^2}{4\pi f_\phi^2}, & (\text{Light QCD Axion, Sec. II C}), \\ (Q_{\mathcal{A}})_{\text{axion}}|_{\theta_\phi=0} &= -F_{\mathcal{A}} \frac{\beta_{ud}}{4m_{\text{amnu}}} \left[\left(\sigma_{\pi N} + \Delta\sigma \frac{A-2Z}{2A} \right) \right. \\ &\quad \left. + \left(\frac{\partial \mathcal{E}_{\text{vol}}}{\partial \log m_\pi^2} + \frac{\partial \mathcal{E}_{\text{surf}}}{\partial \log m_\pi^2} \frac{1}{A^{1/3}} + \frac{\partial \mathcal{E}_{\text{asym}}}{\partial \log m_\pi^2} \frac{(A-2Z)^2}{A^2} + \frac{\partial \mathcal{E}_{\text{em}}}{\partial \log m_\pi^2} \frac{Z(Z-1)}{A^{4/3}} \right) \right], & (\text{A15}) \\ (Q_{\mathcal{A}})_{\text{axion}}|_{\theta_\phi=\pi} &= F_{\mathcal{A}} \frac{\beta_{ud}}{4\sqrt{1-\beta_{ud}}m_{\text{amnu}}} \left[\left(\sigma_{\pi N} + \frac{\Delta\sigma}{1-\beta_{ud}} \frac{A-2Z}{2A} \right) \right. \\ &\quad \left. + \left(\frac{\partial \mathcal{E}_{\text{vol}}}{\partial \log m_\pi^2} + \frac{\partial \mathcal{E}_{\text{surf}}}{\partial \log m_\pi^2} \frac{1}{A^{1/3}} + \frac{\partial \mathcal{E}_{\text{asym}}}{\partial \log m_\pi^2} \frac{(A-2Z)^2}{A^2} + \frac{\partial \mathcal{E}_{\text{em}}}{\partial \log m_\pi^2} \frac{Z(Z-1)}{A^{4/3}} \right) \right]. \end{aligned}$$

In the equations listed above, $(Q_{\mathcal{A}})_{\text{axion}}|_{\theta_\phi=0}$ is the axion charge evaluated at $\theta_\phi = 0$. Since this corresponds to the hilltop of the potential, it explains the negative sign of $(Q_{\mathcal{A}})_{\text{axion}}|_{\theta_\phi=0}$. For the $\theta_\phi = 0$ case, we verify that the contribution from the nuclear rest mass is consistent with Ref. [56], and the contribution from the nuclear binding energy is consistent with Refs. [57, 58]. By contrast, $(Q_{\mathcal{A}})_{\text{axion}}|_{\theta_\phi=\pi}$ is the axion charge evaluated at $\theta_\phi = \pi$. Since this corresponds to the potential minimum, $(Q_{\mathcal{A}})_{\text{axion}}|_{\theta_\phi=\pi}$ carries a positive sign. This quantity can be used to characterize the axion effective mass after the axion phase transition has occurred. From Eq. (A15), $\sigma_{\pi N}$, despite being one of the dominant contributions to the absolute matter effect,¹⁴ cancels universally when computing the differential acceleration of two test masses. Therefore, axion-induced EP violation cannot be properly accounted for without the isospin-violating term $\Delta\sigma$ and the nuclear binding energy terms $\mathcal{E}_{\text{surf}}$, $\mathcal{E}_{\text{asym}}$, \mathcal{E}_{em} .

4. Nuclear Physics Inputs

In the previous section, we derived the analytical expressions for the dilaton charges. We now combine these expressions with inputs from nuclear and hadronic physics to obtain their numerical values. Since the numerical formulas most commonly used in the literature were introduced in Refs. [2, 3] in 2010, it is useful to identify which are limited by the underlying model assumptions and which can be updated with modern data.

We start by introducing the dependence of nuclear binding energy on the pion mass. Because the following discussion is built on the point-like contact interactions in the model of Refs. [3, 155], it cannot be further updated within this framework. From Refs. [3, 155], such pion-mass dependence is given by

$$\begin{aligned} \frac{\partial \mathcal{E}_{\text{vol}}}{\partial \log m_\pi^2} &= \frac{\partial \mathcal{E}_{\text{vol}}}{\partial \log G_S} \frac{\partial \log G_S}{\partial \log m_\pi^2}, & \frac{\partial \mathcal{E}_{\text{asym}}}{\partial \log m_\pi^2} &= \mathcal{E}_{\text{asym}}^{(\text{SEMF})} \frac{\partial \log \mathcal{E}_{\text{asym}}}{\partial \log G_S} \frac{\partial \log G_S}{\partial \log m_\pi^2}, \\ \frac{\partial \mathcal{E}_{\text{surf}}}{\partial \log m_\pi^2} &= \frac{\partial \mathcal{E}_{\text{surf}}}{\partial \log G_S} \frac{\partial \log G_S}{\partial \log m_\pi^2}, & \frac{\partial \mathcal{E}_{\text{em}}}{\partial \log m_\pi^2} &= \mathcal{E}_{\text{em}}^{(\text{SEMF})} \frac{\partial \log k_F}{\partial \log G_S} \frac{\partial \log G_S}{\partial \log m_\pi^2}. \end{aligned} \quad (\text{A16})$$

In the above equations, G_S is the coupling strength of the four-fermion contact interaction $\bar{N}N\bar{N}N$ with $N = (p, n)$, parametrizing the scalar channel of the nucleon–nucleon interaction. Because this effective coupling encodes pion-exchange contributions to the nuclear force, G_S depends on the pion mass. The Coulomb energy \mathcal{E}_{em} is proportional to $1/r_0 \propto k_F$, where the Fermi momentum k_F increases as the nuclear interaction G_S strengthens, thereby acquiring an implicit dependence on the pion mass. To evaluate the above pion-mass dependencies, we firstly use the following

¹⁴ The $\sigma_{\pi N}$ term arises from approximating the quadratic axion–SM coupling in the finite-density medium as $a^2\langle\bar{N}N\rangle \simeq a^2 n_N$ [53, 61], where n_N is the nucleon number density.

	$\sigma_{\pi N}$ [MeV]	$C_n - C_p$ [MeV]	$\Delta\sigma$ [MeV]	$m_n - m_p$ [MeV]	C_n [MeV]
DD 2010 [2, 3]	45 [158]	-0.76 [159]	3.10 [3]	2.34 BBN	-0.13 [159]
This Work	$\simeq 60$ [160–162]	-0.87 [45, 163]	2.16 [45, 163]	1.29 [45]	-0.15 (rescaled)

TABLE A.1. Comparison of the main hadronic inputs adopted by Damour and Donoghue [2, 3], denoted DD 2010, with those used in this work. For This Work, we extract $C_n - C_p$ and $\Delta\sigma$ by combining the QCD/QED ratio $(m_n - m_p)_{\text{QCD}}/(m_n - m_p)_{\text{QED}}$ reported by the BMW Collaboration [163] with the experimental value of $m_n - m_p$ [45]. The value of C_n is obtained by rescaling its DD 2010 value while keeping the ratio C_n/C_p fixed. Note that the DD 2010 value of $m_n - m_p$ is inconsistent with the experimental value used in standard BBN, motivating the updated inputs adopted here.

numerical inputs

$$\frac{\partial \mathcal{E}_{\text{vol}}}{\partial \log G_S} \simeq -120 \text{ MeV}, \quad \frac{\partial \mathcal{E}_{\text{surf}}}{\partial \log G_S} \simeq 97 \text{ MeV}, \quad \frac{\partial \log k_F}{\partial \log G_S} \simeq 0.525, \quad \frac{\partial \log G_S}{\partial \log m_\pi^2} \simeq -0.35. \quad (\text{A17})$$

The numerical values in Eq. (A17) can be found in Refs. [3, 155]. To evaluate $\partial \log \mathcal{E}_{\text{asym}}/\partial \log G_S$, we need

$$\mathcal{E}_{\text{asym}} = \frac{k_F^2}{6\sqrt{M_*^2 + k_F^2}} + \frac{G_\rho k_F^3}{12\pi^2}, \quad M_* = m_{N,0} + \frac{\gamma_N G_S k_F^3}{6\pi^2}, \quad G_S \simeq -355.4 \text{ GeV}^{-2}, \quad G_\rho \simeq 15 \text{ GeV}^{-2}, \quad (\text{A18})$$

where M_* is the effective nucleon mass, and $G_\rho = g_\rho^2/m_\rho^2$ denotes the coupling strength in the isovector ρ -meson channel. Here, $g_\rho \simeq 3$ is the corresponding ρNN coupling strength, while $m_\rho \simeq 775 \text{ MeV}$ is the ρ -meson mass [45]. For $\mathcal{E}_{\text{asym}}$ given by Eq. (A18), we take the derivative in terms of G_S using the chain rules, then we have $\partial \log \mathcal{E}_{\text{asym}}/\partial \log G_S \simeq 2.4$, which is consistent with Ref. [3]. Note that the numerical values given in Eq. (A17) and Eq. (A18) depends on the model assuming the nucleon-nucleon contact interaction and nucleon is point-like particle based on the effective theory arised by Serot and Walecka [153, 154]. Therefore, there is currently no generally accepted modern determination that clearly supersedes the Damour and Donoghue (DD 2010) values [2, 3].

To eventually determine the values of Eq. (A16), we also need the following standard textbook values

$$\mathcal{E}_{\text{asym}}^{(\text{SEMF})} \simeq 23 \text{ MeV}, \quad \mathcal{E}_{\text{em}}^{(\text{SEMF})} \simeq 0.72 \text{ MeV}, \quad k_F = 1.3 \text{ fm}^{-1}, \quad k_F r_0 = \left(\frac{9\pi}{8}\right)^{1/3}. \quad (\text{A19})$$

The coefficients $\mathcal{E}_{\text{asym}}^{(\text{SEMF})}$ and $\mathcal{E}_{\text{em}}^{(\text{SEMF})}$ are obtained by fitting the SEMF model to nucleus masses, whose standard textbook values can be found in Refs. [3, 152, 157]. Although modern mass-table fits can shift $\mathcal{E}_{\text{asym}}^{(\text{SEMF})}$ and $\mathcal{E}_{\text{em}}^{(\text{SEMF})}$ mildly, the changes are typically at the $\mathcal{O}(10\%)$ and $\mathcal{O}(1\%)$ level for asymmetric term and Coulomb term, respectively. Moreover, the value of k_F could be updated by the modern nuclear saturation density measurement through $k_F = (3\pi^2 n_{\text{sat}}/2)^{1/3}$, but the change of k_F is typically at the $\mathcal{O}(1\%)$ level. Given the small size of these updates, we use the values quoted in Eq. (A19) directly. Substituting Eq. (A17), Eq. (A19), and previously acquired $\partial \log \mathcal{E}_{\text{asym}}/\partial \log G_S \simeq 2.4$ into Eq. (A16), we have

$$\frac{\partial \mathcal{E}_{\text{vol}}}{\partial \log m_\pi^2} \simeq 42 \text{ MeV}, \quad \frac{\partial \mathcal{E}_{\text{surf}}}{\partial \log m_\pi^2} \simeq -34 \text{ MeV}, \quad \frac{\partial \mathcal{E}_{\text{asym}}}{\partial \log m_\pi^2} \simeq -20 \text{ MeV}, \quad \frac{\partial \mathcal{E}_{\text{em}}}{\partial \log m_\pi^2} \simeq -0.13 \text{ MeV}, \quad (\text{A20})$$

which is consistent with the numerical results given by Ref. [3]. Based on the above discussion, we know that Eq. (A20) encodes the model assumption given by Serot and Walecka [153, 154] and there are no universally accepted modern values, so we continue using these values for the nuclear binding energy derivatives in dilaton charge computation.

Unlike the quantities above, which describe the pion-mass dependence of nuclear binding energies, several hadronic parameters can be updated, as summarized in Table A.1. We firstly use the updated $\sigma_{\pi N} \simeq 60 \text{ MeV}$ [160–162] compared with 45 MeV used in Damour and Donoghue (DD 2010) [2, 3]. For the pion-nucleon sigma term $\sigma_{\pi N}$, two benchmark values, $\sigma_{\pi N} \simeq 40 \text{ MeV}$ and $\sigma_{\pi N} \simeq 60 \text{ MeV}$, are commonly quoted, reflecting a long-standing tension between direct lattice-QCD calculations and dispersive analyses of pion-nucleon scattering data. Recent reanalyses

suggest that this tension could be alleviated once excited-state contamination is properly accounted for, favoring the higher value [160, 161], which we adopt here. For the isospin-breaking parameters $C_n - C_p$ and $\Delta\sigma$, we use the first-principles lattice QCD+QED result $(m_n - m_p)_{\text{QCD}}/(m_n - m_p)_{\text{QED}} = \Delta\sigma/(C_n - C_p) \simeq -2.49$ from the BMW collaboration [163], together with the measured neutron–proton mass difference, $m_n - m_p = 1.29 \text{ MeV}$ [45]¹⁵. By contrast, the original DD 2010 values yield $m_n - m_p \simeq 2.34 \text{ MeV}$ (marked by $\overline{\text{BBN}}$), nearly twice the measured value. Such a large neutron–proton mass splitting would substantially distort the neutron-to-proton freeze-out ratio and the primordial helium abundance, bringing it into conflict with Big Bang Nucleosynthesis constraints [33, 48]. In the absence of a modern update for the individual self-energies C_n and C_p , we rescale C_n keeping the ratio C_n/C_p fixed to its DD 2010 value. This choice has negligible numerical impact, since C_n enters $(Q_{\mathcal{A}})_e$ only as a subdominant contribution and is thus insensitive to variations at the $\mathcal{O}(10\%)$ level. Using the updated numbers given by Table A.1, we have the numerical form of the dilaton charges of the effective scalar-SM couplings:

$$(Q_{\mathcal{A}})_e = \underbrace{-1.6 \times 10^{-4} \left[\frac{C_n}{-0.15 \text{ MeV}} \right]}_{\text{DD 2010: } -1.4 \times 10^{-4}} + \underbrace{9.4 \times 10^{-4} \left[\frac{C_n - C_p}{-0.87 \text{ MeV}} \right] \frac{Z}{A}}_{\text{DD 2010: } 8.2 \times 10^{-4}} + 7.7 \times 10^{-4} \left[\frac{\mathcal{E}_{\text{em}}^{(\text{SEMF})}}{0.72 \text{ MeV}} \right] \frac{Z(Z-1)}{A^{4/3}}, \quad (\text{A21})$$

$$(Q_{\mathcal{A}})_{m_e} = 5.5 \times 10^{-4} \left[\frac{m_e}{0.511 \text{ MeV}} \right] \frac{Z}{A}, \quad (\text{A22})$$

$$(Q_{\mathcal{A}})_{\hat{m}} = \underbrace{0.064 \left[\frac{\sigma_{\pi N}}{60 \text{ MeV}} \right] + 0.045 \left[\frac{\frac{\partial \mathcal{E}_{\text{vol}}}{\partial \log m_{\pi}^2}}{42 \text{ MeV}} \right]}_{\text{DD 2010: } 0.093} - 0.036 \left[\frac{\frac{\partial \mathcal{E}_{\text{surf}}}{\partial \log m_{\pi}^2}}{-34 \text{ MeV}} \right] \frac{1}{A^{1/3}} \\ - 0.02 \left[\frac{\frac{\partial \mathcal{E}_{\text{asym}}}{\partial \log m_{\pi}^2}}{-20 \text{ MeV}} \right] \frac{(A-2Z)^2}{A^2} - 1.4 \times 10^{-4} \left[\frac{\frac{\partial \mathcal{E}_{\text{em}}}{\partial \log m_{\pi}^2}}{-0.13 \text{ MeV}} \right] \frac{Z(Z-1)}{A^{4/3}}, \quad (\text{A23})$$

$$(Q_{\mathcal{A}})_{\delta m} = \underbrace{0.0012 \left[\frac{\Delta\sigma}{2.16 \text{ MeV}} \right]}_{\text{DD 2010: } 0.0017} \frac{A-2Z}{A}. \quad (\text{A24})$$

In Eq. (A21)–Eq. (A24), unlike the purely numerical results presented in DD 2010 [2, 3], we keep the dependence on the underlying particle- and nuclear-physics inputs explicit. This is useful because these hadronic and nuclear inputs carry uncertainties and may be further updated in future work. Using the formulas above, together with the numerical inputs in Eq. (A20) and Table A.1, we can also compute the Higgs-portal dilaton charge defined in Eq. (A12) and the axion charge defined in Eq. (A15). Throughout the rest of this work, we adopt the benchmark values listed in the row labeled “This Work” in Table A.1. The corresponding dilaton charges for the Earth and the MICROSCOPE test masses are presented in Table I. As a consistency check, using the numerical values labeled “DD 2010” in Table A.1, we reproduce the original dilaton charges reported in DD 2010 [2, 3]. For terms whose numerical values differ from those in DD 2010, we indicate the corresponding DD 2010 values with underbrackets for comparison.

Appendix B: Spherically Symmetric Ansatz

In Sec. III B 2, we derived ψ_{sph} by taking the s -wave limit $k_0 R_{\oplus} \ll 1$. In this appendix, we review the spherically symmetric ansatz, as given by Refs. [14, 25, 29], and discuss the screening effect using this analytical formalism.

¹⁵ Alternative determinations of $C_n - C_p$ via the dispersive method [164, 165] differ from our adopted value by at most $\sim 30\%$. While the BMW Collaboration also provides absolute predictions for $(m_n - m_p)_{\text{QED}}$ and $(m_n - m_p)_{\text{QCD}}$ [163], their sum does not match the measured $m_n - m_p$ exactly. We therefore use only the BMW ratio of QCD to QED contributions, anchored by the experimental value of $m_n - m_p$ [45].

Taking the zero-momentum limit $|\mathbf{k}| \rightarrow 0$, we have $E_{\text{eff}}(\mathbf{k}) \rightarrow 0$. Therefore, Eq. (20) can be written as

$$\frac{1}{r^2} \frac{d}{dr} \left(r^2 \frac{d\psi_{\text{sph}}}{dr} \right) = m_{\text{M},\oplus}^2 \theta(R_{\oplus} - r) \psi_{\text{sph}}, \quad (\text{B1})$$

where ψ_{sph} is independent of the angular coordinates. The regular solution satisfying $\psi_{\text{sph}}(r \rightarrow \infty) = |\psi_0|$ is

$$\psi_{\text{sph}}(r) = |\psi_0| \times \begin{cases} 1 - \mathcal{A} \frac{R_{\oplus}}{r} & (r \geq R_{\oplus}) \\ \mathcal{B} \frac{\sinh(m_{\text{M},\oplus} r)}{m_{\text{M},\oplus} r} & (r < R_{\oplus}) \end{cases}, \quad (\text{B2})$$

where $|\psi_0| = \sqrt{2\rho_{\phi}}/m_{\phi}$. Matching ψ_{sph} and $d\psi_{\text{sph}}/dr$ at the surface $r = R_{\oplus}$ determines the coefficients as follows:

$$\mathcal{A} = \frac{m_{\text{M},\oplus} R_{\oplus} - \tanh(m_{\text{M},\oplus} R_{\oplus})}{m_{\text{M},\oplus} R_{\oplus}} = \frac{m_{\text{M},\oplus}^2 \mathcal{V}_{\oplus}}{4\pi R_{\oplus}} J_+(m_{\text{M},\oplus} R_{\oplus}), \quad \mathcal{B} = \frac{1}{\cosh(m_{\text{M},\oplus} R_{\oplus})}. \quad (\text{B3})$$

This reproduces the spherical configuration given by Refs. [14, 25, 29]. To compare with the s -wave approximation given in Eq. (26), Eq. (C12), and Eq. (C13), we have $\mathcal{A} \simeq iA_0/(kR_{\oplus})$ and $\mathcal{B} \simeq B_0$. In the exterior solution, the constant term corresponds to the incident plane wave in the zero-momentum limit, while the term proportional to \mathcal{A} represents the scattered-wave contribution. Substituting ψ_{sph} into Eq. (19), we obtain the full time-dependent scalar configuration, $\phi_{\text{sph}}(t, r) = \psi_{\text{sph}}(r) \cos(m_{\phi} t)$. Therefore, we have $\langle \phi_{\text{sph}}^2 \rangle = \psi_{\text{sph}}^2(r) \langle \cos^2(m_{\phi} t) \rangle = \psi_{\text{sph}}^2(r)/2$. We can compute the background-induced potential using $V_{\text{bg}} = (m_{\text{M},\mathcal{T}}^2 \mathcal{V}_{\mathcal{T}}/4)(\psi_{\text{sph}}^2 - |\psi_0|^2)$ following Eq. (48).

For $m_{\text{M},\oplus} R_{\oplus} \lesssim 1$, the spherically symmetric system lies in the perturbative region (A) of Fig. 1. In this limit, we have the scalar configuration

$$m_{\text{M},\oplus} R_{\oplus} \lesssim 1 : \quad \psi_{\text{sph}}(r) \simeq |\psi_0| \begin{cases} 1 - \frac{m_{\text{M},\oplus}^2 \mathcal{V}_{\oplus}}{4\pi r} & (r \geq R_{\oplus}) \\ 1 - \xi(r) \frac{m_{\text{M},\oplus}^2 \mathcal{V}_{\oplus}}{4\pi R_{\oplus}} & (r < R_{\oplus}) \end{cases}. \quad (\text{B4})$$

This shows that the deviation of ψ_{sph} from its asymptotic value $|\psi_0|$ remains perturbative. The matter-induced effective mass of the Earth, $m_{\text{M},\oplus}^2$, quantifies the coupling strength, while \mathcal{V}_{\oplus} captures the coherent contribution of the entire Earth volume to the scattered wave. Outside the Earth, the scalar perturbation decays as $1/r$. Inside the Earth, the perturbation has an extra $\mathcal{O}(1)$ spatial profile factor encoded in $\xi(r) = 3/2 - (r/R_{\oplus})^2/2$, with $\xi(0) = 3/2$ and $\xi(R_{\oplus}) = 1$. Using the exterior profile $\psi_{\text{sph}}(r > R_{\oplus})$, the background-induced potential and force are

$$m_{\text{M},\oplus} R_{\oplus} \lesssim 1 : \quad V_{\text{bg}} \simeq -\frac{\rho_{\phi}}{m_{\phi}^2} \frac{(m_{\text{M},\mathcal{T}}^2 \mathcal{V}_{\mathcal{T}})(m_{\text{M},\oplus}^2 \mathcal{V}_{\oplus})}{4\pi r}, \quad \mathbf{F}_{\text{bg}} \simeq -\frac{\rho_{\phi}}{m_{\phi}^2} \frac{(m_{\text{M},\mathcal{T}}^2 \mathcal{V}_{\mathcal{T}})(m_{\text{M},\oplus}^2 \mathcal{V}_{\oplus})}{4\pi r^2} \hat{\mathbf{r}}. \quad (\text{B5})$$

Comparing this expression with Eq. (11), we see that it corresponds to the perturbative regime in which the form factor satisfies $\mathcal{F} \simeq 1$. In this regime, the background-induced potential and force are not suppressed by screening, and the full volume of the Earth contributes coherently.

For $m_{\text{M},\oplus} R_{\oplus} \gtrsim 1$, the system enters the non-perturbative screening region (C) of Fig. 1. In this regime, the scalar

configuration becomes

$$m_{\text{M},\oplus} R_{\oplus} \gtrsim 1 : \quad \psi_{\text{sph}}(r) \simeq |\psi_0| \begin{cases} 1 - \frac{R_{\oplus}}{r} + \frac{1}{m_{\text{M},\oplus} r} & (r > R_{\oplus}) \\ \frac{1}{m_{\text{M},\oplus} R_{\oplus}} & (r = R_{\oplus}) \\ \frac{e^{-m_{\text{M},\oplus}(R_{\oplus}-r)}}{m_{\text{M},\oplus} r} & (m_{\text{M},\oplus}^{-1} \lesssim r < R_{\oplus}) \\ 2e^{-m_{\text{M},\oplus} R_{\oplus}} & (r < m_{\text{M},\oplus}^{-1}) \end{cases}. \quad (\text{B6})$$

Away from the Earth's surface where $r > R_{\oplus}$, the scattered-wave contribution is then approximately controlled by the geometric factor R_{\oplus}/r , and becomes insensitive to the microscopic coupling strength $m_{\text{M},\oplus}^2$. At the surface of the Earth, one obtains the factor $1/(m_{\text{M},\oplus} R_{\oplus})$. This shows that the scalar field is suppressed at the surface due to the screening effect induced by the potential barrier from the Earth. Inside the Earth, namely for $m_{\text{M},\oplus}^{-1} \lesssim r < R_{\oplus}$, the scalar field decays exponentially with the penetration depth $m_{\text{M},\oplus}^{-1}$. Using the exterior profile $\psi_{\text{sph}}(r > R_{\oplus})$, we have

$$m_{\text{M},\oplus} R_{\oplus} \gtrsim 1 : \quad V_{\text{bg}} \simeq -\frac{\rho_{\phi}}{m_{\phi}^2} \frac{(m_{\text{M},\oplus}^2 \mathcal{V}_{\mathcal{T}}) R_{\oplus}}{r} \left(1 - \frac{R_{\oplus}}{2r}\right), \quad \mathbf{F}_{\text{bg}} \simeq -\frac{\rho_{\phi}}{m_{\phi}^2} \frac{(m_{\text{M},\oplus}^2 \mathcal{V}_{\mathcal{T}}) R_{\oplus}}{r^2} \left(1 - \frac{R_{\oplus}}{r}\right) \hat{\mathbf{r}}, \quad (\text{B7})$$

which are consistent with the results given in Sec. III B 2. From Eq. (B7), we see that both the background-induced potential and force are independent of $m_{\text{M},\oplus}$. From one perspective, this behavior follows from the fact that, once the system enters the hard-sphere regime, the scalar profile outside the Earth saturates and becomes insensitive to any further increase in the coupling strength. From another equivalent perspective, this can be understood as a manifestation of the screening effect discussed in Sec. III B 1 and Sec. III B 2. To see this explicitly, we can compare Eq. (B5) with Eq. (B7). Relative to the perturbative result in Eq. (B5), the screened potential and force are suppressed by the characteristic factor $3/(m_{\text{M},\oplus} R_{\oplus})^2$, up to the geometric factors shown explicitly in Eq. (B7).

This ansatz assumes that, far from the Earth, the scalar field is a single, homogeneous, zero-momentum mode $|\psi_0|$. In reality the field is part of the virialized Milky Way halo, and since the Solar System moves through it, the field carries a non-zero velocity relative to the Earth and is described by a distribution of momentum modes, e.g., a boosted Maxwell–Boltzmann distribution. For $k_0 R_{\oplus} \ll 1$ this distinction is inconsequential: each mode is effectively homogeneous over the Earth and has the same spherical configuration, so the ansatz remains accurate. Once $k_0 R_{\oplus} \gtrsim 1$, i.e., $m_{\phi} \gtrsim 4 \times 10^{-11}$ eV, it fails on two aspects—for each mode the s -wave approximation breaks down, so higher angular-momentum l -modes must be retained and the scattered profile becomes non-spherical; and different modes are now distributed differently, so the field must be averaged over its momentum distribution. The former calls for a partial-wave treatment and the latter for phase-space averaging over \mathbf{k} . Both are needed to compute the constraint and the distinctive multi-band signal discussed in this work.

Appendix C: Partial Wave Analysis

In this section, we introduce the partial wave analysis that we implement to calculate the field distribution around the scattering object. Unlike the spherically symmetric case discussed in Appendix B, our discussion here applies to both the low-momentum region of $k_0 R_{\oplus} \ll 1$ and the high momentum region of $k_0 R_{\oplus} \gtrsim 1$. We first present the partial wave solution of the field from a monochromatic incident wave, then the multipole expansion of the field amplitude. We then present the phase space integration of the field amplitude and finish this section with results in different limits to compare with previous results [30, 108].

1. Monochromatic Wave Function

A monochromatic incident plane wave with a specified momentum \mathbf{k} can be expanded in spherical coordinates as

$$\psi_{\text{inc}}(\mathbf{r}; \mathbf{k}) = |\psi_0| e^{i\mathbf{k}\cdot\mathbf{r}} = |\psi_0| \sum_{l=0}^{\infty} (2l+1) i^l j_l(kr) P_l(\cos\theta). \quad (\text{C1})$$

When an incident plane wave scatters off a potential barrier, such as that induced by the Earth, the total wavefunction contains both the incident wave and an outgoing scattered component. For a system with azimuthal symmetry, the scattered wave can be written as

$$\psi_{\text{sc}}(\mathbf{r}; \mathbf{k}) = |\psi_0| \sum_{l=0}^{\infty} (2l+1) i^l A_l h_l(kr) P_l(\cos\theta). \quad (\text{C2})$$

As shown in Fig. 4, θ denotes the angle between the position vector \mathbf{r} and the incident momentum \mathbf{k} . $h_l = j_l + iy_l$ are the spherical Hankel functions of the first kind, j_l are the Bessel functions, and y_l are the spherical Neumann functions. A_l is the amplitude of the scattered wave, which can be written as

$$A_l = \frac{S_l - 1}{2} = \frac{e^{2i\delta_l} - 1}{2}. \quad (\text{C3})$$

S_l is the S-matrix of the l -th component of the partial wave, and δ_l is the phase shift. The total wavefunction outside the scatterer is obtained by adding the incident and scattered components,

$$\psi_{\text{out}}(\mathbf{r}; \mathbf{k}) = \psi_{\text{inc}}(\mathbf{r}; \mathbf{k}) + \psi_{\text{sc}}(\mathbf{r}; \mathbf{k}) = |\psi_0| \sum_{l=0}^{\infty} (2l+1) i^l \mathcal{R}_l(kr) P_l(\cos\theta) \quad (r \geq R_{\oplus}). \quad (\text{C4})$$

$\mathcal{R}_l(kr)$ denotes the radial component of each partial wave, as given by

$$\mathcal{R}_l(kr) = j_l(kr) + A_l h_l(kr) \quad (r \geq R_{\oplus}). \quad (\text{C5})$$

Generally speaking, the wave function outside depends on the potential and it needs to be solved numerically. However, if the scattering object is modeled as a uniform sphere, analytical expressions can be obtained for both the interior and exterior wave functions. We start from the Schrödinger equation inside the object

$$-\frac{1}{2m_{\phi}} \nabla^2 \psi_{\text{int}} + V_{\text{eff},\oplus}(\mathbf{r}) \psi_{\text{int}} = E_{\text{eff}}(\mathbf{k}) \psi_{\text{int}}, \quad (\text{C6})$$

where the uniform potential and the effective kinetic energy are defined respectively as

$$V_{\text{eff},\oplus}(\mathbf{r}) = \frac{m_{\text{M},\oplus}^2}{2m_{\phi}} \quad \text{and} \quad E_{\text{eff}}(\mathbf{k}) = \frac{\mathbf{k}^2}{2m_{\phi}}, \quad (\text{C7})$$

which gives

$$(\nabla^2 + k_{\oplus}^2) \psi_{\text{int}} = 0 \quad \text{with} \quad k_{\oplus}^2 = k^2 - m_{\text{M},\oplus}^2. \quad (\text{C8})$$

Considering the convergence at $r = 0$, the solution of the differential equation in a uniform sphere can be expanded in partial waves as

$$\psi_{\text{int}}(\mathbf{r}; \mathbf{k}) = |\psi_0| \sum_{l=0}^{\infty} (2l+1) i^l B_l j_l(k_{\oplus} r) P_l(\cos\theta), \quad (\text{C9})$$

where B_l is the amplitude of the interior wave function. By matching the outside and interior wave function at $r = R_\oplus$, we solve the amplitudes A_l and B_l ,

$$\begin{aligned} A_l &= -\frac{k j_l(k_\oplus R_\oplus) j_{l+1}(k R_\oplus) - k_\oplus j_l(k R_\oplus) j_{l+1}(k_\oplus R_\oplus)}{k j_l(k_\oplus R_\oplus) h_{l+1}(k R_\oplus) - k_\oplus h_l(k R_\oplus) j_{l+1}(k_\oplus R_\oplus)}, \\ B_l &= \frac{k j_l(k R_\oplus) h_{l+1}(k R_\oplus) - k h_l(k R_\oplus) j_{l+1}(k R_\oplus)}{k j_l(k_\oplus R_\oplus) h_{l+1}(k R_\oplus) - k_\oplus h_l(k R_\oplus) j_{l+1}(k_\oplus R_\oplus)}. \end{aligned} \quad (\text{C10})$$

The phase shift is given by

$$\tan \delta_l = \frac{A_l/i}{A_l + 1} = \frac{k j_l(k_\oplus R_\oplus) j_{l+1}(k R_\oplus) - k_\oplus j_l(k R_\oplus) j_{l+1}(k_\oplus R_\oplus)}{k j_l(k_\oplus R_\oplus) y_{l+1}(k R_\oplus) - k_\oplus y_l(k R_\oplus) j_{l+1}(k_\oplus R_\oplus)}. \quad (\text{C11})$$

In the low-momentum limit, $k R_\oplus \ll 1$, the amplitudes of the exterior and interior wavefunctions are dominated by s -wave component ($l = 0$) and can be expanded in powers of $k R_\oplus$. Specifically, the exterior amplitude from the s -wave component is

$$A_0 = -i \frac{m_{M,\oplus} R_\oplus - \tanh(m_{M,\oplus} R_\oplus)}{m_{M,\oplus} R_\oplus} k R_\oplus - \left(\frac{m_{M,\oplus} R_\oplus - \tanh(m_{M,\oplus} R_\oplus)}{m_{M,\oplus} R_\oplus} \right)^2 (k R_\oplus)^2 + \dots, \quad (\text{C12})$$

while the interior amplitude from the s -wave component is

$$B_0 = \frac{1}{\cosh(m_{M,\oplus} R_\oplus)} + \frac{-i}{\cosh(m_{M,\oplus} R_\oplus)} \left(\frac{m_{M,\oplus} R_\oplus - \tanh(m_{M,\oplus} R_\oplus)}{m_{M,\oplus} R_\oplus} \right) (k R_\oplus) + \dots. \quad (\text{C13})$$

Another useful limit is the hard sphere limit, where $m_{M,\oplus} \gg k$ and $m_{M,\oplus} R_\oplus \gg 1$. In this scenario, the field is exponentially suppressed inside the sphere, and the outside wave function is well approximated by the hard-wall boundary condition $\mathcal{R}_l(k R_\oplus) = 0$. Using Eq. (C5), this gives

$$j_l(k R_\oplus) + A_l h_l(k R_\oplus) = 0, \quad A_l = -\frac{j_l(k R_\oplus)}{h_l(k R_\oplus)}, \quad B_l = 0. \quad (\text{C14})$$

Using Eq. (C3), the phase shift in this limit satisfies

$$\tan \delta_l = \frac{j_l(k R_\oplus)}{y_l(k R_\oplus)}. \quad (\text{C15})$$

The hard-sphere expressions for A_l and B_l in Eq. (C14), together with the phase shift δ_l in Eq. (C15), can be recovered by taking the limit $m_{M,\oplus} R_\oplus \gg 1$ in Eq. (C10) and using $j_l(k_\oplus R_\oplus) \simeq i^l e^{m_{M,\oplus} R_\oplus} / 2m_{M,\oplus} R_\oplus$.

2. Phase Space Integration

With the general expression Eq. (C4) of the outside field, we calculate the square of the monochromatic field and integrate it with respect to the Standard Halo Model (SHM). We begin by simplifying the squared of a monochromatic wavefunction with fixed incident momentum \mathbf{k} . Specifically, we have

$$|\psi(\mathbf{r}; \mathbf{k})|^2 = |\psi_0|^2 \sum_{l=0}^{\infty} \sum_{l'=0}^{\infty} (2l+1)(2l'+1) i^{l-l'} \mathcal{R}_l(kr) \mathcal{R}_{l'}^*(kr) P_l(\cos \theta) P_{l'}(\cos \theta). \quad (\text{C16})$$

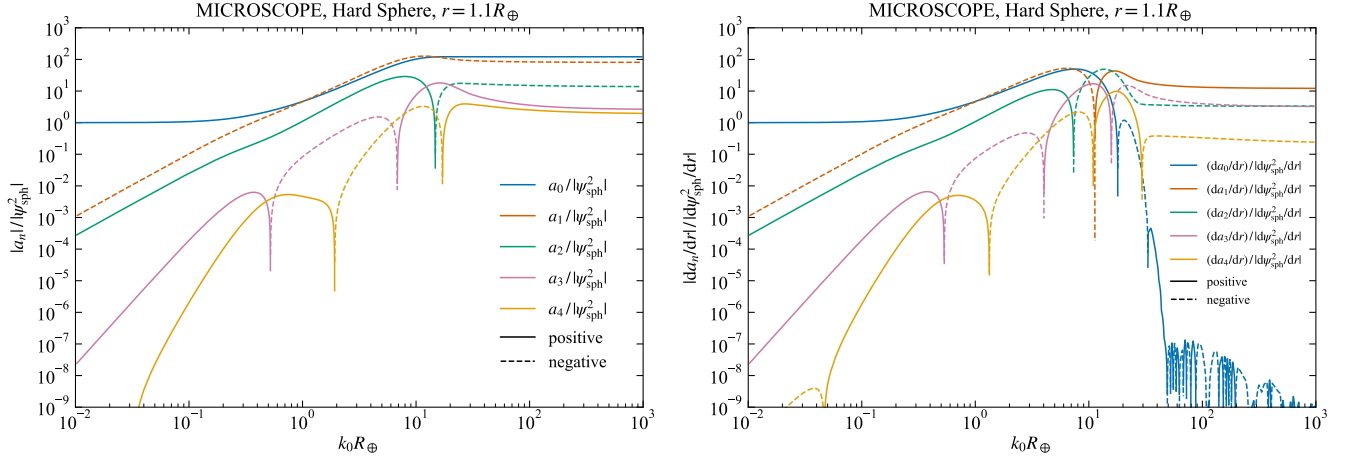


FIG. C.1. The a_L -series and derivatives, same as Fig. 5 and Fig. 6 but in log-scales after taking absolute values, where the solid (dashed) lines are for positive (negative) values. We use the $k_{\text{esc}} \rightarrow \infty$ limit as the difference between using a finite k_{esc} versus an infinite cutoff does not affect our results. Note that da_0/dr is strongly suppressed when $k_0 R_{\oplus} \gg 10$, while other da_L/dr with $L \geq 1$ tends to a constant. This behavior can be understood from the optical limit, where a_0 approaches a constant and therefore da_0/dr vanishes, as shown in Appendix D.

Using the Clebsch–Gordan decomposition of spherical harmonics, the product of two Legendre polynomials can be expanded as a linear combination of Legendre polynomials:

$$P_l(\cos \theta) P_{l'}(\cos \theta) = \sum_{L=|l-l'|}^{l+l'} \underbrace{\langle l 0 l' 0 | L 0 \rangle^2}_{\mathcal{C}_{l'l'L}} P_L(\cos \theta). \quad (\text{C17})$$

Here the coefficients $\mathcal{C}_{l'l'L}$ are determined by the Clebsch–Gordan coefficients and are nonzero only when the selection rules

$$|l - l'| \leq L \leq l + l', \quad l + l' + L \text{ even}. \quad (\text{C18})$$

are satisfied. From Ref. [166], these coefficients are given explicitly by

$$\mathcal{C}_{l'l'L} = \underbrace{\frac{1 + (-1)^J}{2}}_{\text{Zero for odd } J} \times (2L + 1) \frac{(J - 2l)!(J - 2l')!(J - 2L)!}{(J + 1)!} \left[\frac{(\frac{J}{2})!}{(\frac{J}{2} - l)!(\frac{J}{2} - l')!(\frac{J}{2} - L)!} \right]^2, \quad (\text{C19})$$

where $J = l + l' + L$. Another useful equivalent expression of $\mathcal{C}_{l'l'L}$ to simplify the numerical calculation and analytical derivation is

$$\mathcal{C}_{l,l+L-2p,L} = K_{L,p} \times \frac{1}{2(l-p)+1} \times \prod_{i=1}^L \frac{2(l-p+i)}{2(l-p+i)+1}. \quad (\text{C20})$$

Note that Eq. (C20) also makes explicit which coefficients $\mathcal{C}_{l'l'L}$ in Eq. (C19) are nonzero. All remaining coefficients vanish by the Clebsch–Gordan selection rules. Here, $K_{L,p}$ is defined as

$$K_{L,p} \equiv \frac{2L+1}{2^L} \varepsilon_p \varepsilon_{L-p}, \quad \text{where} \quad \varepsilon_p \equiv \frac{(2p)!}{2^p (p!)^2} = \frac{\binom{2p}{p}}{2^p}. \quad (\text{C21})$$

Using the Legendre-product decomposition in Eq. (C17), Eq. (C16) becomes

$$|\psi(\mathbf{r}; \mathbf{k})|^2 = |\psi_0|^2 \sum_{l=0}^{\infty} \sum_{l'=0}^{\infty} (2l+1)(2l'+1) i^{l-l'} \mathcal{R}_l(kr) \mathcal{R}_{l'}^*(kr) \sum_{L=|l-l'|}^{l+l'} \mathcal{C}_{l l' L} P_L(\cos \theta). \quad (\text{C22})$$

We can see that $|\psi(\mathbf{r}; \mathbf{k})|^2$ can be written in terms of linear expansion of the Legendre polynomials,

$$|\psi(\mathbf{r}; \mathbf{k})|^2 = |\psi_0|^2 \sum_{L=0}^{\infty} c_L(r; k, m_{\mathbf{M}, \oplus}) P_L(\cos \theta), \quad (\text{C23})$$

where the coefficient c_L is given by

$$c_L(r; k, m_{\mathbf{M}, \oplus}) \equiv \sum_{l=0}^{\infty} \sum_{l'=0}^{\infty} (2l+1)(2l'+1) i^{l-l'} \mathcal{R}_l(kr) \mathcal{R}_{l'}^*(kr) \mathcal{C}_{l l' L}. \quad (\text{C24})$$

Starting from Eq. (C24), we keep

$$0 \leq p \leq \left\lfloor \frac{L}{2} \right\rfloor \quad (\text{C25})$$

based on the Clebsch–Gordan selection rules in Eq. (C18), and then symmetrize the summand under the interchange $l \leftrightarrow l'$ through the two assignments

$$\begin{cases} l \rightarrow l \\ l' \rightarrow l + L - 2p \end{cases} \quad \text{and} \quad \begin{cases} l \rightarrow l + L - 2p \\ l' \rightarrow l \end{cases}, \quad (\text{C26})$$

we finally get the following general representation:

$$c_L(r; k, m_{\mathbf{M}, \oplus}) = \sum_{l=0}^{\infty} \sum_{p=0}^{\lfloor L/2 \rfloor} [2l+1][2(l+L-2p)+1] \mathcal{C}_{l, (l+L-2p), L} (2 - \delta_{L-2p,0}) \cdot \text{Re} [i^{L-2p} \mathcal{R}_{l+L-2p} \mathcal{R}_l^*], \quad (\text{C27})$$

which enables efficient numerical computation to arbitrary orders in L . Here, the factor $\delta_{L-2p,0}$ prevents double counting of the diagonal terms. As examples, we list the explicit expressions for c_L in Eq. (C27) for $L = 0, \dots, 3$:

$$\begin{aligned} c_0(r; k, m_{\mathbf{M}, \oplus}) &= \sum_{l=0}^{\infty} (2l+1) |\mathcal{R}_l|^2, \\ c_1(r; k, m_{\mathbf{M}, \oplus}) &= -6 \sum_{l=0}^{\infty} (l+1) \text{Im}(\mathcal{R}_{l+1} \mathcal{R}_l^*), \\ c_2(r; k, m_{\mathbf{M}, \oplus}) &= \sum_{l=0}^{\infty} \frac{5(2l+1)l(l+1)}{(2l+3)(2l-1)} |\mathcal{R}_l|^2 - \sum_{l=0}^{\infty} \frac{15(l+2)(l+1)}{2l+3} \text{Re}[\mathcal{R}_{l+2} \mathcal{R}_l^*], \\ c_3(r; k, m_{\mathbf{M}, \oplus}) &= - \sum_{l=0}^{+\infty} \frac{21(l+2)(l+1)l}{(2l+5)(2l-1)} \text{Im}[\mathcal{R}_{l+1} \mathcal{R}_l^*] + \sum_{l=0}^{+\infty} \frac{35(l+3)(l+2)(l+1)}{(2l+5)(2l+3)} \text{Im}[\mathcal{R}_{l+3} \mathcal{R}_l^*], \dots \end{aligned} \quad (\text{C28})$$

We note that the results above focus on simplifying the squared amplitude of a monochromatic wavefunction with a single incident momentum mode \mathbf{k} . To obtain the ensemble-averaged scalar profile $\langle |\psi|^2 \rangle$, and hence the background-induced potential V_{bg} , we must integrate over the DM phase-space distribution given in Eq. (40). As we will see below,

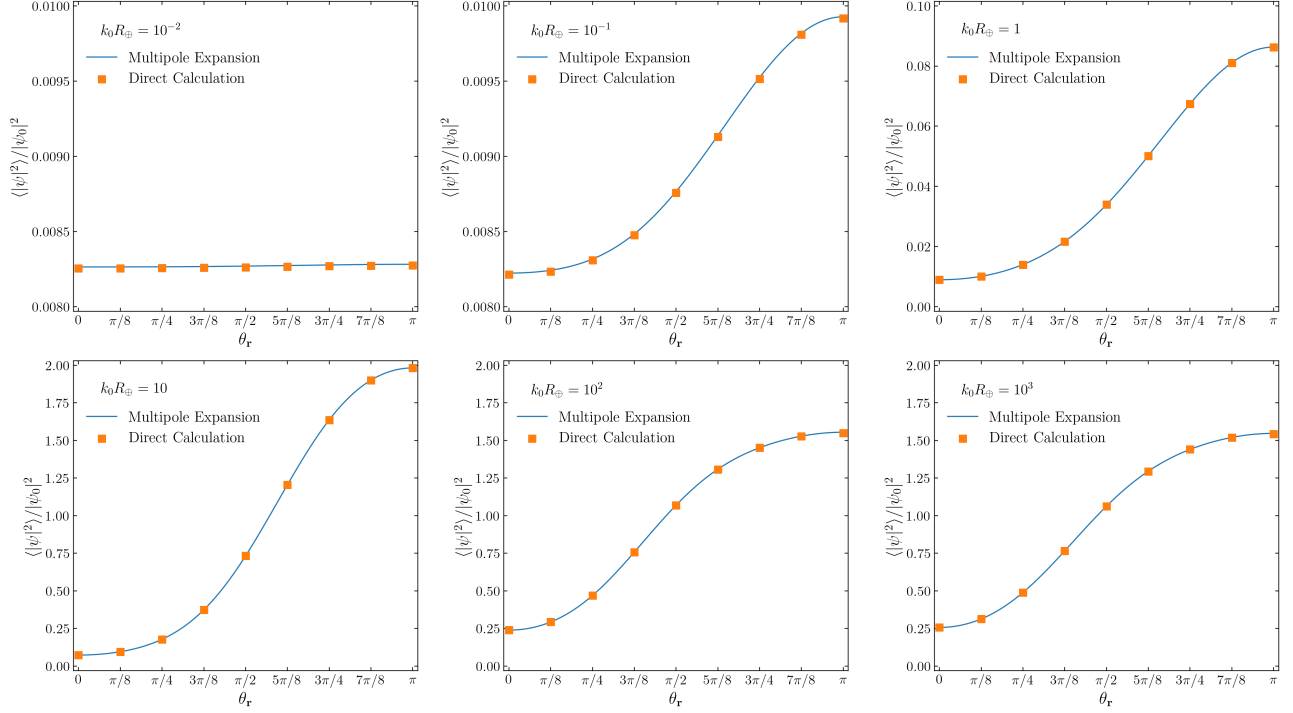


FIG. C.2. The comparison of the $\langle |\psi|^2 \rangle$ calculation between multipole expansion (blue curve) and direct calculation (orange squares).

this averaging procedure, in particular the integration over the azimuthal angle $\phi_{\mathbf{k}}$, provides the second simplification step toward the final computational method. To prepare for the phase-space averaging, we recall from Eq. (40) that the DM distribution in the Solar System is described by the SHM, a truncated Maxwell–Boltzmann distribution, which is

$$f_{\phi}(\mathbf{k}) = \frac{n_{\phi}}{\mathcal{N}(k_{\text{esc}})} \cdot \left(\frac{2\pi}{\sigma_k^2} \right)^{3/2} \exp \left[-\frac{(\mathbf{k} - \mathbf{k}_0)^2}{2\sigma_k^2} \right] \Theta(k_{\text{esc}} - |\mathbf{k} - \mathbf{k}_0|). \quad (\text{C29})$$

For convenience, we follow Fig. 4 and define the spherical coordinate system with \mathbf{k}_0 as the z -axis. Then we have

$$\hat{\mathbf{k}} = (\sin \theta_{\mathbf{k}} \cos \phi_{\mathbf{k}}, \sin \theta_{\mathbf{k}} \sin \phi_{\mathbf{k}}, \cos \theta_{\mathbf{k}}), \quad \hat{\mathbf{r}} = (\sin \theta_{\mathbf{r}}, 0, \cos \theta_{\mathbf{r}}). \quad (\text{C30})$$

The angle between $\hat{\mathbf{k}}$ and $\hat{\mathbf{r}}$ is then given by

$$\cos \theta = \hat{\mathbf{k}} \cdot \hat{\mathbf{r}} = \sin \theta_{\mathbf{k}} \cos \phi_{\mathbf{k}} \sin \theta_{\mathbf{r}} + \cos \theta_{\mathbf{k}} \cos \theta_{\mathbf{r}}. \quad (\text{C31})$$

To find the expectation value of $|\psi|^2$, we integrate Eq. (C23) over $f_{\phi}(\mathbf{k})$,

$$\begin{aligned} \langle |\psi|^2 \rangle &= |\psi_0|^2 \sum_{L=0}^{\infty} \frac{1}{n_{\phi}} \int d^3 \mathbf{k} f_{\phi}(\mathbf{k}) c_L(r; k, m_{M,\oplus}) P_L(\cos \theta) \\ &= |\psi_0|^2 \frac{1}{\mathcal{N}(k_{\text{esc}})} \left(\frac{1}{2\pi\sigma_k^2} \right)^{3/2} \sum_{L=0}^{\infty} \int_0^{+\infty} dk k^2 \exp \left[-\frac{k^2 + k_0^2}{2\sigma_k^2} \right] c_L(r; k, m_{M,\oplus}) \\ &\quad \times \int_{-1}^{+1} d \cos \theta_{\mathbf{k}} \exp \left[\frac{k k_0 \cos \theta_{\mathbf{k}}}{\sigma_k^2} \right] \Theta(k_{\text{esc}} - |\mathbf{k} - \mathbf{k}_0|) \times \underbrace{\int_0^{2\pi} d\phi_{\mathbf{k}} P_L(\cos \theta)}_{\hat{\mathbf{k}}\text{-}\hat{\mathbf{r}} \text{ separation}}, \end{aligned} \quad (\text{C32})$$

Another important step comes from the simplification of the integration $\int_0^{2\pi} d\phi_{\mathbf{k}} P_L(\cos\theta)$. Using the Legendre addition theorem, we have

$$P_L(\underbrace{\cos\theta}_{\hat{\mathbf{k}} \cdot \hat{\mathbf{r}}}) = \frac{4\pi}{2L+1} \sum_{M=-L}^L Y_{LM}(\hat{\mathbf{r}}) Y_{LM}^*(\hat{\mathbf{k}}), \quad (\text{C33})$$

Because

$$\int_0^{2\pi} d\phi_{\mathbf{k}} Y_{LM}^*(\hat{\mathbf{k}}) = \sqrt{\frac{2L+1}{4\pi}} P_L(\cos\theta_{\mathbf{k}}) \times 2\pi\delta_{M0}, \quad (\text{C34})$$

we have

$$\hat{\mathbf{k}}\text{-}\hat{\mathbf{r}} \text{ separation : } \int_0^{2\pi} d\phi_{\mathbf{k}} P_L(\cos\theta) = 2\pi P_L(\cos\theta_{\mathbf{k}}) P_L(\cos\theta_{\mathbf{r}}). \quad (\text{C35})$$

After applying Eq. (C35) to Eq. (C32) and factoring out $P_L(\cos\theta_{\mathbf{r}})$, we obtain

$$\langle |\psi|^2 \rangle = |\psi_0|^2 \sum_{L=0}^{+\infty} a_L(r; k_0, m_{M,\oplus}) P_L(\cos\theta_{\mathbf{r}}). \quad (\text{C36})$$

Here a_L is the multipole coefficient used throughout this work, given by

$$\begin{aligned} a_L(r; k_0, m_{M,\oplus}) &= \frac{1}{\mathcal{N}(k_{\text{esc}})} \left(\frac{1}{2\pi\sigma_k^2} \right)^{3/2} \int_0^{+\infty} dk k^2 \exp\left[-\frac{k^2 + k_0^2}{2\sigma_k^2}\right] c_L(r; k, m_{M,\oplus}) \\ &\times 2\pi \int_{-1}^{+1} d\cos\theta_{\mathbf{k}} \exp\left[\frac{kk_0 \cos\theta_{\mathbf{k}}}{\sigma_k^2}\right] P_L(\cos\theta_{\mathbf{k}}) \Theta(k_{\text{esc}} - |\mathbf{k} - \mathbf{k}_0|). \end{aligned} \quad (\text{C37})$$

In the limit where $k_{\text{esc}} \gg \sigma_k$, using

$$\int_0^{\pi} d\theta_{\mathbf{k}} \sin\theta_{\mathbf{k}} \exp\left[\frac{kk_0 \cos\theta_{\mathbf{k}}}{\sigma_k^2}\right] P_L(\cos\theta_{\mathbf{k}}) = 2i_L\left(\frac{kk_0}{\sigma_k^2}\right), \quad (\text{C38})$$

where $i_L(x) = \sqrt{\frac{\pi}{2x}} I_{L+\frac{1}{2}}(x)$ is the spherical modified Bessel function of the first kind, we have

$$k_{\text{esc}} \gg k_0 : \quad a_L(r; k_0, m_{M,\oplus}) = \left(\frac{1}{2\pi\sigma_k^2} \right)^{3/2} 4\pi \int_0^{\infty} dk k^2 \exp\left[-\frac{k^2 + k_0^2}{2\sigma_k^2}\right] c_L(r; k, m_{M,\oplus}) i_L\left(\frac{kk_0}{\sigma_k^2}\right), \quad (\text{C39})$$

which is consistent with Eq. (44) in the main text. We now summarize our numerical procedure. First, we use Eq. (C27) to generate the analytical representation of c_L up to the required multipole order.¹⁶ Second, for each c_L , we perform the partial-wave summation over l . Here \mathcal{R}_l contains both the incident plane-wave contribution ψ_{inc} and the scattered-wave contribution ψ_{sc} . The convergence condition for the scattered wave is $l_{\text{max}} \sim kR_{\oplus}$, whereas that for the incident plane wave is $l_{\text{max}} \sim kr$. This requires careful numerical treatment: the summation must be taken sufficiently far to capture the incident plane-wave contribution, while avoiding numerical instabilities at excessively large l . Third, after obtaining c_L for a fixed \mathbf{k} through the l -summation, we perform the phase-space averaging using either Eq. (C37) or Eq. (C39), depending on whether the velocity cutoff is included. Finally, once a_L is obtained, the ensemble-averaged scalar profile $\langle |\psi|^2 \rangle$ and the corresponding background-induced potential V_{bg} can be constructed. To compute the background-induced force \mathbf{F}_{bg} , one also needs the radial derivatives da_L/dr , as shown in Eq. (56). Although these derivatives can equivalently be obtained by taking numerical finite differences of V_{bg} or a_L , the most

¹⁶ For the MICROSCOPE analysis in this work, $L_{\text{max}} = 5$ is sufficient. A larger L_{max} is needed to compute V_{bg} at large r/R_{\oplus} , although we have verified that $L_{\text{max}} = 8$ is sufficient for most realistic cases.

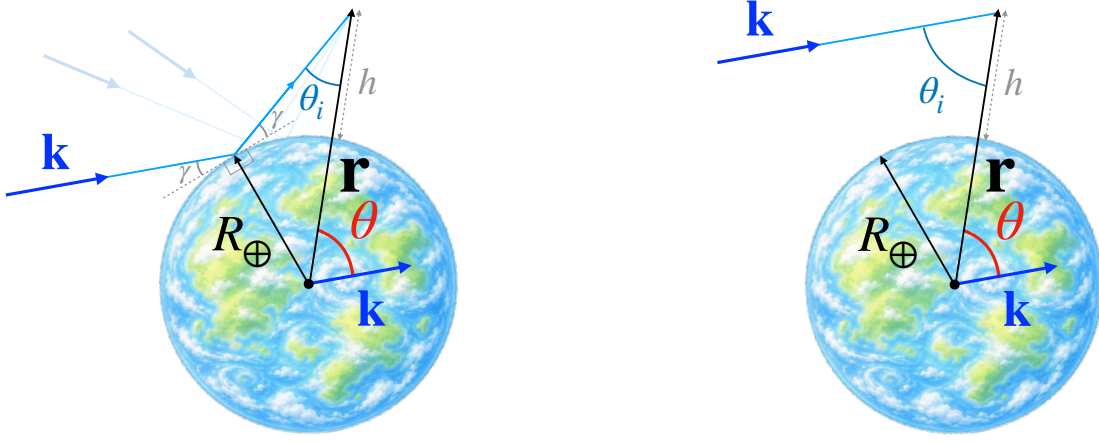


FIG. D.1. Ray geometry for the optical-limit calculation. **Left.** Contribution from the incident ray that reaches the observation point after specular reflection by the Earth. Applying the law of sines to the triangle formed by the Earth's center, the observation point, and the reflection point gives $\sin \theta_i / R_\oplus = \sin(\pi/2 + \gamma) / r = \cos \gamma / r$. Thus $\gamma = \arccos[(r/R_\oplus) \sin \theta_i]$. Specular reflection then gives $\theta = \theta_i + 2\gamma$. **Right.** Contribution from the directly incident ray, which reaches the observation point without reflection. $\theta = \theta_i$.

convenient approach is to first take the analytical radial derivative of c_L in Eq. (C27), and then apply the same numerical procedure used for computing a_L .

As a validity check, we verified that, in the parameter regions of interest, the resulting a_L values are negligibly affected by whether the velocity cutoff is included. The reason is that the contribution to the integration from the phase space of $|\mathbf{k} - \mathbf{k}_0| > k_{\text{esc}}$ is suppressed by the Maxwell-Boltzmann distribution ($k_{\text{esc}}/\sigma_k = 3.23$). As an example, we show the numerical result of a_L and da_L/dr in the hard sphere limit, with $r = 1.1R_\oplus$, in Fig. 6. We also show the results in log-scale in Fig. C.1.

As a cross-check, we perform an additional check to compare the field profile $\langle |\psi|^2 \rangle$ from the a_L calculation and from the direct calculation:

$$\langle |\psi|^2 \rangle = \frac{1}{n_\phi} \int d^3\mathbf{k} f_\phi(\mathbf{k}) |\psi_{\text{out}}(\mathbf{r}; \mathbf{k})|^2, \quad (\text{C40})$$

where the monochromatic wave function comes from the general expression of Eq. (C4). To directly calculate the field profile outside, we solve the phase shift δ_l using Eq. (C11), sum over the partial waves in Eq. (C4) and integrate over the phase space according to Eq. (C40) directly. We compare the field profile from the multipole expansion Eq. (C36) and from direct calculation, with different k_0 , at different angle of location θ_r in Fig. C.2. We can see that the results obtained from the two formalisms agree well with each other.

Appendix D: Optical Limit

In this section, we show how the calculation of the scalar profile and the corresponding background-induced potential can be performed in the optical limit at high DM masses. When the DM wavelength is much smaller than all relevant length scales, in particular the altitude, h , and the radius of the Earth, R_\oplus , the propagation of the DM field can be treated in the formalism of geometric-optics. Before proceeding, we emphasize that this geometric-optics approximation is appropriate when $k_0 R_\oplus, k_0 h \gg 1$ and for $m_{\text{M},\oplus} > k_0$ where the Earth can be treated as a hard sphere.

Since $\langle |\psi|^2 \rangle$ is proportional to the local ULDM density, the normalized ensemble-averaged squared field amplitude

is equal to the normalized local number density,

$$\frac{\langle |\psi|^2 \rangle(\mathbf{r})}{|\psi_0|^2} = \frac{n_\phi(\mathbf{r})}{n_\phi}, \quad (\text{D1})$$

where the \mathbf{r} dependence encodes the spatial inhomogeneity induced by the matter effect. In the optical regime where ϕ is treated as the collection of particles, this number density can be obtained by integrating the spectral radiance divided by the particle velocity, \mathcal{L}/v , over the directions of the incident rays,

$$\frac{n_\phi(\mathbf{r})}{n_\phi} = \frac{1}{n_\phi} \int d\Omega_i \int_0^\infty k^2 dk \frac{\mathcal{L}(\mathbf{r}, \Omega_i, k)}{v}. \quad (\text{D2})$$

Here $v = k/m_\phi$ is the particle velocity, and $d\Omega_i = d\phi_i \sin\theta_i d\theta_i$ is the solid-angle element associated with the direction Ω_i , defined opposite to the ray-propagation direction and therefore labeling the incident ray reaching the point \mathbf{r} . Since the spectral radiance is conserved along each ray, including through specular reflection and direct incidence, we have

$$\mathcal{L}(\mathbf{r}, \Omega_i, k) = \mathcal{L}_\infty(\Omega_{\mathbf{k}}, k), \quad (\text{D3})$$

where $\mathcal{L}_\infty(\Omega_{\mathbf{k}}, k)$ denotes the asymptotic radiance at infinity. We therefore rewrite Eq. (D2) as an integral over the direction of the incident momentum $\hat{\mathbf{k}}$, which is also the asymptotic sky direction $\Omega_{\mathbf{k}} \equiv \hat{\mathbf{k}}$,

$$\begin{aligned} \frac{n_\phi(\mathbf{r})}{n_\phi} &= \int d\Omega_{\mathbf{k}} \left| \frac{d\Omega_i}{d\Omega_{\mathbf{k}}} \right| \frac{1}{n_\phi} \int_0^\infty k^2 dk \frac{\mathcal{L}_\infty(\Omega_{\mathbf{k}}, k)}{k/m_\phi} \\ &= \int d\Omega_{\mathbf{k}} 4\pi T(r, \theta) I(\Omega_{\mathbf{k}}). \end{aligned} \quad (\text{D4})$$

Here θ is the angle between the position vector direction $\hat{\mathbf{r}}$ and the incident momentum direction $\hat{\mathbf{k}}$, as shown in Fig. D.1. $T(r, \theta)$ is defined as

$$T(r, \theta) \equiv \frac{1}{4\pi} \left| \frac{d\Omega_i}{d\Omega_{\mathbf{k}}} \right|, \quad (\text{D5})$$

which is the angular redistribution kernel. With this normalization, $T = 1/(4\pi)$ when the Earth does not redirect the rays. In the optical regime where the scalar is treated as classical particle, the spectral radiance from infinitely far divided by the particle velocity k/m_ϕ is precisely the DM phase-space distribution,

$$\frac{\mathcal{L}_\infty(\Omega_{\mathbf{k}}, k)}{k/m_\phi} = f_\phi(\mathbf{k}), \quad (\text{D6})$$

where k/m_ϕ is the particle velocity and $f_\phi(\mathbf{k})$ is the ULDM phase space distribution in Eq. (40). The angular intensity profile is therefore given by

$$\begin{aligned} I(\Omega_{\mathbf{k}}) &= \frac{1}{n_\phi} \int_0^\infty k^2 dk \frac{\mathcal{L}_\infty(\Omega_{\mathbf{k}}, k)}{k/m_\phi} \\ &= \frac{1}{n_\phi} \int_0^\infty k^2 dk f_\phi(\mathbf{k}), \end{aligned} \quad (\text{D7})$$

which captures the angular distribution of the incident DM. As shown in the second equal sign in Eq. (D7), for fixed geometric factors σ_k/k_0 and k_0/k_{esc} , $I(\Omega_{\mathbf{k}})$ is independent of the DM mass m_ϕ .

Because the kernel $T(r, \theta)$ is azimuthally symmetric around $\hat{\mathbf{r}}$, it can be expanded in terms of Legendre polynomials.

Coefficient	I_0^0	I_1^0	I_2^0	I_3^0	I_4^0	I_5^0
Value	$1/\sqrt{4\pi}$	0.310	0.196	0.0952	0.0386	0.0137

TABLE D.1. The first six $M = 0$ multipole moments of the incident angular intensity for the DM distribution described by the SHM.

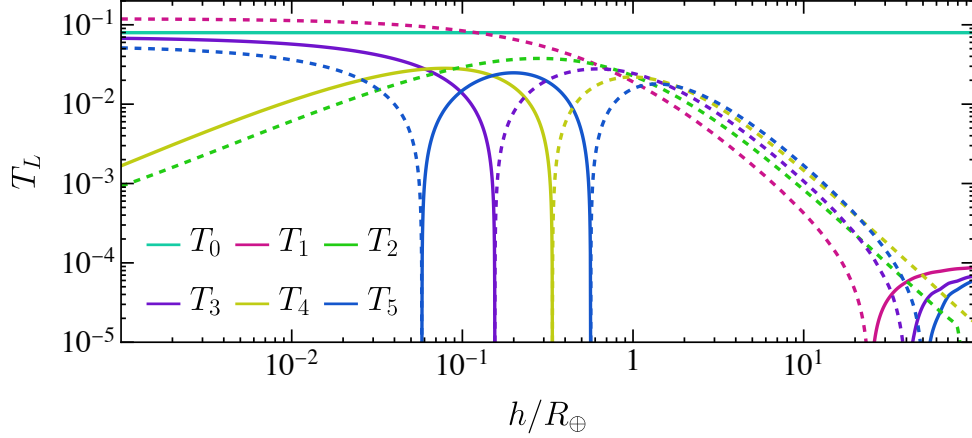


FIG. D.2. Multipole transfer coefficients $T_L(r)$ as a function of h/R_\oplus for $L = 0, \dots, 5$. The solid curves correspond to cases where $T_L > 0$, while the dashed curves indicate cases where $T_L < 0$.

We define the multipole transfer coefficients by

$$T_L(r) = \frac{2L+1}{2} \int_0^\pi \sin\theta \, d\theta T(r, \theta) P_L(\cos\theta). \quad (\text{D8})$$

Equivalently, $T(r, \theta) = \sum_{L=0}^\infty T_L(r) P_L(\cos\theta)$. Note that the coefficients $T_L(r)$, which encode how the geometry of the reflected rays modifies each angular multipole, depend only on the geometry and not on the DM distribution $f_\phi(\mathbf{k})$.

Using the addition theorem of Legendre polynomials, we can then write the ensemble-averaged Eq. (D4) over the DM distribution as

$$\frac{n_\phi(\mathbf{r})}{n_\phi} = \sum_{L=0}^\infty \sum_{M=-L}^L \frac{(4\pi)^2}{2L+1} I_L^M T_L(r) Y_L^M(\Omega_{\mathbf{r}}), \quad (\text{D9})$$

where the index L is chosen to match the convention used in the ensemble-averaged multipole expansion in Appendix C. $\Omega_{\mathbf{r}} \equiv \hat{\mathbf{r}}$ denotes the direction of \mathbf{r} , and the multipole moments of the incident angular intensity are

$$I_L^M = \int d\Omega_{\mathbf{k}} I(\Omega_{\mathbf{k}}) Y_L^{M*}(\Omega_{\mathbf{k}}). \quad (\text{D10})$$

We now compute the angular redistribution kernel using the geometry shown in Fig. D.1. Consider a ray that reaches the observation point at radius r with incidence polar angle θ_i , measured from the inward radial direction. The corresponding asymptotic sky angle is

$$\theta(\theta_i, r) = \begin{cases} \theta_i + 2 \arccos\left(\frac{r}{R_\oplus} \sin\theta_i\right), & \theta_i < \pi/2 \text{ and } \sin\theta_i < R_\oplus/r, \\ \theta_i, & \text{otherwise.} \end{cases} \quad (\text{D11})$$

The first line applies to rays that intersect the Earth and undergo specular reflection before reaching the observation point, as illustrated in the left panel of Fig. D.1. The second line applies to unreflected rays that reach the observation point directly, as illustrated in the right panel of Fig. D.1.

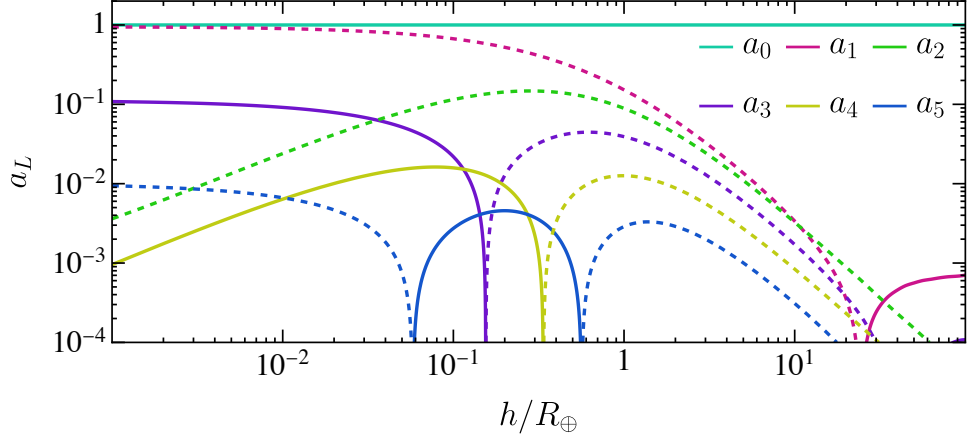


FIG. D.3. The a_L -series as a function of h/R_\oplus for $L = 0, \dots, 5$ in the optical limit and the SHM. The solid curves correspond to cases where $a_L > 0$, while the dashed curves indicate cases where $a_L < 0$. We have numerically verified the consistency between the optical-limit calculation of a_L and the multipole-expansion method described in Sec. III C 2, in the regime $k_0 R_\oplus \gg 1$ and $k_0 h \gg 1$.

Rather than writing a closed-form expression for the kernel, we compute it as the probability density for a uniformly distributed local ray direction to map to a given point on the asymptotic sky. Let $p_r(\theta)$ be the one-dimensional probability density obtained by applying Eq. (D11) while sampling $\cos \theta_i$ uniformly on $[-1, 1]$. Equivalently,

$$p_r(\theta) = \frac{1}{2} \sum_{\theta_i: \theta(\theta_i, r) = \theta} \left| \frac{d \cos \theta_i}{d\theta} \right|. \quad (\text{D12})$$

Azimuthal symmetry then gives

$$T(r, \theta) = \frac{p_r(\theta)}{2\pi \sin \theta}. \quad (\text{D13})$$

This form is convenient for numerical evaluation of the transfer coefficients in Eq. (D8).

For this work, we take the SHM for the DM distribution. Figure D.2 shows the first few T_L as a function of h/R_\oplus while Table D.1 lists the first six $M = 0$ multipole coefficients I_L^0 for the SHM. For the SHM, the incident angular distribution is axially symmetric. If the polar axis is chosen along the DM halo-wind \mathbf{k}_0 as shown in Fig. 4, then only the coefficients with $M = 0$ are nonzero, and Eq. (D9) reduces to

$$\frac{n_\phi(r, \theta_{\mathbf{r}})}{n_\phi} = \sum_{L=0}^{\infty} 4\pi \sqrt{\frac{4\pi}{2L+1}} I_L^0 T_L(r) P_L(\cos \theta_{\mathbf{r}}), \quad (\text{D14})$$

where $\theta_{\mathbf{r}}$ is the angle between \mathbf{r} and the halo-wind axis \mathbf{k}_0 . Comparing Eq. (D14) with Eq. (42), the optical limit gives

$$a_L(r) = 4\pi \sqrt{\frac{4\pi}{2L+1}} I_L^0 T_L(r). \quad (\text{D15})$$

Figure D.3 shows first few a_L as a function of h/R_\oplus in the optical limit. Recalling that $r = h + R_\oplus$, this figure shows that, in the optical limit, $a_0(r) \rightarrow 1$ so the monopole contribution to the background-induced force vanishes in contrast with the spherical limit, where the monopole provides the only contribution. This explains the strong suppression of da_0/dr in the large- $k_0 R_\oplus$ limit, in contrast to the higher-multipole derivatives da_L/dr with $L \geq 1$, which approach nonzero constants, as shown in Fig. 6 and Fig. C.1.

As a consistency check, we numerically verified that the optical-limit calculation of a_L given by Eq. (D15) agrees with the ensemble-averaged multipole-expansion method described in Sec. III C 2 in the regime $k_0 R_\oplus \gg 1$ and $k_0 h \gg 1$

over the full range of h/R_\oplus considered. For the MICROSCOPE altitude, $h = 0.1 R_\oplus$, once $k_0 h \gg 1$, or equivalently $k_0 R_\oplus \gg 10$, the optical-limit values of a_L agree with the large- $k_0 R_\oplus$ behavior shown in Fig. 5 and in the left panel of Fig. C.1. The finite-difference derivatives $da_L/d(r/R_\oplus)$ likewise agree with Fig. 6 and the right panel of Fig. C.1.

-
- [1] D. Antypas *et al.*, “New Horizons: Scalar and Vector Ultralight Dark Matter,” (2022), [arXiv:2203.14915 \[hep-ex\]](#).
 - [2] Thibault Damour and John F. Donoghue, “Phenomenology of the Equivalence Principle with Light Scalars,” *Class. Quant. Grav.* **27**, 202001 (2010), [arXiv:1007.2790 \[gr-qc\]](#).
 - [3] Thibault Damour and John F. Donoghue, “Equivalence Principle Violations and Couplings of a Light Dilaton,” *Phys. Rev. D* **82**, 084033 (2010), [arXiv:1007.2792 \[gr-qc\]](#).
 - [4] Y. V. Stadnik and V. V. Flambaum, “Can dark matter induce cosmological evolution of the fundamental constants of Nature?” *Phys. Rev. Lett.* **115**, 201301 (2015), [arXiv:1503.08540 \[astro-ph.CO\]](#).
 - [5] Jean-Philippe Uzan, “Fundamental constants: from measurement to the universe, a window on gravitation and cosmology,” (2024), [arXiv:2410.07281 \[astro-ph.CO\]](#).
 - [6] Asimina Arvanitaki, Junwu Huang, and Ken Van Tilburg, “Searching for dilaton dark matter with atomic clocks,” *Phys. Rev. D* **91**, 015015 (2015), [arXiv:1405.2925 \[hep-ph\]](#).
 - [7] Ken Van Tilburg, Nathan Leefler, Lykourgos Bougas, and Dmitry Budker, “Search for ultralight scalar dark matter with atomic spectroscopy,” *Phys. Rev. Lett.* **115**, 011802 (2015), [arXiv:1503.06886 \[physics.atom-ph\]](#).
 - [8] A. Hees, J. Guéna, M. Abgrall, S. Bize, and P. Wolf, “Searching for an oscillating massive scalar field as a dark matter candidate using atomic hyperfine frequency comparisons,” *Phys. Rev. Lett.* **117**, 061301 (2016), [arXiv:1604.08514 \[gr-qc\]](#).
 - [9] P. Wcisło *et al.*, “New bounds on dark matter coupling from a global network of optical atomic clocks,” *Sci. Adv.* **4**, eaau4869 (2018), [arXiv:1806.04762 \[physics.atom-ph\]](#).
 - [10] Colin J Kennedy, Eric Oelker, John M Robinson, Tobias Bothwell, Dhruv Kedar, William R Milner, G Edward Marti, Andrei Derevianko, and Jun Ye, “Precision metrology meets cosmology: improved constraints on ultralight dark matter from atom-cavity frequency comparisons,” *Physical Review Letters* **125**, 201302 (2020).
 - [11] M. Filzinger, S. Dörscher, R. Lange, J. Klose, M. Steinel, E. Benkler, E. Peik, C. Lisdat, and N. Huntemann, “Improved Limits on the Coupling of Ultralight Bosonic Dark Matter to Photons from Optical Atomic Clock Comparisons,” *Phys. Rev. Lett.* **130**, 253001 (2023), [arXiv:2301.03433 \[physics.atom-ph\]](#).
 - [12] Melina Filzinger, Ashlee R. Caddell, Dhruv Jani, Martin Steinel, Leonardo Giani, Nils Huntemann, and Benjamin M. Roberts, “Ultralight Dark Matter Search with Space-Time Separated Atomic Clocks and Cavities,” *Phys. Rev. Lett.* **134**, 031001 (2025), [arXiv:2312.13723 \[hep-ph\]](#).
 - [13] Peter W. Graham, David E. Kaplan, Jeremy Mardon, Surjeet Rajendran, and William A. Terrano, “Dark Matter Direct Detection with Accelerometers,” *Phys. Rev. D* **93**, 075029 (2016), [arXiv:1512.06165 \[hep-ph\]](#).
 - [14] Aurélien Hees, Olivier Minazzoli, Etienne Savalle, Yevgeny V. Stadnik, and Peter Wolf, “Violation of the equivalence principle from light scalar dark matter,” *Phys. Rev. D* **98**, 064051 (2018), [arXiv:1807.04512 \[gr-qc\]](#).
 - [15] Ken Van Tilburg, “Wake forces in a background of quadratically coupled mediators,” *Phys. Rev. D* **109**, 096036 (2024).
 - [16] Clare Burrage, Angus Macdonald, and Elisa Todarello, “Using the Pericentre Precession of LAGEOS II to Constrain Quadratically Coupled Ultralight Dark Matter,” (2026), [arXiv:2605.28248 \[hep-ph\]](#).
 - [17] Yousef Abou El-Neaj *et al.* (AEDGE), “AEDGE: Atomic Experiment for Dark Matter and Gravity Exploration in Space,” *EPJ Quant. Technol.* **7**, 6 (2020), [arXiv:1908.00802 \[gr-qc\]](#).
 - [18] L. Badurina *et al.*, “AION: An Atom Interferometer Observatory and Network,” *JCAP* **05**, 011 (2020), [arXiv:1911.11755 \[astro-ph.CO\]](#).
 - [19] Mahiro Abe *et al.* (MAGIS-100), “Matter-wave Atomic Gradiometer Interferometric Sensor (MAGIS-100),” *Quantum Sci. Technol.* **6**, 044003 (2021), [arXiv:2104.02835 \[physics.atom-ph\]](#).
 - [20] Wei Zhao, Xitong Mei, Dongfeng Gao, Jin Wang, and Mingsheng Zhan, “Ultralight scalar dark matter detection with ZAIGA,” *Int. J. Mod. Phys. D* **31**, 2250037 (2022), [arXiv:2110.11564 \[physics.atom-ph\]](#).
 - [21] Nataliya K. Porayko *et al.*, “Parkes Pulsar Timing Array constraints on ultralight scalar-field dark matter,” *Phys. Rev. D* **98**, 102002 (2018), [arXiv:1810.03227 \[astro-ph.CO\]](#).
 - [22] Yu-Mei Wu, Zu-Cheng Chen, Qing-Guo Huang, Xingjiang Zhu, N. D. Ramesh Bhat, Yi Feng, George Hobbs, Richard N. Manchester, Christopher J. Russell, and R. M. Shannon (PPTA), “Constraining ultralight vector dark matter with the Parkes Pulsar Timing Array second data release,” *Phys. Rev. D* **106**, L081101 (2022), [arXiv:2210.03880 \[astro-ph.CO\]](#).
 - [23] David E. Kaplan, Andrea Mitridate, and Tanner Trickle, “Constraining fundamental constant variations from ultralight dark matter with pulsar timing arrays,” *Phys. Rev. D* **106**, 035032 (2022), [arXiv:2205.06817 \[hep-ph\]](#).

- [24] Xucheng Gan, Hyungjin Kim, and Andrea Mitridate, “Probing Quadratically Coupled Ultralight Dark Matter with Pulsar Timing Arrays,” (2025), [arXiv:2510.13945 \[hep-ph\]](#).
- [25] Abhishek Banerjee, Gilad Perez, Marianna Safronova, Inbar Savoray, and Aviv Shalit, “The phenomenology of quadratically coupled ultra light dark matter,” *JHEP* **10**, 042 (2023), [arXiv:2211.05174 \[hep-ph\]](#).
- [26] T. A. Wagner, S. Schlamminger, J. H. Gundlach, and E. G. Adelberger, “Torsion-balance tests of the weak equivalence principle,” *Class. Quant. Grav.* **29**, 184002 (2012), [arXiv:1207.2442 \[gr-qc\]](#).
- [27] Joel Bergé, Philippe Brax, Gilles Métris, Martin Pernot-Borràs, Pierre Touboul, and Jean-Philippe Uzan, “MICROSCOPE Mission: First Constraints on the Violation of the Weak Equivalence Principle by a Light Scalar Dilaton,” *Phys. Rev. Lett.* **120**, 141101 (2018), [arXiv:1712.00483 \[gr-qc\]](#).
- [28] Pierre Touboul *et al.*, “Result of the MICROSCOPE weak equivalence principle test,” *Class. Quant. Grav.* **39**, 204009 (2022), [arXiv:2209.15488 \[gr-qc\]](#).
- [29] Lasha Berezhiani and Justin Khoury, “Emergent long-range interactions in Bose-Einstein Condensates,” *Phys. Rev. D* **99**, 076003 (2019), [arXiv:1812.09332 \[hep-th\]](#).
- [30] Xucheng Gan, Da Liu, Di Liu, Xuheng Luo, and Bingrong Yu, “Detecting ultralight dark matter with matter effect,” *JHEP* **02**, 043 (2026), [arXiv:2504.11522 \[hep-ph\]](#).
- [31] Abhishek Banerjee, Itay M. Bloch, Quentin Bonnefoy, Sebastian A. R. Ellis, Gilad Perez, Inbar Savoray, Konstantin Springmann, and Yevgeny V. Stadnik, “Momentum and Matter Matter for Axion Dark Matter Matters on Earth,” (2025), [arXiv:2502.04455 \[hep-ph\]](#).
- [32] Yeray Garcia del Castillo, Benjamin Hammett, and Joerg Jaeckel, “Enhanced Axion-wind near Earth’s Surface,” (2025), [arXiv:2502.04456 \[hep-ph\]](#).
- [33] Thomas Bouley, Philip Sørensen, and Tien-Tien Yu, “Constraints on ultralight scalar dark matter with quadratic couplings,” *JHEP* **03**, 104 (2023), [arXiv:2211.09826 \[hep-ph\]](#).
- [34] Anson Hook, “Solving the Hierarchy Problem Discretely,” *Phys. Rev. Lett.* **120**, 261802 (2018), [arXiv:1802.10093 \[hep-ph\]](#).
- [35] Anson Hook, “Naturalness without new particles,” *JHEP* **04**, 048 (2021), [arXiv:1902.06758 \[hep-ph\]](#).
- [36] Dawid Brzemiński, Zackaria Chacko, Abhish Dev, and Anson Hook, “Time-varying fine structure constant from naturally ultralight dark matter,” *Phys. Rev. D* **104**, 075019 (2021), [arXiv:2012.02787 \[hep-ph\]](#).
- [37] Luca Di Luzio, Belen Gavela, Pablo Quilez, and Andreas Ringwald, “An even lighter QCD axion,” *JHEP* **05**, 184 (2021), [arXiv:2102.00012 \[hep-ph\]](#).
- [38] Luca Di Luzio, Belen Gavela, Pablo Quilez, and Andreas Ringwald, “Dark matter from an even lighter QCD axion: trapped misalignment,” *JCAP* **10**, 001 (2021), [arXiv:2102.01082 \[hep-ph\]](#).
- [39] Xucheng Gan and Di Liu, “Cosmologically varying kinetic mixing,” *JHEP* **11**, 031 (2023), [arXiv:2302.03056 \[hep-ph\]](#).
- [40] Cédric Delaunay, Michael Geller, Zamir Heller-Algazi, Gilad Perez, and Konstantin Springmann, “Natural Ultralight Dark Matter: The Quadratic Twin,” (2025), [arXiv:2507.12514 \[hep-ph\]](#).
- [41] Mathias Becker, Francesco D’Eramo, and Ville Vaskonen, “Ultralight Dark Matter from the Edge of Field Space,” *Phys. Rev. Lett.* **136**, 201003 (2026), [arXiv:2511.09622 \[hep-ph\]](#).
- [42] Murray Gell-Mann, R. J. Oakes, and B. Renner, “Behavior of current divergences under $SU(3) \times SU(3)$,” *Phys. Rev.* **175**, 2195–2199 (1968).
- [43] Stefan Scherer, “Introduction to chiral perturbation theory,” *Adv. Nucl. Phys.* **27**, 277 (2003), [arXiv:hep-ph/0210398](#).
- [44] Federico Piazza and Maxim Pospelov, “Sub-eV scalar dark matter through the super-renormalizable Higgs portal,” *Phys. Rev. D* **82**, 043533 (2010), [arXiv:1003.2313 \[hep-ph\]](#).
- [45] S. Navas *et al.* (Particle Data Group), “Review of particle physics,” *Phys. Rev. D* **110**, 030001 (2024).
- [46] C. Brans and R. H. Dicke, “Mach’s Principle and a Relativistic Theory of Gravitation,” *Phys. Rev.* **124**, 925–935 (1961).
- [47] T. Damour and G. Esposito-Farese, “Tensor-multi-scalar theories of gravitation,” *Class. Quant. Grav.* **9**, 2093–2176 (1992).
- [48] Sergey Sibiryakov, Philip Sørensen, and Tien-Tien Yu, “BBN constraints on universally-coupled ultralight scalar dark matter,” *JHEP* **12**, 075 (2020), [arXiv:2006.04820 \[hep-ph\]](#).
- [49] Yasunori Fujii, “Role of regularization in quantum corrections to the scalar - tensor theories of gravity,” *Mod. Phys. Lett. A* **12**, 371–380 (1997), [arXiv:gr-qc/9610006](#).
- [50] Lam Hui and Alberto Nicolis, “An Equivalence principle for scalar forces,” *Phys. Rev. Lett.* **105**, 231101 (2010), [arXiv:1009.2520 \[hep-th\]](#).
- [51] Cristian Armendariz-Picon and Riccardo Penco, “Quantum Equivalence Principle Violations in Scalar-Tensor Theories,” *Phys. Rev. D* **85**, 044052 (2012), [arXiv:1108.6028 \[hep-th\]](#).
- [52] Francesco Nitti and Federico Piazza, “Scalar-tensor theories, trace anomalies and the QCD-frame,” *Phys. Rev. D* **86**, 122002 (2012), [arXiv:1202.2105 \[hep-th\]](#).
- [53] Anson Hook and Junwu Huang, “Probing axions with neutron star inspirals and other stellar processes,” *JHEP* **06**, 036

- (2018), [arXiv:1708.08464 \[hep-ph\]](#).
- [54] Lorenzo Ubaldi, “Effects of theta on the deuteron binding energy and the triple-alpha process,” *Phys. Rev. D* **81**, 025011 (2010), [arXiv:0811.1599 \[hep-ph\]](#).
- [55] Giovanni Grilli di Cortona, Edward Hardy, Javier Pardo Vega, and Giovanni Villadoro, “The QCD axion, precisely,” *JHEP* **01**, 034 (2016), [arXiv:1511.02867 \[hep-ph\]](#).
- [56] Mia Kumamoto, Junwu Huang, Christian Drischler, Masha Baryakhtar, and Sanjay Reddy, “Neutron stars with exceptionally light QCD axions,” *Phys. Rev. D* **112**, 043008 (2025), [arXiv:2410.21590 \[hep-ph\]](#).
- [57] Jordan Gué, Aurélien Hees, and Peter Wolf, “Violation of the equivalence principle induced by oscillating rest mass and transition frequency, and its detection in atom interferometers,” *Phys. Rev. D* **110**, 035005 (2024), [arXiv:2401.14742 \[hep-ph\]](#).
- [58] Martin Bauer, Sreemanti Chakraborti, and Guillaume Rostagni, “Axion bounds from quantum technology,” *JHEP* **05**, 023 (2025), [arXiv:2408.06412 \[hep-ph\]](#).
- [59] Jordan Gué, Peter Wolf, and Aurélien Hees, “Search for QCD coupled axion dark matter with the MICROSCOPE space experiment,” (2025), [arXiv:2504.00720 \[hep-ph\]](#).
- [60] C. Abel *et al.*, “Search for Axionlike Dark Matter through Nuclear Spin Precession in Electric and Magnetic Fields,” *Phys. Rev. X* **7**, 041034 (2017), [arXiv:1708.06367 \[hep-ph\]](#).
- [61] Reuven Balkin, Javi Serra, Konstantin Springmann, Stefan Stelzl, and Andreas Weiler, “White dwarfs as a probe of exceptionally light QCD axions,” *Phys. Rev. D* **109**, 095032 (2024), [arXiv:2211.02661 \[hep-ph\]](#).
- [62] Samuel J. Witte, Andrea Caputo, Stefan Stelzl, Alexander Chernoglazov, Alexander A. Philippov, and Surjeet Rajendran, “Constraints on light QCD and CP-violating axions from the death line of rotation-powered pulsars,” (2025), [arXiv:2512.11023 \[hep-ph\]](#).
- [63] L. Wolfenstein, “Neutrino Oscillations in Matter,” *Phys. Rev. D* **17**, 2369–2374 (1978).
- [64] S. P. Mikheyev and A. Yu. Smirnov, “Resonance Amplification of Oscillations in Matter and Spectroscopy of Solar Neutrinos,” *Sov. J. Nucl. Phys.* **42**, 913–917 (1985).
- [65] S. P. Mikheyev and A. Yu. Smirnov, “Resonant amplification of neutrino oscillations in matter and solar neutrino spectroscopy,” *Nuovo Cim. C* **9**, 17–26 (1986).
- [66] F. J. Botella, C. S. Lim, and W. J. Marciano, “Radiative Corrections to Neutrino Indices of Refraction,” *Phys. Rev. D* **35**, 896 (1987).
- [67] Dirk Nötzold and Georg Raffelt, “Neutrino dispersion at finite temperature and density,” *Nucl. Phys. B* **307**, 924–936 (1988).
- [68] Alessandro Mirizzi, Stefano Pozzorini, Georg G. Raffelt, and Pasquale D. Serpico, “Flavour-dependent radiative correction to neutrino-neutrino refraction,” *JHEP* **10**, 020 (2009), [arXiv:0907.3674 \[hep-ph\]](#).
- [69] Jihong Huang and Shun Zhou, “Mikheyev-Smirnov-Wolfenstein matter potential at the one-loop level in the Standard Model,” *Phys. Rev. D* **108**, 093010 (2023), [arXiv:2307.04685 \[hep-ph\]](#).
- [70] W. Meissner and R. Ochsenfeld, “Ein neuer Effekt bei Eintritt der Supraleitfähigkeit,” *Naturwiss.* **21**, 787–788 (1933).
- [71] John David Jackson, *Classical Electrodynamics* (Wiley, 1998).
- [72] J. E. Moody and Frank Wilczek, “NEW MACROSCOPIC FORCES?” *Phys. Rev. D* **30**, 130 (1984).
- [73] G. Feinberg, J. Sucher, and C. K. Au, “The Dispersion Theory of Dispersion Forces,” *Phys. Rept.* **180**, 83 (1989).
- [74] F. Ferrer and J. A. Grifols, “Effects of Bose-Einstein condensation on forces among bodies sitting in a boson heat bath,” *Phys. Rev. D* **63**, 025020 (2001), [arXiv:hep-ph/0001185](#).
- [75] Thibault Damour, Federico Piazza, and Gabriele Veneziano, “Runaway dilaton and equivalence principle violations,” *Phys. Rev. Lett.* **89**, 081601 (2002), [arXiv:gr-qc/0204094](#).
- [76] Sylvain Fichet, “Quantum Forces from Dark Matter and Where to Find Them,” *Phys. Rev. Lett.* **120**, 131801 (2018), [arXiv:1705.10331 \[hep-ph\]](#).
- [77] Martin Bauer and Guillaume Rostagni, “Fifth Forces from QCD Axions Scale Differently,” *Phys. Rev. Lett.* **132**, 101802 (2024), [arXiv:2307.09516 \[hep-ph\]](#).
- [78] Yuval Grossman, Chinhsan Sieng, Xun-Jie Xu, and Bingrong Yu, “Strongly Coupled Quantum Forces,” (2025), [arXiv:2512.05968 \[hep-ph\]](#).
- [79] Mitrajyoti Ghosh, Yuval Grossman, Walter Tangarife, Xun-Jie Xu, and Bingrong Yu, “Neutrino forces in neutrino backgrounds,” *JHEP* **02**, 092 (2023), [arXiv:2209.07082 \[hep-ph\]](#).
- [80] Diego Blas, Ivan Esteban, M. C. Gonzalez-Garcia, and Jordi Salvado, “On neutrino-mediated potentials in a neutrino background,” *JHEP* **04**, 039 (2023), [arXiv:2212.03889 \[hep-ph\]](#).
- [81] Sergio Barbosa and Sylvain Fichet, “Background-induced forces from dark relics,” *JHEP* **01**, 021 (2025), [arXiv:2403.13894 \[hep-ph\]](#).
- [82] Mitrajyoti Ghosh, Yuval Grossman, Walter Tangarife, Xun-Jie Xu, and Bingrong Yu, “The neutrino force in neutrino

- backgrounds: Spin dependence and parity-violating effects,” *JHEP* **07**, 107 (2024), [arXiv:2405.16801 \[hep-ph\]](#).
- [83] Yuval Grossman, Bingrong Yu, and Siyu Zhou, “Axion forces in axion backgrounds,” *JHEP* **01**, 145 (2026), [arXiv:2504.00104 \[hep-ph\]](#).
- [84] Yu Cheng and Shuaailiang Ge, “Background-Enhanced Axion Force by Axion Dark Matter,” (2025), [arXiv:2504.02702 \[hep-ph\]](#).
- [85] Jakob Rieser, Mario A. Ciampini, Henning Rudolph, Nikolai Kiesel, Klaus Hornberger, Benjamin A. Stickler, Markus Aspelmeyer, and Uroš Delić, “Tunable light-induced dipole-dipole interaction between optically levitated nanoparticles,” *Science* **377**, abp9941 (2022), [arXiv:2203.04198 \[physics.optics\]](#).
- [86] Henning Rudolph, Uroš Delić, Klaus Hornberger, and Benjamin A. Stickler, “Quantum Optical Binding of Nanoscale Particles,” *Phys. Rev. Lett.* **133**, 233603 (2024), [arXiv:2412.03204 \[quant-ph\]](#).
- [87] S. Seager, M. Kuchner, C. n Hier-Majumder, and B. Militzer, “Mass-Radius Relationships for Solid Exoplanets,” *Astro-phys. J.* **669**, 1279 (2007), [arXiv:0707.2895 \[astro-ph\]](#).
- [88] William F McDonough, “Compositional model for the earth’s core,” *Treatise on geochemistry* **2**, 568 (2003).
- [89] Aleksandr Belokon and Anna Tokareva, “Light scalar dark matter coupled to a trace of energy-momentum tensor,” *Phys. Rev. D* **101**, 103535 (2020), [arXiv:1812.04065 \[hep-ph\]](#).
- [90] Masha Baryakhtar, Olivier Simon, and Zachary J. Weiner, “Cosmology with varying fundamental constants from hyperlight, coupled scalars,” *Phys. Rev. D* **110**, 083505 (2024), [arXiv:2405.10358 \[astro-ph.CO\]](#).
- [91] Masha Baryakhtar, Olivier Simon, and Zachary J. Weiner, “Searching for coupled, hyperlight scalars across cosmic history,” (2025), [arXiv:2502.04432 \[hep-ph\]](#).
- [92] Subhajit Ghosh, Kimberly K. Boddy, and Tien-Tien Yu, “Early Universe Constraints on Variations in Fundamental Constants Induced by Ultralight Scalar Dark Matter,” (2025), [arXiv:2511.14532 \[astro-ph.CO\]](#).
- [93] James D. Bjorken and Sidney D. Drell, *Relativistic Quantum Mechanics*, International Series In Pure and Applied Physics (McGraw-Hill, New York, 1965).
- [94] Walter Greiner, *Relativistic Quantum Mechanics. Wave Equations* (Springer, Berlin, 1997).
- [95] Helmut Moritz, “Geodetic reference system 1980,” *Journal of geodesy* **74**, 128–133 (2000).
- [96] Brian Luzum, Nicole Capitaine, Agnès Fienga, William Folkner, Toshio Fukushima, James Hilton, Catherine Hohenkerk, George Krasinsky, Gérard Petit, Elena Pitjeva, *et al.*, “The iau 2009 system of astronomical constants: the report of the iau working group on numerical standards for fundamental astronomy,” *Celestial Mechanics and Dynamical Astronomy* **110**, 293–304 (2011).
- [97] E. E. Mamajek *et al.* (IAU Inter-Division A-G Working Group on Nominal Units for Stellar & Planetary Astronomy), “IAU 2015 Resolution B3 on Recommended Nominal Conversion Constants for Selected Solar and Planetary Properties,” (2015), [arXiv:1510.07674 \[astro-ph.SR\]](#).
- [98] A. M Nobili, D Bramanti, E Polacco, G Catastini, A Anselmi, S Portigliotti, A Lenti, and A Severi, “The ‘Galileo Galilei’ (GG) project: Testing the Equivalence Principle in space and on Earth,” *Adv. Space Res.* **25**, 1231–1235 (2000).
- [99] A. M. Nobili *et al.*, “‘Galileo Galilei’ (GG): Space test of the weak equivalence principle to 10⁽⁻¹⁷⁾ and laboratory demonstrations,” *Class. Quant. Grav.* **29**, 184011 (2012).
- [100] Anna M. Nobili and Alberto Anselmi, “Relevance of the weak equivalence principle and experiments to test it: Lessons from the past and improvements expected in space,” *Phys. Lett. A* **382**, 2205–2218 (2018), [arXiv:1709.02768 \[gr-qc\]](#).
- [101] Anna M. Nobili and Alberto Anselmi, “Testing the Equivalence Principle in space after the MICROSCOPE mission,” *Phys. Rev. D* **98**, 042002 (2018), [arXiv:1803.03313 \[gr-qc\]](#).
- [102] Pierre Touboul *et al.*, “MICROSCOPE Mission: First Results of a Space Test of the Equivalence Principle,” *Phys. Rev. Lett.* **119**, 231101 (2017), [arXiv:1712.01176 \[astro-ph.IM\]](#).
- [103] Pierre Touboul *et al.* (MICROSCOPE), “Space test of the Equivalence Principle: first results of the MICROSCOPE mission,” *Class. Quant. Grav.* **36**, 225006 (2019), [arXiv:1909.10598 \[gr-qc\]](#).
- [104] Pierre Touboul *et al.* (MICROSCOPE), “MICROSCOPE Mission: Final Results of the Test of the Equivalence Principle,” *Phys. Rev. Lett.* **129**, 121102 (2022), [arXiv:2209.15487 \[gr-qc\]](#).
- [105] Lev Davidovich Landau and E. M. Lifshits, *Quantum Mechanics: Non-Relativistic Theory*, Course of Theoretical Physics, Vol. v.3 (Butterworth-Heinemann, Oxford, 1991).
- [106] Jun John Sakurai and Jim Napolitano, *Modern Quantum Mechanics*, Quantum physics, quantum information and quantum computation (Cambridge University Press, 2020).
- [107] Vadim A. Bednyakov and Dmitry V. Naumov, “Coherency and incoherency in neutrino-nucleus elastic and inelastic scattering,” *Phys. Rev. D* **98**, 053004 (2018), [arXiv:1806.08768 \[hep-ph\]](#).
- [108] Dawid Brzeminski and Aaron Pierce, “Searching for Ultralight Scalar Dark Matter with Clocks in Low Earth Orbit,” (2026), [arXiv:2601.16259 \[hep-ph\]](#).
- [109] Andrei Derevianko, “Detecting dark-matter waves with a network of precision-measurement tools,” *Phys. Rev. A* **97**,

- 042506 (2018), arXiv:1605.09717 [physics.atom-ph].
- [110] Joshua W. Foster, Nicholas L. Rodd, and Benjamin R. Safdi, “Revealing the Dark Matter Halo with Axion Direct Detection,” *Phys. Rev. D* **97**, 123006 (2018), arXiv:1711.10489 [astro-ph.CO].
- [111] Mariangela Lisanti, Matthew Moschella, and William Terrano, “Stochastic properties of ultralight scalar field gradients,” *Phys. Rev. D* **104**, 055037 (2021), arXiv:2107.10260 [astro-ph.CO].
- [112] Lam Hui, “Wave Dark Matter,” *Ann. Rev. Astron. Astrophys.* **59**, 247–289 (2021), arXiv:2101.11735 [astro-ph.CO].
- [113] Hyungjin Kim, “Gravitational interaction of ultralight dark matter with interferometers,” *JCAP* **12**, 018 (2023), arXiv:2306.13348 [hep-ph].
- [114] Dhong Yeon Cheong, Nicholas L. Rodd, and Lian-Tao Wang, “Quantum description of wave dark matter,” *Phys. Rev. D* **111**, 015028 (2025), arXiv:2408.04696 [hep-ph].
- [115] D. Baxter *et al.*, “Recommended conventions for reporting results from direct dark matter searches,” *Eur. Phys. J. C* **81**, 907 (2021), arXiv:2105.00599 [hep-ex].
- [116] Guo-yuan Huang, “Neutrino-antineutrino asymmetry of $C\nu B$ on the surface of the round Earth,” *JHEP* **11**, 153 (2024), arXiv:2401.07347 [hep-ph].
- [117] Andrei Gruzinov and Mehrdad Mirbabayi, “The Density of Relic Neutrinos Near the Surface of Earth,” (2024), arXiv:2403.03152 [hep-ph].
- [118] Saarik Kalia, “Tunneling away the relic neutrino asymmetry,” *Phys. Rev. D* **110**, 053001 (2024), arXiv:2404.11664 [hep-ph].
- [119] Thomas Bouley, *Diverse Approaches to Ultralight Dark Matter*, Ph.D. thesis, Oregon U. (2025).
- [120] P. Touboul, G. Metris, V. Lebat, and A. Robert, “The MICROSCOPE experiment, ready for the in-orbit test of the equivalence principle,” *Class. Quant. Grav.* **29**, 184010 (2012).
- [121] Alain Robert *et al.*, “MICROSCOPE satellite and its drag-free and attitude control system,” *Class. Quant. Grav.* **39**, 204003 (2022), arXiv:2012.06479 [gr-qc].
- [122] Manuel Rodrigues *et al.*, “MICROSCOPE mission scenario, ground segment and data processing,” *Class. Quant. Grav.* **39**, 204004 (2022), arXiv:2201.10841 [astro-ph.IM].
- [123] United States Space Force, “Two-Line Element Sets / Orbital Mean-Element Messages for MICROSCOPE (NORAD ID 41457),” Space-Track.org, generated by the 18th Space Defense Squadron, U.S. Space Command (USSPACECOM) (2026), accessed via <https://www.space-track.org>.
- [124] David A Vallado, *Fundamentals of astrodynamics and applications*, Vol. 12 (Springer Science & Business Media, 2001).
- [125] NASA LAMBDA Team, “LAMBDA – astronomical coordinate conversion utility,” NASA Goddard Space Flight Center, Astrophysics Science Division (2026), online tool, accessed 2026-05-10.
- [126] Pierre Fayet, “MICROSCOPE limits for new long-range forces and implications for unified theories,” *Phys. Rev. D* **97**, 055039 (2018), arXiv:1712.00856 [hep-ph].
- [127] Pierre Fayet, “MICROSCOPE limits on the strength of a new force, with comparisons to gravity and electromagnetism,” *Phys. Rev. D* **99**, 055043 (2019), arXiv:1809.04991 [hep-ph].
- [128] Dorian W. P. Amaral, Mudit Jain, Mustafa A. Amin, and Christopher Tunnell, “Vector wave dark matter and terrestrial quantum sensors,” *JCAP* **06**, 050 (2024), arXiv:2403.02381 [hep-ph].
- [129] Hannah Day, Da Liu, Markus A. Luty, and Yue Zhao, “Blowing in the dark matter wind,” *JHEP* **07**, 136 (2024), arXiv:2312.13345 [hep-ph].
- [130] Cheng-Tao Fu, Peng-Shun Luo, Rui Luo, Jie Sheng, and Chuan-Yang Xing, “Macroscopic Quantum Interference in Dark Matter Wave Scattering with MICROSCOPE,” (2026), arXiv:2606.07008 [hep-ph].
- [131] Glen Cowan, Kyle Cranmer, Eilam Gross, and Ofer Vitells, “Asymptotic formulae for likelihood-based tests of new physics,” *Eur. Phys. J. C* **71**, 1554 (2011), [Erratum: *Eur.Phys.J.C* 73, 2501 (2013)], arXiv:1007.1727 [physics.data-an].
- [132] Michele Maggiore, *Gravitational Waves. Vol. 1: Theory and Experiments* (Oxford University Press, 2007).
- [133] Hooman Davoudiasl and Peter B Denton, “Ultralight Boson Dark Matter and Event Horizon Telescope Observations of M87*,” *Phys. Rev. Lett.* **123**, 021102 (2019), arXiv:1904.09242 [astro-ph.CO].
- [134] Masha Baryakhtar, Marios Galanis, Robert Lasenby, and Olivier Simon, “Black hole superradiance of self-interacting scalar fields,” *Phys. Rev. D* **103**, 095019 (2021), arXiv:2011.11646 [hep-ph].
- [135] Meng He, Xi Chen, Jie Fang, Qunfeng Chen, Huanyao Sun, Yibo Wang, Jiaqi Zhong, Lin Zhou, Chuan He, Jinting Li, *et al.*, “The space cold atom interferometer for testing the equivalence principle in the china space station,” *npj Microgravity* **9**, 58 (2023).
- [136] Dan-Fang Zhang *et al.*, “In-orbit Test of the Weak Equivalence Principle with Atom Interferometry,” (2026), arXiv:2603.22981 [physics.atom-ph].
- [137] Naceur Gaaloul *et al.* (STE-QUEST), “STE-QUEST – Space Time Explorer and QUantum Equivalence principle Space Test: The 2022 medium-class mission concept,” (2022), arXiv:2211.15412 [physics.space-ph].

- [138] Christian Struckmann, Robin Corgier, Sina Loriani, Gina Kleinsteinberg, Nina Gox, Enno Giese, Gilles Métris, Naceur Gaaloul, and Peter Wolf, “Platform and environment requirements of a satellite quantum test of the weak equivalence principle at the 10-17 level,” *Phys. Rev. D* **109**, 064010 (2024), [arXiv:2310.04212 \[physics.space-ph\]](#).
- [139] T. J. Sumner *et al.*, “STEP (satellite test of the equivalence principle),” *Adv. Space Res.* **39**, 254–258 (2007).
- [140] James Overduin, Francis Everitt, Paul Worden, and John Mester, “STEP and fundamental physics,” *Class. Quant. Grav.* **29**, 184012 (2012), [arXiv:1401.4784 \[gr-qc\]](#).
- [141] Jason Williams, Sheng-wei Chiow, Nan Yu, and Holger Mueller, “Quantum Test of the Equivalence Principle and Space-Time aboard the International Space Station,” *New J. Phys.* **18**, 025018 (2016), [arXiv:1510.07780 \[physics.atom-ph\]](#).
- [142] Robert D. Reasenberg and James D. Phillips, “A weak equivalence principle test on a suborbital rocket,” *Class. Quant. Grav.* **27**, 095005 (2010), [arXiv:1001.4752 \[gr-qc\]](#).
- [143] Stephan Schlamminger, K. Y. Choi, T. A. Wagner, J. H. Gundlach, and E. G. Adelberger, “Test of the equivalence principle using a rotating torsion balance,” *Phys. Rev. Lett.* **100**, 041101 (2008), [arXiv:0712.0607 \[gr-qc\]](#).
- [144] Dawid Brzemiński and Aaron Pierce, “A directional force template for quadratically coupled ultralight dark matter,” To appear.
- [145] Hyungjin Kim, Alessandro Lenoci, Gilad Perez, and Wolfram Ratzinger, “Probing an ultralight QCD axion with electromagnetic quadratic interaction,” *Phys. Rev. D* **109**, 015030 (2024), [arXiv:2307.14962 \[hep-ph\]](#).
- [146] Carl Beadle, Sebastian A. R. Ellis, Jérémie Quevillon, and Pham Ngoc Hoa Vuong, “Quadratic coupling of the axion to photons,” *Phys. Rev. D* **110**, 035019 (2024), [arXiv:2307.10362 \[hep-ph\]](#).
- [147] Mikhail A. Shifman, A. I. Vainshtein, and Valentin I. Zakharov, “Remarks on Higgs Boson Interactions with Nucleons,” *Phys. Lett. B* **78**, 443–446 (1978).
- [148] Frank Wilczek, “Origins of Mass,” *Central Eur. J. Phys.* **10**, 1021–1037 (2012), [arXiv:1206.7114 \[hep-ph\]](#).
- [149] C. F. V. Weizsacker, “Zur Theorie der Kernmassen,” *Z. Phys.* **96**, 431–458 (1935).
- [150] H. A. Bethe and R. F. Bacher, “Nuclear Physics A. Stationary States of Nuclei,” *Rev. Mod. Phys.* **8**, 82–229 (1936).
- [151] John Markus Blatt and Victor Frederick Weisskopf, *Theoretical nuclear physics* (Springer, New York, 1952).
- [152] Irving Kaplan and T Teichmann, “Nuclear physics,” (1955).
- [153] Brian D. Serot and John Dirk Walecka, “The Relativistic Nuclear Many Body Problem,” *Adv. Nucl. Phys.* **16**, 1–327 (1986).
- [154] Brian D. Serot and John Dirk Walecka, “Recent progress in quantum hydrodynamics,” *Int. J. Mod. Phys. E* **6**, 515–631 (1997).
- [155] John F. Donoghue, “The Nuclear central force in the chiral limit,” *Phys. Rev. C* **74**, 024002 (2006), [arXiv:nucl-th/0603016](#).
- [156] R. L. Workman *et al.* (Particle Data Group), “Review of Particle Physics,” *PTEP* **2022**, 083C01 (2022).
- [157] P. E. Hodgson, E. Gadioli, and E. Gadioli Erba, *Introductory Nuclear Physics* (Clarendon Press, Oxford, 1997).
- [158] J. Gasser, H. Leutwyler, and M. E. Sainio, “Sigma term update,” *Phys. Lett. B* **253**, 252–259 (1991).
- [159] J. Gasser and H. Leutwyler, “Quark Masses,” *Phys. Rept.* **87**, 77–169 (1982).
- [160] Martin Hoferichter, Jacobo Ruiz de Elvira, Bastian Kubis, and Ulf-G. Meißner, “High-precision determination of the pion-nucleon sigma term from roy-steiner equations,” *Phys. Rev. Lett.* **115**, 092301 (2015), [arXiv:1506.04142 \[hep-ph\]](#).
- [161] Rajan Gupta, Sungwoo Park, Martin Hoferichter, Emanuele Mereghetti, Boram Yoon, and Tanmoy Bhattacharya, “Pion-nucleon sigma term from lattice qcd,” *Phys. Rev. Lett.* **127**, 242002 (2021), [arXiv:2105.12095 \[hep-lat\]](#).
- [162] Y. Aoki *et al.* (Flavour Lattice Averaging Group (FLAG)), “Flag review 2024,” *Phys. Rev. D* **113**, 014508 (2026), [arXiv:2411.04268 \[hep-lat\]](#).
- [163] Sz. Borsanyi, S. Durr, Z. Fodor, C. Hoelbling, S. D. Katz, S. Krieg, L. Lellouch, T. Lippert, A. Portelli, K. K. Szabo, and B. C. Toth, “Ab initio calculation of the neutron-proton mass difference,” *Science* **347**, 1452–1455 (2015), [arXiv:1406.4088 \[hep-lat\]](#).
- [164] Andre Walker-Loud, Carl E. Carlson, and Gerald A. Miller, “The Electromagnetic Self-Energy Contribution to $M_p - M_n$ and the Isovector Nucleon Magnetic Polarizability,” *Phys. Rev. Lett.* **108**, 232301 (2012), [arXiv:1203.0254 \[nucl-th\]](#).
- [165] A. W. Thomas, X. G. Wang, and R. D. Young, “Electromagnetic Contribution to the Proton-Neutron Mass Splitting,” *Phys. Rev. C* **91**, 015209 (2015), [arXiv:1406.4579 \[nucl-th\]](#).
- [166] Alan Robert Edmonds, *Angular momentum in quantum mechanics*, Vol. 4 (Princeton university press, 1996).